ISSN 1949-8470 (online)

World Journal of *Radiology*

World J Radiol 2016 August 28; 8(8): 726-763

Published by Baishideng Publishing Group Inc

WJR World Journal of Radiology

A peer-reviewed, online, open-access journal of Radiology

Editorial Board

2014-2017

The *World Journal of Radiology* Editorial Board consists of 365 members, representing a team of worldwide experts in radiology. They are from 36 countries, including Afghanistan (1), Argentina (2), Australia (5), Austria (7), Belgium (2), Brazil (8), Canada (6), Chile (1), China (43), Croatia (1), Denmark (4), Egypt (6), France (5), Germany (22), Greece (10), India (12), Iran (6), Ireland (2), Israel (3), Italy (47), Japan (13), Netherlands (1), New Zealand (1), Pakistan (1), Poland (2), Portugal (1), Serbia (1), Singapore (3), Slovakia (1), South Korea (18), Spain (4), Sweden (2), Switzerland (4), Thailand (1), Turkey (26), United Kingdom (11), and United States (82).

Yue-Qi Zhu, *Shanghai*

Croatia

Goran Kusec, Osijek

Denmark

Poul E Andersen, *Odense*
Lars J Petersen, *Aalborg*
Thomas Z Ramsoy, *Frederiksberg*
Morten Ziebell, *Copenhagen*

Egypt

Mohamed F Bazeed, *Mansoura*
Mohamed Abou El-Ghar, *Mansoura*
Reem HA Mohamed, *Cairo*
Mohamed R Nouh, *Alexandria*
Ahmed AKA Razek, *Mansoura*
Ashraf A Zytoon, *Shebin El-Koom*

France

Sabine F Bensamoun, *Compiègne*
Romaric Loffroy, *Dijon*
Stephanie Nougaret, *Montpellier*
Hassane Oudadesse, *Rennes*
Vincent Vinh-Hung, *Fort-de-France*

Germany

Henryk Barthel, *Leipzig*
Peter Bannas, *Hamburg*
Martin Beeres, *Frankfurt*
Ilja F Ciernik, *Dessau*
A Dimitrakopoulou-Strauss, *Heidelberg*
Peter A Fasching, *Erlanegn*
Andreas G Schreyer, *Regensburg*
Philipp Heusch, *Duesseldorf*
Sonja M Kirchhoff, *Munich*
Sebastian Ley, *Munich*
Adel Maataoui, *Frankfurt am Main*
Stephan M Meckel, *Freiburg*
Hans W Muller, *Duesseldorf*
Kay Raum, *Berlin*
Dirk Rades, *Luebeck*
Marc-Ulrich Regier, *Hamburg*
Alexey Surov, *Halle*
Martin Walter, *Magdeburg*
Axel Wetter, *Essen*
Christoph Zilkens, *Düsseldorf*

Greece

Panagiotis Antoniou, *Thessaloniki*
Nikos Efthimiou, *Athens*
Dimitris Karnabatidis, *Patras*
George Latsios, *Athens*
Stylianos Megremis, *Iraklion*
Alexander D Rapidis, *Athens*
Kiki Theodorou, *Larissa*
Ioannis A Tsalafoutas, *Athens*
Evanthia E Tripoliti, *Ioannina*
Athina C Tsili, *Ioannina*

India

Ritesh Agarwal, *Chandigarh*
Chandan J Das, *New Delhi*
Prathamesh V Joshi, *Mumbai*
Naveen Kalra, *Chandigarh*
Chandrasekharan Kesavadas, *Trivandrum*
Jyoti Kumar, *New Delhi*
Atin Kumar, *New Delhi*
Kaushala P Mishra, *Allahabad*
Daya N Sharma, *New Delhi*
Binit Sureka, *New Delhi*
Sanjay Sharma, *New Delhi*
Raja R Yadav, *Allahabad*

Iran

Majid Assadi, *Bushehr*
SeyedReza Najafizadeh, *Tehran*
Mohammad Ali Oghabian, *Tehran*
Amir Reza Radmard, *Tehran*
Ramin Sadeghi, *Mashhad*
Hadi Rokni Yazdi, *Tehran*

Ireland

Tadhg Gleeson, *Wexford*
Frederik JAI Vernimmen, *Cork*

Israel

Dafna Ben Bashat, *Tel Aviv*
Amit Gefen, *Tel Aviv*
Tamar Sella, *Jerusalem*

Italy

Adriano Alippi, *Rome*
Dante Amelio, *Trento*
Michele Anzidei, *Rome*
Filippo F Angileri, *Messinas*
Stefano Arcangeli, *Rome*
Roberto Azzoni, *San Donato milanese*
Tommaso V Bartolotta, *Palermo*
Tommaso Bartalena, *Imola*
Livia Bernardin, *San Bonifacio*
Federico Boschi, *Verona*
Sergio Casciaro, *Lecce*
Emanuele Casciani, *Rome*
Musa M Can, *Napoli*
Alberto Cuocolo, *Napoli*
Michele Ferrara, *Coppito*
Mauro Feola, *Fossano*
Giampiero Francica, *Castel Volturno*
Luigi De Gennaro, *Rome*
Giulio Giovannetti, *Pisa*
Francesca Iacobellis, *Napoli*
Formato Invernizzi, *Monza Brianza*
Francesco Lassandro, *Naples*
Lorenzo Livi, *Florence*
Pier P Mainenti, *Napoli*
Laura Marzetti, *Chieti*
Giuseppe Malinverni, *Crescentino*
Enrica Milanesi, *Turin*
Giovanni Morana, *Treviso*
Lorenzo Monti, *Milan*
Silvia D Morbelli, *Genoa*
Barbara Palumbo, *Perugia*
Cecilia Parazzini, *Milan*
Stefano Pergolizzi, *Messina*
Antonio Pinto, *Naples*
Camillo Porcaro, *Rome*
Carlo C Quattrocchi, *Rome*
Alberto Rebonato, *Perugia*
Giuseppe Rizzo, *Rome*
Roberto De Rosa, *Naples*
Domenico Rubello, *Rovigo*
Andrea Salvati, *Bari*
Sergio Sartori, *Ferrara*
Luca M Sconfienza, *Milano*
Giovanni Storto, *Rionero*
Nicola Sverzellati, *Parma*
Alberto S Tagliafico, *Genova*
Nicola Troisi, *Florence*

Japan

Yasuhiko Hori, *Chiba*
Hidetoshi Ikeda, *Koriyama*
Masahito Kawabori, *Sapporo*
Tamotsu Kamishima, *Sapporo*
Hiro Kiyosue, *Yufu*
Yasunori Minami, *Osaka-sayama*
Yasuhiro Morimoto, *Kitakyushu*
Satoru Murata, *Tokyo*
Shigeki Nagamachi, *Miyazaki*
Hiroshi Onishi, *Yamanashi*
Morio Sato, *Wakayama Shi*
Yoshito Tsushima, *Maebashi*
Masahiro Yanagawa, *Suita*

Netherlands

Willem Jan van Rooij, *Tilburg*

New Zealand

W Howell Round, *Hamilton*

Pakistan

Wazir Muhammad, *Abbottabad*

Poland

Maciej S Baglaj, *Wroclaw*

Piotr Czauderna, *Gdansk*

Portugal

Joao Manuel RS Tavares, *Porto*

Serbia

Olivera Ciraj-Bjelac, *Belgrade*

Singapore

Gopinathan Anil, *Singapore*
Terence KB Teo, *Singapore*
Cher Heng Tan, *Singapore*

Slovakia

Stefan Sivak, *Martin*

South Korea

Ki Seok Choo, *Busan*
Seung Hong Choi, *Seoul*
Dae-Seob Choi, *Jinju*
Hong-Seok Jang, *Seoul*
Yong Jeong, *Daejeon*
Chan Kyo Kim, *Seoul*
Se Hyung Kim, *Seoul*
Joong-Seok Kim, *Seoul*
Sang Eun Kim, *Seongnam*
Sung Joon Kwon, *Seoul*
Jeong Min Lee, *Seoul*
In Sook Lee, *Busan*
Noh Park, *Goyang*
Chang Min Park, *Seoul*
Sung Bin Park, *Seoul*
Deuk Jae Sung, *Seoul*
Choongsoo Shin, *Seoul*
Kwon-Ha Yoon, *Iksan*

Spain

Miguel A De Gregorio, *Zaragoza*
Antonio Luna, *Jaén*
Enrique Marco de Lucas, *Santander*
Fernando Ruiz Santiago, *Granada*

Sweden

Dmitry Grishenkov, *Stockholm*
Tie-Qiang Li, *Stockholm*

Switzerland

Nicolau Beckmann, *Basel*
Christian Boy, *Bern*
Giorgio Treglia, *Bellinzona*

Stephan Ulmer, *Kiel*

Thailand

Sirianong Namwongprom, *Chiang Mai*

Turkey

Kubilay Aydin, *Istanbul*
Ramazan Akdemir, *Sakarya*
Serhat Avcu, *Ankara*
Ayse Aralasmak, *Istanbul*
Oktay Algin, *Ankara*
Nevbahar Akcar, *Meselik*
Bilal Battal, *Ankara*
Zulkif Bozgeyik, *Elazig*
Nazan Ciledag, Aakara
Fuldem Y Donmez, *Ankara*
Gulgun Engin, *Istanbul*
Ahmet Y Goktay, *Izmir*
Oguzhan G Gumustas, *Bursa*
Kaan Gunduz, *Ankara*
Pelin Ozcan Kara, *Mersin*
Kivanc Kamburoglu, *Ankara*
Ozgur Kilickesmez, *Istanbul*
Furuzan Numan, *Istanbul*
Cem Onal, *Adana*
Ozgur Oztekin, *Izmir*
Seda Ozbek (Boruban), *Konya*
Selda Sarikaya, *Zonguldak*
Figen Taser, *Kutahya*
Baran Tokar, *Eskisehir*
Ender Uysal, *Istanbul*
Ensar Yekeler, *Istanbul*

United Kingdom

Indran Davagnanam, *London*
M DC Valdés Hernández, *Edinburgh*
Alan Jackson, *Manchester*
Suneil Jain, *Belfast*
Long R Jiao, *London*
Miltiadis Krokidis, *Cambridge*
Pradesh Kumar, *Liverpool*
Peter D Kuzmich, *Derby*
Georgios Plataniotis, *Brighton*
Vanessa Sluming, *Liverpool*

United States

Garima Agrawal, *Saint Louis*
James R Brasic, *Baltimore*
Rajendra D Badgaiyan, *Buffalo*
Ulas Bagci, *Bethesda*
Anat Biegon, *Stony Brook*
Ramon Casanova, *Winston Salem*
Wenli Cai, *Boston*
Zheng Chang, *Durham*
Corey J Chakarun, *Long Beach*
Kai Chen, *Los Angeles*
Hyun-Soon Chong, *Chicago*
Marco Cura, *Dallas*
Ravi R Desai, *Bensalem*
Delia DeBuc, *Miami*
Carlo N De Cecco, *Charleston*
Timm-Michael L Dickfeld, *Baltimore*
Subba R Digumarthy, *Boston*
Huy M Do, *Stanford*
Todd A Faasse, *Grand Rapids*
Salomao Faintuch, *Boston*
Girish M Fatterpekar, *New York*
Dhakshinamoorthy Ganeshan, *Houston*
Robert J Griffin, *Little Rock*
Andrew J Gunn, *Boston*
Sandeep S Hedgire, *Boston*
Timothy J Hoffman, *Columbia*
Mai-Lan Ho, *San Francisco*
Juebin Huang, *Jackson*
Abid Irshad, *Charleston*
Matilde Inglese, *New York*
El-Sayed H Ibrahim, *Jacksonville*
Paul R Julsrud, *Rochester*
Pamela T Johnson, *Baltimore*
Ming-Hung Kao, *Tempe*
Sunil Krishnan, *Houston*
Richard A Komoroski, *Cincinnati*
Sandi A Kwee, *Honolulu*
King Kim, *Ft. Lauderdale*
Guozheng Liu, *Worcester*
Yiyan Liu, *Newark*
Venkatesh Mani, *New York*
Lian-Sheng Ma, *Pleasanton*
Rachna Madan, *Boston*
Zeyad A Metwalli, *Houston*
Yilong Ma, *Manhasset*
Hui Mao, *Atlanta*
Feroze B Mohamed, *Philadelphia*
Gul Moonis, *Boston*
John L Nosher, *New Brunswick*
Rahmi Oklu, *Boston*
Aytekin Oto, *Chicago*
Bishnuhari Paudyal, *Philadelphia*
Rajul Pandya, *Youngstown*
Chong-Xian Pan, *Sacramento*
Jay J Pillai, *Baltimore*
Neal Prakash, *Duarte*
Reza Rahbar, *Boston*
Ali S Raja, *Boston*
Gustavo J Rodriguez, *El Paso*
David J Sahn, *Portlsand*
Steven Schild, *Scottsdale*
Ali R Sepahdari, *Los Angeles*
Li Shen, *Indianapolis*
JP Sheehan, *Charlottesville*
Atul B Shinagare, *Boston*
Sarabjeet Singh, *Boston*
Charles J Smith, *Columbia*
Kenji Suzuki, *Chicago*
Monvadi Srichai-Parsia, *Washington*
Sree H Tirumani, *Boston*
Hebert A Vargas, *New York*
Sachit Verma, *Philadelphia*
Yoichi Watanabe, *Minneapolis*
Li Wang, *Chapel Hill*
Carol C Wu, *Boston*
Shoujun Xu, *Houston*
Min Yao, *Cleveland*
Xiaofeng Yang, *Atlanta*
Qingbao Yu, *Albuquerque*
Aifeng Zhang, *Chicago*
Chao Zhou, *Bethlehem*
Hongming Zhuang, *Philadelphia*

WJR World Journal of Radiology

Contents

Monthly Volume 8 Number 8 August 28, 2016

World Journal of Radiology
Volume 8 Number 8 August 28, 2016

Contents

NAME OF JOURNAL
World Journal of Radiology

ISSN
ISSN 1949-8470 (online)

LAUNCH DATE
January 31, 2009

FREQUENCY
Monthly

EDITORIAL OFFICE
Jin-Lei Wang, Director
Xiu-Xia Song, Vice Director
World Journal of Radiology
Room 903, Building D, Ocean International Center,
No. 62 Dongsihuan Zhonglu, Chaoyang District,
Beijing 100025, China
Telephone: +86-10-59080039
Fax: +86-10-85381893
E-mail: editorialoffice@wjgnet.com
Help Desk: http://www.wjgnet.com/esps/helpdesk.aspx
http://www.wjgnet.com

PUBLISHER
Baishideng Publishing Group Inc
8226 Regency Drive,
Pleasanton, CA 94588, USA
Telephone: +1-925-223-8242
Fax: +1-925-223-8243
E-mail: bpgoffice@wjgnet.com
Help Desk: http://www.wjgnet.com/esps/helpdesk.aspx
http://www.wjgnet.com

PUBLICATION DATE
August 28, 2016

INSTRUCTIONS TO AUTHORS
http://www.wjgnet.com/bpg/gerinfo/204

ONLINE SUBMISSION
http://www.wjgnet.com/esps/

World Journal of Radiology

Submit a Manuscript: http://www.wjgnet.com/esps/
Help Desk: http://www.wjgnet.com/esps/helpdesk.aspx
DOI: 10.4329/wjr.v8.i8.726

World J Radiol 2016 August 28; 8(8): 726-728
ISSN 1949-8470 (online)

EDITORIAL

Peripheral nerve imaging: Not only cross-sectional area

Alberto Stefano Tagliafico

Alberto Stefano Tagliafico, Department of Experimental Medicine, DIMES, Institute of Anatomy, University of Genova, 16132 Genova, Italy

Author contributions: Tagliafico AS solely contributed to the paper.

Conflict-of-interest statement: The author declares no conflicts of interest regarding this manuscript.

Manuscript source: Invited manuscript

Correspondence to: Alberto Stefano Tagliafico, MD, Radiologist, Assistant Professor of Human Anatomy, Department of Experimental Medicine, DIMES, Institute of Anatomy, University of Genova, Via de Toni 14, 16132 Genova, Italy. alberto.tagliafico@unige.it
Telephone: +39-010-3537882
Fax: +39-010-3537885

Received: March 17, 2016
Peer-review started: March 19, 2016
First decision: April 15, 2016
Revised: April 19, 2016
Accepted: June 14, 2016
Article in press: June 16, 2016
Published online: August 28, 2016

Abstract

Peripheral nerve imaging is recognized as a complement to clinical and neurophysiological assessment in the evaluation of peripheral nerves with the ability to impact patient management, even for small and difficult nerves. The European Society of Musculoskeletal Radiology, suggest to use ultrasound (US) for nerve evaluation due to the fact that, in sever anatomical area, magnetic resonance imaging is not able to give additional informations. US could be considered the first-choice approach for the assessment of peripheral nerves. The relative drawback of peripheral nerve US is the long learning curve and the deep anatomic competence to evaluate even small nerves. In the recent years, the role of US in peripheral nerve evaluation has been widened. In the past, nerve US was mainly used to assess nerve-cross sectional area, but now more advanced measurements and considerations are desirable and can boost the role of peripheral nerve US. Nerve echotexture evaluation was defined in 2010: The ratio between the hypoechoic and hyperechoic areas of peripheral nerves on US was called "nerve density". For evaluation of patients who have peripheral neuropathies, the role of peripheral nerve is US wider than simple cross-sectional area evaluation. Quantitative measurements describing the internal fascicular echotexture of peripheral nerves introduce the concept of considering US as a possible quantitative imaging biomarker technique. The potential of nerve US has started to be uncovered. It seems clear that only cross-sectional area measurement is no more sufficient for a comprehensive US evaluation of peripheral nerves.

Key words: Ultrasound; Imaging; Magnetic resonance imaging; Nerve density; Fascicular ratio

Core tip: Ultrasound (US) is a possible quantitative imaging biomarker technique for peripheral nerves evaluation. The potential of nerve US has therefore started to be uncovered and it seems clear that only cross-sectional area measurement is no more sufficient for a comprehensive US evaluation of peripheral nerves.

Tagliafico AS. Peripheral nerve imaging: Not only cross-sectional area. *World J Radiol* 2016; 8(8): 726-728 Available from: URL:

http://www.wjgnet.com/1949-8470/full/v8/i8/726.htm DOI: http://dx.doi.org/10.4329/wjr.v8.i8.726

INTRODUCTION

Peripheral nerve imaging is recognized as a complement to clinical and neurophysiological assessment in the evaluation of peripheral nerves with the ability to impact patient management, even for small and difficult nerves[1-7]. In daily radiological clinical practice, ultrasound (US) and magnetic resonance imaging (MRI) are the technics of choice. The European Society of Musculoskeletal Radiology, suggest to use US for nerve evaluation due to the fact that, in sever anatomical area, MRI is not able to give additional informations[8]. For deep nerve or central disease, conventional MRI, MRI neurography, diffusion tensor imaging, fiber tractography[9] and 3D MRI[10] are promising but are not always available and need long acquisition time. Therefore, US could be considered the first-choice approach for the assessment of peripheral nerves. US is a relative low-cost technique, widely available and with dynamic capabilities[1-13]. In addition, evaluation of the entire limb during a unique exam is possibly with great spare of time compared to MRI. The relative drawback of peripheral nerve US is the long learning curve and the deep anatomic competence to evaluate even small nerves[1-14]. To improve the knowledge of peripheral nerve US, the International Society of Peripheral Neurophysiological Imaging (http://www.ispni.org/), founded in 2014, supports the pivotal role of peripheral nerve US in the assessment of patients with suspect peripheral nerve pathological involvement. Not surprisingly, in the recent years, the role of US in peripheral nerve evaluation has been widened[15,16]. In the past, nerve US was mainly used to assess nerve-cross sectional area[17-22], but now more advanced measurements and considerations are desirable and can boost the role of peripheral nerve US.

Nerve echotexture evaluation was defined in 2010. Our research group, using US, developed a software that quantifies the ratio between the hypoechoic and hyperechoic areas of peripheral nerves on US[23]. We called this parameter: "nerve density"[23]. We evaluated sixty-five different patients and (n = 65) controls (age range, 35-81 years; mean 55 years) prospectively. Nerve density was capable of discriminating between normal and pathologic nerves of patients affected by carpal tunnel syndrome or neurofibromas. Moreover, nerve density measure was useful to discriminate between patients with mild and severe Carpal Tunnel Syndrome[23].

In addition, we defined and quantitatively evaluated the fascicular ratio (FR) on MRI in patients with peripheral neuropathies compared with healthy controls[24,25]. On MRI, FRs were significantly increased in patients compared with controls (FR, 76.7 ± 15.1 *vs* 56 ± 12.3; $P < 0.0001$ for the semiautomatic interface; and FR 66.3 ± 17.5 *vs* 47.8 ± 18.4; $P < 0.0001$ for the automatic interface). The increase in FR was caused mainly by an increase in the hypointense part of the nerve and this observation was valid for all causes of neuropathies[24,25].

CONCLUSION

For evaluation of patients who have peripheral neuropathies, the role of peripheral nerve is US wider than simple cross-sectional area evaluation[25]. Quantitative measurements describing the internal fascicular echotexture of peripheral nerves introduce the concept of considering US as a possible quantitative imaging biomarker technique[22]. Indeed, quantitative assessment of nerve echogenicity or the FR has been considered a step further in the evaluation of peripheral nerves by the means of US[23-27]. The potential of nerve US has started to be uncovered. It seems clear that only cross-sectional area measurement is no more sufficient for a comprehensive US evaluation of peripheral nerves.

REFERENCES

1 **Bignotti B**, Tagliafico A, Martinoli C. Ultrasonography of Peripheral Nerves: Anatomy and Pathology. *Ultrasound Clinics* 2014; **9**: 525-536 [DOI: 10.1016/j.cult.2014.03.006]

2 **Tagliafico A**, Bignotti B, Miguel Perez M, Reni L, Bodner G, Martinoli C. Contribution of ultrasound in the assessment of patients with suspect idiopathic pudendal nerve disease. *Clin Neurophysiol* 2014; **125**: 1278-1284 [PMID: 24368033 DOI: 10.1016/j.clinph.2013.10.053]

3 **Hobson-Webb LD**, Padua L, Martinoli C. Ultrasonography in the diagnosis of peripheral nerve disease. *Expert Opin Med Diagn* 2012; **6**: 457-471 [PMID: 23480810 DOI: 10.1517/17530059.2012.692904]

4 **Tagliafico A**, Padua L, Martinoli C. High-resolution ultrasonography in the assessment of meralgia paresthetica: some clarifications are needed. *Muscle Nerve* 2012; **45**: 922; author reply 922 [PMID: 22581555 DOI: 10.1002/mus.23391]

5 **Tagliafico A**, Bodner G, Rosenberg I, Palmieri F, Garello I, Altafini L, Martinoli C. Peripheral nerves: ultrasound-guided interventional procedures. *Semin Musculoskelet Radiol* 2010; **14**: 559-566 [PMID: 21072732 DOI: 10.1055/s-0030-1268066]

6 **Martinoli C**, Gandolfo N, Perez MM, Klauser A, Palmieri F, Padua L, Tagliafico A. Brachial plexus and nerves about the shoulder. *Semin Musculoskelet Radiol* 2010; **14**: 523-546 [PMID: 21072730 DOI: 10.1055/s-0030-1268072]

7 **Tagliafico A**, Altafini L, Garello I, Marchetti A, Gennaro S, Martinoli C. Traumatic neuropathies: spectrum of imaging findings and postoperative assessment. *Semin Musculoskelet Radiol* 2010; **14**: 512-522 [PMID: 21072729 DOI: 10.1055/s-0030-1268071]

8 **Klauser AS**, Tagliafico A, Allen GM, Boutry N, Campbell R, Court-Payen M, Grainger A, Guerini H, McNally E, O'Connor PJ, Ostlere S, Petroons P, Reijnierse M, Sconfienza LM, Silvestri E, Wilson DJ, Martinoli C. Clinical indications for musculoskeletal ultrasound: a Delphi-based consensus paper of the European Society of Musculoskeletal Radiology. *Eur Radiol* 2012; **22**: 1140-1148 [PMID: 22453857 DOI: 10.1007/s00330-011-2356-3]

9 **Tagliafico A**, Calabrese M, Puntoni M, Pace D, Baio G, Neumaier CE, Martinoli C. Brachial plexus MR imaging: accuracy and reproducibility of DTI-derived measurements and fibre tractography at 3.0-T. *Eur Radiol* 2011; **21**: 1764-1771 [PMID: 21424901 DOI: 10.1007/s00330-011-2100-z]

10 **Tagliafico A**, Succio G, Neumaier CE, Baio G, Serafini G, Ghidara M, Calabrese M, Martinoli C. Brachial plexus assessment

with three-dimensional isotropic resolution fast spin echo MRI: comparison with conventional MRI at 3.0 T. *Br J Radiol* 2012; **85**: e110-e116 [PMID: 21343321 DOI: 10.1259/bjr/28972953]
11 **Tagliafico AS**, Bignotti B, Martinoli C. Elbow US: Anatomy, Variants, and Scanning Technique. *Radiology* 2015; **275**: 636-650 [PMID: 25997130 DOI: 10.1148/radiol.2015141950]
12 **Martinoli C**, Garello I, Marchetti A, Palmieri F, Altafini L, Valle M, Tagliafico A. Hip ultrasound. *Eur J Radiol* 2012; **81**: 3824-3831 [PMID: 21571471 DOI: 10.1016/j.ejrad.2011.03.102]
13 **Martinoli C**, Miguel-Perez M, Padua L, Gandolfo N, Zicca A, Tagliafico A. Imaging of neuropathies about the hip. *Eur J Radiol* 2013; **82**: 17-26 [PMID: 21549536 DOI: 10.1016/j.ejrad.2011.04.034]
14 **Tagliafico A**, Bignotti B, Cadoni A, Perez MM, Martinoli C. Anatomical study of the iliohypogastric, ilioinguinal, and genitofemoral nerves using high-resolution ultrasound. *Muscle Nerve* 2015; **51**: 42-48 [PMID: 24797303 DOI: 10.1002/mus.24277]
15 **Tagliafico A**, Perez MM, Martinoli C. High-Resolution ultrasound of the pudendal nerve: normal anatomy. *Muscle Nerve* 2013; **47**: 403-408 [PMID: 23180573 DOI: 10.1002/mus.23537]
16 **Tagliafico A**, Serafini G, Lacelli F, Perrone N, Valsania V, Martinoli C. Ultrasound-guided treatment of meralgia paresthetica (lateral femoral cutaneous neuropathy): technical description and results of treatment in 20 consecutive patients. *J Ultrasound Med* 2011; **30**: 1341-1346 [PMID: 21968484]
17 **Tagliafico A**, Resmini E, Nizzo R, Derchi LE, Minuto F, Giusti M, Martinoli C, Ferone D. The pathology of the ulnar nerve in acromegaly. *Eur J Endocrinol* 2008; **159**: 369-373 [PMID: 18632873 DOI: 10.1530/EJE-08-0327]
18 **Resmini AE**, Tagliafico, Nizzo R, Bianchi F, Minuto F, Derchi L, Martinoli C, Ferone D. P-21 Relationship between IGF-I levels and peripheral nerve enlargement in acromegaly. *Growth Horm IGF Res* 2008; **2**: 18 [DOI: 10.1016/S1096-6374(08)70106-0]
19 **Tagliafico A**, Pugliese F, Bianchi S, Bodner G, Padua L, Rubino M, Martinoli C. High-resolution sonography of the palmar cutaneous branch of the median nerve. *AJR Am J Roentgenol* 2008; **191**: 107-114 [PMID: 18562732 DOI: 10.2214/AJR.07.3383]
20 **Tagliafico A**, Resmini E, Nizzo R, Bianchi F, Minuto F, Ferone D, Martinoli C. Ultrasound measurement of median and ulnar nerve cross-sectional area in acromegaly. *J Clin Endocrinol Metab* 2008; **93**: 905-909 [PMID: 18073306 DOI: 10.1210/jc.2007-1719]
21 **Tagliafico A**, Martinoli C. Reliability of side-to-side sonographic cross-sectional area measurements of upper extremity nerves in healthy volunteers. *J Ultrasound Med* 2013; **32**: 457-462 [PMID: 23443186]
22 **Tagliafico A**, Cadoni A, Fisci E, Bignotti B, Padua L, Martinoli C. Reliability of side-to-side ultrasound cross-sectional area measurements of lower extremity nerves in healthy subjects. *Muscle Nerve* 2012; **46**: 717-722 [PMID: 23055313 DOI: 10.1002/mus.23417]
23 **Tagliafico A**, Tagliafico G, Martinoli C. Nerve density: a new parameter to evaluate peripheral nerve pathology on ultrasound. Preliminary study. *Ultrasound Med Biol* 2010; **36**: 1588-1593 [PMID: 20850025 DOI: 10.1016/j.ultrasmedbio.2010.07.009]
24 **Tagliafico AS**, Tagliafico G. Fascicular ratio: a new parameter to evaluate peripheral nerve pathology on magnetic resonance imaging: a feasibility study on a 3T MRI system. *Medicine* (Baltimore) 2014; **93**: e68 [PMID: 25255018 DOI: 10.1097/MD.0000000000000068]
25 **Tagliafico A**, Bignotti B. New Parameters for Evaluating Peripheral Nerve Disorders on Sonography and Magnetic Resonance Imaging. *J Ultrasound Med* 2015; **34**: 1523 [PMID: 26206844 DOI: 10.7863/ultra.34.8.1523]
26 **Wilder-Smith EP**. Quantitative assessment of peripheral nerve ultrasound echogenicity. A step forward. *Clin Neurophysiol* 2012; **123**: 1267-1268 [PMID: 22182966 DOI: 10.1016/j.clinph.2011.11.038]
27 **Boom J**, Visser LH. Quantitative assessment of nerve echogenicity: comparison of methods for evaluating nerve echogenicity in ulnar neuropathy at the elbow. *Clin Neurophysiol* 2012; **123**: 1446-1453 [PMID: 22217961 DOI: 10.1016/j.clinph.2011.10.050]

P- Reviewer: Chow J, Gao BL, Nouh MR **S- Editor**: Qiu S
L- Editor: A **E- Editor**: Zhang FF

World Journal of Radiology

Submit a Manuscript: http://www.wjgnet.com/esps/
Help Desk: http://www.wjgnet.com/esps/helpdesk.aspx
DOI: 10.4329/wjr.v8.i8.729

World J Radiol 2016 August 28; 8(8): 729-734
ISSN 1949-8470 (online)

Enhanced characterization of solid solitary pulmonary nodules with Bayesian analysis-based computer-aided diagnosis

Simone Perandini, Gian Alberto Soardi, Massimiliano Motton, Raffaele Augelli, Chiara Dallaserra, Gino Puntel, Arianna Rossi, Giuseppe Sala, Manuel Signorini, Laura Spezia, Federico Zamboni, Stefania Montemezzi

Simone Perandini, Gian Alberto Soardi, Massimiliano Motton, Raffaele Augelli, Chiara Dallaserra, Gino Puntel, Arianna Rossi, Giuseppe Sala, Manuel Signorini, Laura Spezia, Federico Zamboni, Stefania Montemezzi, Department of Radiology, Azienda Ospedaliera Universitaria Integrata di Verona, 37100 Verona, Italy

Author contributions: Perandini S, Soardi GA, Motton M and Montemezzi S designed and wrote the manuscript; Augelli R, Dallaserra C, Puntel G, Rossi A, Sala G, Signorini M, Spezia L and Zamboni F equally collected and analyzed the data in addition to performing literature search and manuscript revision.

Conflict-of-interest statement: The authors declare no conflicts of interest regarding this manuscript.

Manuscript source: Invited manuscript

Correspondence to: Simone Perandini, MD, Department of Radiology, Azienda Ospedaliera Universitaria Integrata di Verona, Piazzale Stefani 1, 37100 Verona, Italy. simone.perandini@ospedaleuniverona.it
Telephone: +39-045-8122124
Fax: +39-045-8122124

Received: February 18, 2016
Peer-review started: February 21, 2016
First decision: March 25, 2016
Revised: April 12, 2016
Accepted: July 11, 2016
Article in press: July 13, 2016
Published online: August 28, 2016

Abstract

The aim of this study was to prospectively assess the accuracy gain of Bayesian analysis-based computer-aided diagnosis (CAD) *vs* human judgment alone in characterizing solitary pulmonary nodules (SPNs) at computed tomography (CT). The study included 100 randomly selected SPNs with a definitive diagnosis. Nodule features at first and follow-up CT scans as well as clinical data were evaluated individually on a 1 to 5 points risk chart by 7 radiologists, firstly blinded then aware of Bayesian Inference Malignancy Calculator (BIMC) model predictions. Raters' predictions were evaluated by means of receiver operating characteristic (ROC) curve analysis and decision analysis. Overall ROC area under the curve was 0.758 before and 0.803 after the disclosure of CAD predictions (P = 0.003). A net gain in diagnostic accuracy was found in 6 out of 7 readers. Mean risk class of benign nodules dropped from 2.48 to 2.29, while mean risk class of malignancies rose from 3.66 to 3.92. Awareness of CAD predictions also determined a significant drop on mean indeterminate SPNs (15 *vs* 23.86 SPNs) and raised the mean number of correct and confident diagnoses (mean 39.57 *vs* 25.71 SPNs). This study provides evidence supporting the integration of the Bayesian analysis-based BIMC model in SPN characterization.

Key words: Solitary pulmonary nodule; Computer-aided diagnosis; Lung neoplasms; Multidetector computed tomography; Bayesian prediction

Core tip: The aim of this study was to prospectively assess the net accuracy gain of using computer-aided diagnosis in characterizing solitary pulmonary nodules detected at computed tomography. One-hundred

randomly selected nodules with a definitive diagnosis were reviewed by 7 radiologists, before and after computer predictions. A net gain in diagnostic accuracy was found in 6 out of 7 readers. This study provides further evidence supporting the integration of computer aided diagnosis in nodule characterization.

Perandini S, Soardi GA, Motton M, Augelli R, Dallaserra C, Puntel G, Rossi A, Sala G, Signorini M, Spezia L, Zamboni F, Montemezzi S. Enhanced characterization of solid solitary pulmonary nodules with Bayesian analysis-based computer-aided diagnosis. *World J Radiol* 2016; 8(8): 729-734 Available from: URL: http://www.wjgnet.com/1949-8470/full/v8/i8/729.htm DOI: http://dx.doi.org/10.4329/wjr.v8.i8.729

INTRODUCTION

Solitary pulmonary nodules (SPNs) are a common radiological finding at computed tomography (CT)[1]. While the presence of multiple nodules can be suggestive of secondary pulmonary involvement, a single SPN can be more problematic to characterize. Benign and malignant SPNs are often difficult to discriminate on the basis of their appearance, due to the overlap of radiographic features such as shape, edge, size, and location within the lungs[2]. The presence of accessory findings such as calcifications within the nodule, hilar or mediastinal adenopathy and pleural effusion, can help the radiologist in better assessing the nature of the lesions[3]; however, this is rarely the case. The Fleischner Society has issued recommendations about the work-up of a newly discovered SPN, suggesting to obtain a pre-test probability of malignancy[4]. A few malignancy prediction algorithms have been introduced in the literature[5-7] to aid radiologists in integrating clinical and imaging information into a reproducible and quantitative evaluation of the malignancy risk of a lesion. Among these, the recently introduced Bayesian Inference Malignancy Calculator (BIMC, http://www.simoneperandini.com/bimc/) model has shown promising results in SPN classification[8]. However, there is little or no evidence in the literature that these prediction models can enhance discrimination of SPNs at the time of diagnosis. Bayesian analysis is a form of statistical inference in which the probability favoring a hypothesis increases or lowers as more information becomes available. It fits particularly well in actual clinical scenarios, where data are often partly available. The primary purpose of this study was to evaluate the net accuracy gain of an integrated human and computer-aided diagnosis (CAD) approach *vs* human judgment alone in distinguishing benign from malignant SPNs detected at CT. The secondary aim was to assess how the adoption of the model modifies judgment among raters, and, in particular, whether it allows for more accurate diagnosis of nodules perceived as having intermediate risk by human judgment alone.

RESEARCH AND LITERATURE

A total of 100 solid SPNs from 100 patients, consisting of 35 benign and 65 malignant nodules, were randomly collected from the local database of SPNs referred to our center for characterization. The inclusion criteria were the presence of one solid (defined as a nodule with at least a solid component > 80% of the total volume) SPN, an available thin section CT scan encompassing the lungs and a definitive diagnosis by means of tissue biopsy or imaging follow-up, as suggested by guidelines[4]. The exclusion criteria were the presence of visible nodule calcifications and the presence of more than one nodule in the same patient. Patients were imaged with a 256-row multi-detector computed tomography (MDCT) system (Brilliance iCT: Philips Healthcare) or a 64-row MDCT system (LightSpeed: General Electrics Healthcare). CT scans were performed using sub-millimetric (0.9 mm), millimetric (1 mm) or near-millimetric (1.25 mm) contiguous slices. Data were reconstructed with a matrix of 512 × 512. The diameters of all nodules were measured by means of a linear digital caliper tool. The nodules were independently reviewed by 7 radiologists with expertise in thoracic imaging ranging from 3 to 10 years, blinded to final diagnosis and prevalence of malignancy, on Multi-Planar Reconstruction images on a professional workstation (Carestream Picture Archiving and Communication System, Carestream Health, 2011). All nodules were independently reviewed by the raters in the same order. Clinical and anamnestic data were collected from the hospital electronic records and made preliminarily available to raters. The reviewer was firstly asked to assess image quality as optimal or sub-optimal for diagnosis. They were subsequently asked to classify the probability of malignancy of the lesion before and after disclosure of the BIMC model result according to the classes detailed in Table 1, and to record and enter personal results in a spreadsheet. The BIMC model is a recent SPN risk prediction model developed in 2015; it works by providing the user with a risk probability after the collection of all available data. It currently supports the following features: Age, smoking (Pack-years), history of previous malignancy, size (mm), location within the lungs, edges, volume doubling time, minimum focal density, contrast enhancement and F-18 fluorodeoxyglucose positron emission tomography SUVmax value. Since it was developed as a Bayesian classifier, it tolerates partial data collection. The model was designed to be a useful tool for integrating all available data in an objective, reproducible manner. In this study the BIMC model was accessed either in the version of a computer application (http://www.simoneperandini.com/npsbimc/download.htm) or in its web counterpart (http://www.simoneperandini.com/bimc/).

A different operator, which was not included among the raters, merged the data and performed the analysis. Reviewers' performance was assessed by means of receiver operating characteristic (ROC) curve analysis.

Table 1 Classification of solitary pulmonary nodule malignancy adopted in the current study

Class	Probability of malignancy
1	Minimal risk; almost certainly benign
2	Low risk; probably benign
3	Intermediate risk; not further characterizable
4	High risk; probably malignant
5	Very high risk; almost certainly malignant

Table 2 Area under the receiver operating characteristic curve values before and following disclosure of the computer-aided diagnosis data for the different raters

Rater	SPNs	AUC blinded 95%CI	AUC unfolded 95%CI	Difference	Significance
BIMC	94	0.845 0.755-0.911	-	-	-
Rater 1	94	0.734 0.633-0.820	0.769 0.671-0.850	0.035	$P = 0.3329$
Rater 2	94	0.788 0.691-0.865	0.820 0.727-0.892	0.032	$P = 0.2170$
Rater 3	94	0.788 0.692-0.866	0.830 0.738-0.899	0.042	$P = 0.0592$
Rater 4	94	0.739 0.639-0.825	0.795 0.699-0.871	0.056	$P = 0.0048$
Rater 5	94	0.751 0.651-0.834	0.815 0.721-0.887	0.064	$P = 0.0300$
Rater 6	94	0.836 0.745-0.904	0.833 0.742-0.902	-0.003	$P = 0.9308$
Rater 7	94	0.682 0.578-0.774	0.756 0.657-0.839	0.074	$P = 0.0054$
Overall	658	0.758 0.723-0.790	0.803 0.770-0.833	0.045	$P = 0.0003$

AUC: Area under the curve; SPNs: Solitary pulmonary nodules; BIMC: Bayesian inference malignancy calculator.

Table 3 Mean number of predicted solitary pulmonary nodules for each risk class considered, before (pre-computer-aided diagnosis) and after (post-computer-aided diagnosis) computer-aided diagnosis result disclosure

Risk class	Benign SPNs		Malignant SPNs	
	Pre-CAD	Post-CAD	Pre-CAD	Post-CAD
1	6.71	13.43	1.86	1.86
2	12.43	6.86	8.43	7.14
3	6.43	3.71	17.43	11.29
4	3.57	5.00	15.29	15.57
5	2.86	3.00	19.00	26.14

SPNs: Solitary pulmonary nodules; CAD: Computer-aided diagnosis.

Analysis of ROC curves was performed according to DeLong *et al*[9]. Risk class ratings before and after disclosure of CAD data were collected in a spreadsheet and analyzed. Statistical analyses were conducted with MedCalc Statistical Software (MedCalc Software bvba, Ostend, Belgium; http://www.medcalc.org; 2014).

CONCLUSION

Six nodules were discarded from the original 100 because at least one of the reviewers found image quality to be sub-optimal for diagnosis. The study population consisted of 94 nodules from 94 different patients (57 males and 37 females). Mean age ± standard deviation (SD) was 65 ± 9 years. Mean nodule diameter ± SD was 14.84 ± 7.23 mm. The resulting population consisted of 62 malignant nodules and 32 benign nodules. Definitive diagnoses were obtained by tissue biopsy in 78 nodules and by lack of significant growth according to guidelines or volumetric reduction in 16 nodules. Benign nodules were composed of 8 hamartomas, 2 fibrotic nodules, 3 non-tubercular granulomas, 1 tubercular granuloma, 1 lymph node with signs of histiocytosis, 1 nodule of organizing pneumonia, and 16 nodules which proved stable according to American College of Chest Physicians guidelines. Malignancies were composed of 4 large cell carcinomas, 29 adenocarcinomas (4 minimally invasive, 11 not otherwise specified, 14 invasive), 5 squamocellular carcinomas, 12 typical carcinoids, and 12 metastases. ROC curve analysis is summarized in Table 2 and illustrated in Figures 1 and 2. SPN ratings are summarized in Table 3 and illustrated in Figures 3 and 4. Mean risk class shifts after the disclosure of BIMC data were 37.14 (39.5%) out of 94 ratings. Mean risk class of benign SPNs before and after CAD results was 2.48 and 2.29, respectively. Mean risk class of malignancies before and after CAD results was 3.66 and 3.92, respectively. Mean indeterminate SPNs (both benign and malignant nodules in class 3) were 23.86 and 15 before and after awareness of CAD predictions, respectively. Mean correct confident diagnoses (benign nodules in class 1 and malignant nodules in class 5) were 25.71 and 39.57 before and after awareness of CAD predictions, respectively.

Mean correct diagnosis shift (benign nodules with a lesser score or malignant nodules with a higher score after CAD disclosure) was 26.42.

Lung cancer is currently one of the leading causes of cancer deaths worldwide[10]. Most patients are diagnosed at an advanced stage and only about 15% have the opportunity of surgical resection[11]. Accurate assessment, proper treatment and timely surgical resection of malignant pulmonary nodules will be highly beneficial to the survival of patients with lung cancer.

SPNs are a common radiological finding at CT[1] and they often represent a diagnostic challenge for the physician because of substantial overlap of imaging signs between malignant and benign disease. Furthermore the differential diagnosis of a solid solitary pulmonary nodule is broad, ranging from benign tumors, infectious lesions to primary cancer. Typical findings at high-resolution CT are illustrated in Figures 5 and 6.

The cornerstone of nodule assessment is to estimate the likelihood of malignancy, since accurate determination of the nature of an SPN has critical consequences. In the case of a high-risk nodule the patient undergoes surgery while SPNs looking less aggressive are often monitored by serial imaging or characterized by tissue biopsy. Clinical prediction models, also referred to as risk

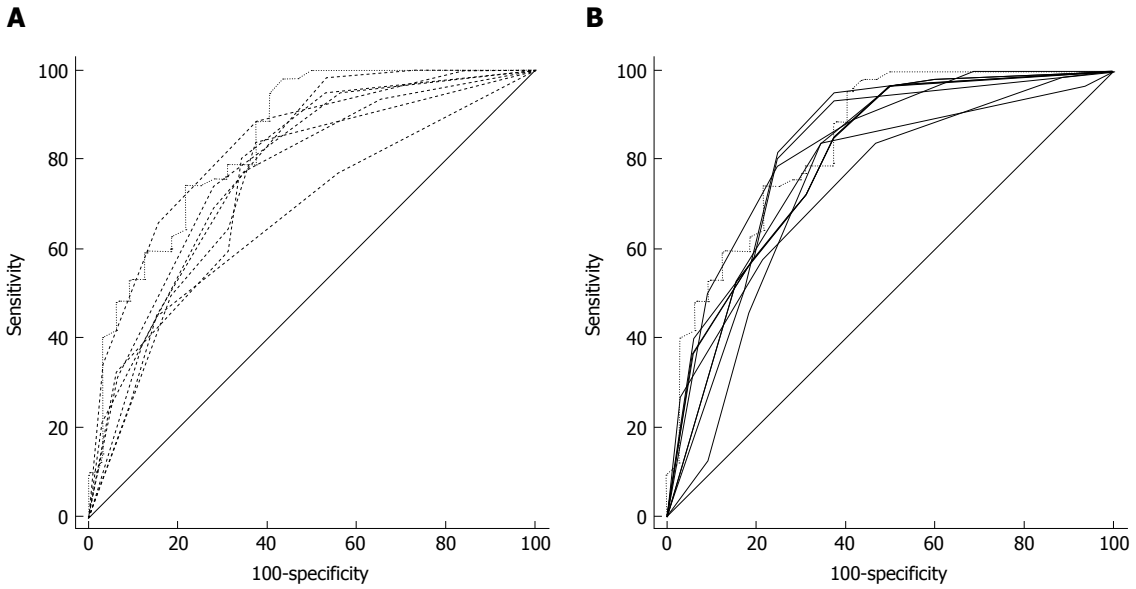

Figure 1 Graphical representation of raters' receiver operating characteristic curves before (A) and after (B) computer-aided diagnosis results disclosure. The Bayesian Inference Malignancy Calculator model receiver operating characteristic curve is recognizable as a staircase shaped dotted-line. A net shift towards the upper-left corner is noted from A to B.

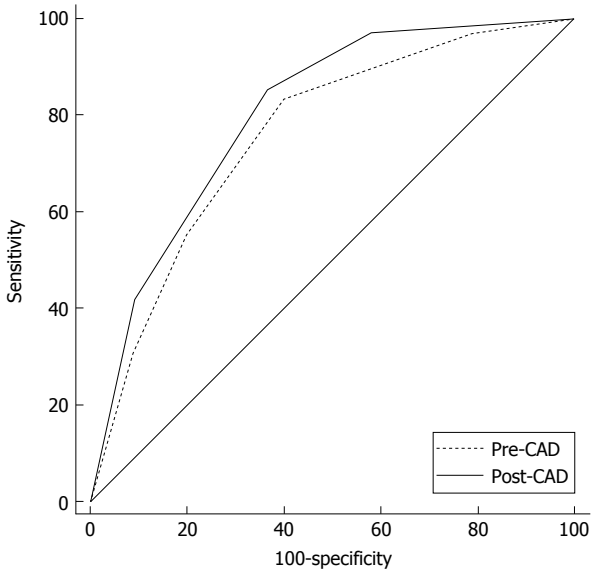

Figure 2 Graphical representation of overall receiver operating characteristic curve comparison. Post-computer-aided diagnosis receiver operating characteristic curve (solid line) is constantly superior to the pre-computer-aided diagnosis curve (dotted line). CAD: Computer-aided diagnosis.

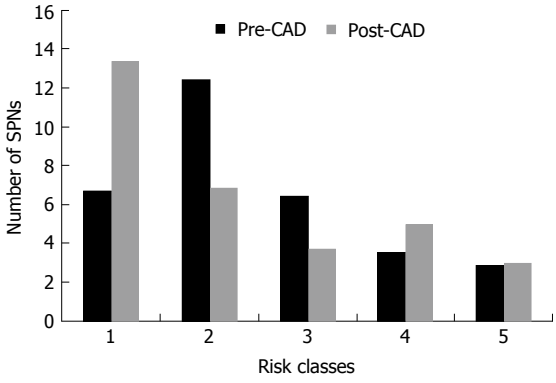

Figure 3 Graphical representation of benign solitary pulmonary nodule classification before (pre-computer-aided diagnosis) and after (post-computer-aided diagnosis) computer-aided diagnosis result disclosure. CAD: Computer-aided diagnosis; SPNs: Solitary pulmonary nodules.

assessment models, have been developed to provide a more explicit, transparent, and reproducible assessment of the risk[12]. In the past years a few studies have reported that CAD systems can help the radiologist to better detect and characterize SPNs on CT scans[13-16]. Although a number of proposals for the quantitative evaluation of SPNs have been offered, at present there is no consensus regarding the optimal approach[17]. The main purpose of this research was to assess whether and to what extent and significance CAD integration could help radiologists in better characterizing incidental solid SPNs during the work-up.

The most important and clinically relevant finding in this study is that the integration of the proposed prediction model significantly enhanced SPN characterization by increasing overall area under the curve (AUC) by 0.045 (P = 0.0003). This effect was less evident on single raters' AUC, probably because of the modest size of the sample evaluated. CAD integration increased to a variable extent the AUC for all raters but one (6 out of 7 raters) nonetheless.

A second crucial finding is the drop of nodules which were classified as indeterminate (class 3 in this study) for both malignant and benign lesions after CAD. It also led to an overall decrease of doubtful diagnoses (SPNs in classes 2, 3 and 4) and raised the number of correct confident diagnosis (benign SPNs in class 1 and malignant SPNs in class 5). A third noteworthy observation is that CAD integration did not cause an increase of cancer misdiagnoses (malignant SPNs in

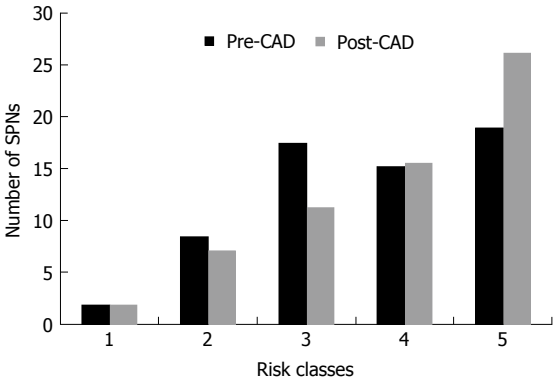

Figure 4 Graphical representation of malignant solitary pulmonary nodule classification before (pre-computer-aided diagnosis) and after (post-computer-aided diagnosis) computer-aided diagnosis result disclosure. CAD: Computer-aided diagnosis; SPNs: Solitary pulmonary nodules.

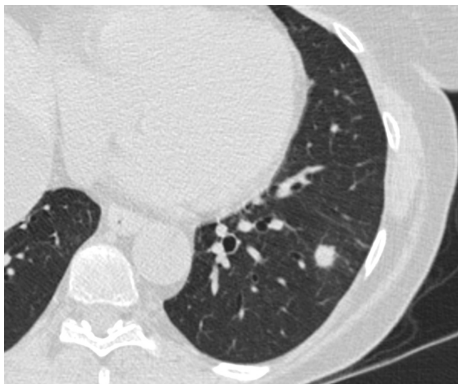

Figure 5 Typical appearance of an indeterminate solid pulmonary nodule at high-resolution computed tomography (Philips icomputed tomography, slice thickness 1.25 mm) in a 59-year-old female patient. The lesion was located in the left lower lobe, had a maximum diameter of 10 mm and proved to be a non-tubercular granuloma at surgery.

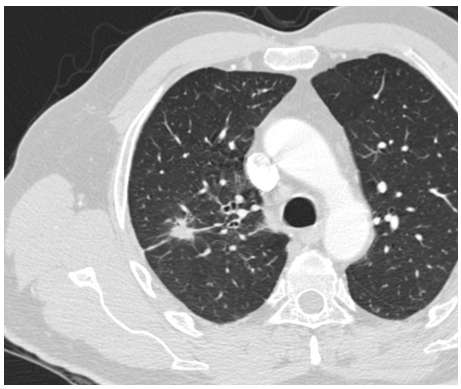

Figure 6 Typical appearance of a malignant solid pulmonary nodule at high-resolution computed tomography (Philips icomputed tomography, slice thickness 1.25 mm) in a 59-year-old male patient. The lesion was located in the right upper lobe, had a maximum diameter of 24 mm and proved to be an adenocarcinoma at surgery.

class 1), while only determining a modest increase of benign lesions being classified as probably (benign SPNs in class 4: Increased 1.43/32, 4.46%) or certainly malignant (benign SPNs in class 5: Increased 0.14/32, 0.43%). Overall comparison of ratings showed a higher mean confidence by lowering mean risk class of benign nodules from 2.48 to 2.29 and by raising mean risk class of malignancies from 3.66 to 3.92. These results support the possibility of enhancing SPN characterization by integrating CAD in routine SPN analysis. They also show how the BIMC model is particularly able to increase confidence in malignant nodule characterization, without raising concern of cancer misses. A very moderate increase in the number of benign nodules which are wrongly classified as malignant could possibly be the main drawback of using the proposed CAD. In this regard the authors believe that a more accurate and prompt characterization of malignant nodules can be worth the cost of very few benign nodules that would need further testing or will eventually undergo surgery.

One collateral finding of the current analysis is that the BIMC model alone showed persistent superiority to all human raters in providing correct predictions of risk. A note of caution is due here since the study was not designed to provide direct, unbiased comparison between raters and the model itself, and results may be limited by the methods adopted.

Whether models alone could perform better than clinicians is uncertain. Swensen, for example, showed that there was no difference in accuracy between the judgment of four expert physicians and the probabilities generated by the Mayo Clinic model, although it was noted how the experts tended to overestimate risk for nodules identified as low risk by the model[16]. Since this kind of analysis was beyond the scope and the methods of the study, these results need therefore to be interpreted with caution.

Our analysis suffers from some limitations. In the first place we did not consider the time needed to enter data in the calculator and obtain a CAD estimated value. Additional time requested in nodule assessment could possibly be detrimental to the clinical introduction of the described model. This was beyond the aim of the study and could be better assessed in future work. We eventually estimated the mean time spent on the web BIMC calculator for a single prediction by asking three radiologists to perform a risk prediction using the model. Time needed varied from less than 1 min for the very experienced (model designer and programmer, not included into raters) to roughly 4 min for the less skilled user (first time user, not included into raters). In the second place we solely focused on incremental accuracy of the CAD integrated method in SPN characterization. Additional studies are needed to clarify the value of prediction models above clinical judgment and to assess whether they can improve care and outcomes for patients presenting with an SPN.

Our results indicate that use of an integrated CAD and human judgment system can lead to improved raters' performance in SPN characterization on chest CT images.

This study provides evidence supporting the integration of CAD in SPN assessment. The BIMC prediction

model can assist radiologists in better distinguishing malignant from benign SPNs.

REFERENCES

1 **Trotman-Dickenson B**, Baumert B. Multidetector-row CT of the solitary pulmonary nodule. *Semin Roentgenol* 2003; **38**: 158-167 [PMID: 12854439 DOI: 10.1016/S0037-198X(03)00018-X]

2 **Wang YX**, Gong JS, Suzuki K, Morcos SK. Evidence based imaging strategies for solitary pulmonary nodule. *J Thorac Dis* 2014; **6**: 872-887 [PMID: 25093083 DOI: 10.3978/j.issn.2072-1439.2014.07.26]

3 **Sim YT**, Poon FW. Imaging of solitary pulmonary nodule-a clinical review. *Quant Imaging Med Surg* 2013; **3**: 316-326 [PMID: 24404446 DOI: 10.3978/j.issn.2223-4292.2013.12.08]

4 **Gould MK**, Fletcher J, Iannettoni MD, Lynch WR, Midthun DE, Naidich DP, Ost DE. Evaluation of patients with pulmonary nodules: when is it lung cancer?: ACCP evidence-based clinical practice guidelines (2nd edition). *Chest* 2007; **132**: 108S-130S [PMID: 17873164 DOI: 10.1378/chest.07-1353]

5 **Patel VK**, Naik SK, Naidich DP, Travis WD, Weingarten JA, Lazzaro R, Gutterman DD, Wentowski C, Grosu HB, Raoof S. A practical algorithmic approach to the diagnosis and management of solitary pulmonary nodules: part 1: radiologic characteristics and imaging modalities. *Chest* 2013; **143**: 825-839 [PMID: 23460160 DOI: 10.1378/chest.12-0960]

6 **Swensen SJ**, Jett JR, Sloan JA, Midthun DE, Hartman TE, Sykes AM, Aughenbaugh GL, Zink FE, Hillman SL, Noetzel GR, Marks RS, Clayton AC, Pairolero PC. Screening for lung cancer with low-dose spiral computed tomography. *Am J Respir Crit Care Med* 2002; **165**: 508-513 [PMID: 11850344 DOI: 10.1164/ajrccm.165.4.2107006]

7 **Zhao B**, Gamsu G, Ginsberg MS, Jiang L, Schwartz LH. Automatic detection of small lung nodules on CT utilizing a local density maximum algorithm. *J Appl Clin Med Phys* 2003; **4**: 248-260 [PMID: 12841796 DOI: 10.1120/1.1582411]

8 **Soardi GA**, Perandini S, Motton M, Montemezzi S. Assessing probability of malignancy in solid solitary pulmonary nodules with a new Bayesian calculator: improving diagnostic accuracy by means of expanded and updated features. *Eur Radiol* 2015; **25**: 155-162 [PMID: 25182626 DOI: 10.1007/s00330-014-3396-2]

9 **DeLong ER**, DeLong DM, Clarke-Pearson DL. Comparing the areas under two or more correlated receiver operating characteristic curves: a nonparametric approach. *Biometrics* 1988; **44**: 837-845 [PMID: 3203132 DOI: 10.2307/2531595]

10 **Jemal A**, Bray F, Center MM, Ferlay J, Ward E, Forman D. Global cancer statistics. *CA Cancer J Clin* 2011; **61**: 69-90 [PMID: 21296855 DOI: 10.3322/caac.20107]

11 **Zhan P**, Xie H, Xu C, Hao K, Hou Z, Song Y. Management strategy of solitary pulmonary nodules. *J Thorac Dis* 2013; **5**: 824-829 [PMID: 24409361 DOI: 10.3978/j.issn.2072-1439.2013.12.13]

12 **Gould MK**, Ananth L, Barnett PG. A clinical model to estimate the pretest probability of lung cancer in patients with solitary pulmonary nodules. *Chest* 2007; **131**: 383-388 [PMID: 17296637 DOI: 10.1378/chest.06-1261]

13 **Choi EJ**, Jin GY, Han YM, Lee YS, Kweon KS. Solitary pulmonary nodule on helical dynamic CT scans: analysis of the enhancement patterns using a computer-aided diagnosis (CAD) system. *Korean J Radiol* 2008; **9**: 401-408 [PMID: 18838848 DOI: 10.3348/kjr.2008.9.5.401]

14 **Rubin GD**, Lyo JK, Paik DS, Sherbondy AJ, Chow LC, Leung AN, Mindelzun R, Schraedley-Desmond PK, Zinck SE, Naidich DP, Napel S. Pulmonary nodules on multi-detector row CT scans: performance comparison of radiologists and computer-aided detection. *Radiology* 2005; **234**: 274-283 [PMID: 15537839 DOI: 10.1148/radiol.2341040589]

15 **Way TW**, Hadjiiski LM, Sahiner B, Chan HP, Cascade PN, Kazerooni EA, Bogot N, Zhou C. Computer-aided diagnosis of pulmonary nodules on CT scans: segmentation and classification using 3D active contours. *Med Phys* 2006; **33**: 2323-2337 [PMID: 16898434 DOI: 10.1118/1.2207129]

16 **Swensen SJ**, Silverstein MD, Edell ES, Trastek VF, Aughenbaugh GL, Ilstrup DM, Schleck CD. Solitary pulmonary nodules: clinical prediction model versus physicians. *Mayo Clin Proc* 1999; **74**: 319-329 [PMID: 10221459 DOI: 10.4065/74.4.319]

17 **Naidich DP**, Bankier AA, MacMahon H, Schaefer-Prokop CM, Pistolesi M, Goo JM, Macchiarini P, Crapo JD, Herold CJ, Austin JH, Travis WD. Recommendations for the management of subsolid pulmonary nodules detected at CT: a statement from the Fleischner Society. *Radiology* 2013; **266**: 304-317 [PMID: 23070270 DOI: 10.1148/radiol.12120628]

P- Reviewer: Chow J, Demir Y, Lassandro F **S- Editor**: Qiu S
L- Editor: Wang TQ **E- Editor**: Zhang FF

World Journal of Radiology

Submit a Manuscript: http://www.wjgnet.com/esps/
Help Desk: http://www.wjgnet.com/esps/helpdesk.aspx
DOI: 10.4329/wjr.v8.i8.735

World J Radiol 2016 August 28; 8(8): 735-742
ISSN 1949-8470 (online)

ORIGINAL ARTICLE

Retrospective Study

Helical tomotherapy and volumetric modulated arc therapy: New therapeutic arms in the breast cancer radiotherapy

Olivier Lauche, Youlia M Kirova, Pascal Fenoglietto, Emilie Costa, Claire Lemanski, Celine Bourgier, Olivier Riou, David Tiberi, Francois Campana, Alain Fourquet, David Azria

Olivier Lauche, Youlia M Kirova, Emilie Costa, Francois Campana, Alain Fourquet, Department of Radiation Oncology, Institut Curie, 75005 Paris, France

Pascal Fenoglietto, Claire Lemanski, Celine Bourgier, Olivier Riou, David Azria, Departement of Radiation Oncology, Institut du Cancer de Montpellier, 34298 Montpellier cedex 5, France

David Tiberi, Department of Radiation Oncology, Centre Hospitalier de l'Université de Montréal Hôpital Notre Dame, Montreal H2L 4M1, Canada

Author contributions: Lauche O and Kirova YM participated in the conception, acquisition, analysis, interpretation of the data and drafted the initial manuscript; Kirova YM and Azria D were the guarantor and designed the study; Fenoglietto P participated in the analysis and the interpretation of the data; Costa E, Lemanski C, Bourgier C, Riou O and Fourquet A revised the article critically for important intellectual content; Language revision was realized by Tiberi D from Canada (native speaker); Campana F participated in the treatment of the patients and revised the article.

Institutional review board statement: The study was reviewed and approved by the Breast Cancer Groups of Curie Institute and Montpellier Cancer Institute.

Informed consent statement: Not applicable given the retrospective design of our study.

Conflict-of-interest statement: There are no conflicts of interest to report.

Data sharing statement: No additional data are available.

Manuscript source: Invited manuscript

Correspondence to: Youlia M Kirova, MD, Chief of breast cancer research and treatment in the Department of Radiation Oncology, Institut Curie, 26, rue d'Ulm, 75005 Paris, France. youlia.kirova@curie.fr
Telephone: +33-1-44324193
Fax: +33-1-44324616

Received: February 23, 2016
Peer-review started: February 25, 2016
First decision: April 15, 2016
Revised: May 12, 2016
Accepted: June 27, 2016
Article in press: June 29, 2016
Published online: August 28, 2016

Abstract

AIM

To analyse clinical and dosimetric results of helical tomotherapy (HT) and volumetric modulated arc therapy (VMAT) in complex adjuvant breast and nodes irradiation.

METHODS

Seventy-three patients were included (31 HT and 42 VMAT). Dose were 63.8 Gy (HT) and 63.2 Gy (VMAT) in the tumour bed, 52.2 Gy in the breast, 50.4 Gy in supraclavicular nodes (SCN) and internal mammary chain (IMC) with HT and 52.2 Gy and 49.3 Gy in IMC and SCN with VMAT in 29 fractions. Margins to particle tracking velocimetry were greater in the VMAT cohort (7 mm *vs* 5 mm).

RESULTS

For the HT cohort, the coverage of clinical target volumes was as follows: Tumour bed: 99.4% ± 2.4%; breast: 98.4% ± 4.3%; SCN: 99.5% ± 1.2%; IMC:

96.5% ± 13.9%. For the VMAT cohort, the coverage was as follows: Tumour bed: 99.7% ± 0.5%, breast: 99.3% ± 0.7%; SCN: 99.6% ± 1.4%; IMC: 99.3% ± 3%. For ipsilateral lung, Dmean and V20 were 13.6 ± 1.2 Gy, 21.1% ± 5% (HT) and 13.6 ± 1.4 Gy, 20.1% ± 3.2% (VMAT). Dmean and V30 of the heart were 7.4 ± 1.4 Gy, 1% ± 1% (HT) and 10.3 ± 4.2 Gy, 2.5% ± 3.9% (VMAT). For controlateral breast Dmean was 3.6 ± 0.2 Gy (HT) and 4.6 ± 0.9 Gy (VMAT). Acute skin toxicity grade 3 was 5% in the two cohorts.

CONCLUSION

HT and VMAT in complex adjuvant breast irradiation allow a good coverage of target volumes with an acceptable acute tolerance. A longer follow-up is needed to assess the impact of low doses to healthy tissues.

Key words: Three-dimensional conformal radiotherapy; Intensity modulated radiation therapy; Toxicity; Helical tomotherapy; Volumetric modulated arc therapy; Breast cancer radiotherapy

Core tip: Using conventional techniques in breast and nodes irradiation, there could be suboptimal target coverage or great dose exposure to the normal structures. Our study suggests that helical tomotherapy (HT) and volumetric modulated arc therapy (VMAT) plans provide excellent target volume coverage and reduces high doses to organs at risk with an acceptable acute toxicity. At the same time, HT and VMAT deliver lower doses to larger volumes of normal tissues, suggesting in some cases an increased risk of second cancer. Nevertheless, the risk to benefit ratio seems to be in favour of HT and VMAT as opposed to three-dimensional conformal radiation therapy in complex target volumes, such as funnel chest, tumor in the inner quadrant when internal mammary chain and tumor bed boost are indicated, large breast size or unfavourable cardiac anatomy.

Lauche O, Kirova YM, Fenoglietto P, Costa E, Lemanski C, Bourgier C, Riou O, Tiberi D, Campana F, Fourquet A, Azria D. Helical tomotherapy and volumetric modulated arc therapy: New therapeutic arms in the breast cancer radiotherapy. *World J Radiol* 2016; 8(8): 735-742 Available from: URL: http://www.wjgnet.com/1949-8470/full/v8/i8/735.htm DOI: http://dx.doi.org/10.4329/wjr.v8.i8.735

INTRODUCTION

Adjuvant breast radiation therapy is standard of care after breast conserving surgery in early breast cancer, improving disease free survival and overall survival (OS)[1]. Benefit of lymph node irradiation [internal mammary chain (IMC) and supra and infra clavicular nodes (SN)] in patients with axillary lymph node involvement or at high risk of relapse has been shown by a meta-analysis of three randomised trials (MA.20, European Organisation for Research and Treatment of Cancer 22922/10925 and the Lyon breast cancer trial)[2]. Lymph nodes irradiation resulted in a significant improvement of OS [hazard ratio (HR) 0.88 (95%CI: 0.75-0.97)], disease free survival [HR 0.85 (95%CI: 0.77-0.94)] and distant metastasis free survival [HR 0.82 (95%CI: 0.73-0.92)]. In these trials, separated fields for breast and lymph nodes irradiation were used in two-dimensional (2D) or three-dimensional conformal radiation therapy (3D-CRT) treatment delivery. In recent years, intensity modulated radiation therapy (IMRT) has been developed to lessen organs at risk (OAR) exposure to high doses. Static breast cancer IMRT significantly reduced acute and late skin toxicity compared to standard techniques in 3 phase Ⅲ randomised trials[3-5]. Then static IMRT techniques moved to helical tomotherapy (HT) or volumetric modulated arc therapy (VMAT) for pelvic and head and neck cancers. These two techniques (VMAT and HT) have been recently performed and assessed in breast cancers. Dosimetrics studies showed that HT or VMAT improved target volume coverage, allowed better dose homogeneity and decreased high doses to OAR compared to 3D-CRT[6-11]. At the other hand these two techniques increased low doses to OAR suggesting the possibility of greater risk for secondary malignancies[12].

Using conventional techniques in breast and nodes irradiation, field junction may result in a cold or hot spot and in complex cases (unfavourable cardiac anatomy, tumour in the inner quadrants, funnel chest for example) there could be suboptimal target coverage or great dose exposure to the normal structures. Some dosimetrics studies suggested a benefit of HT or VMAT in complex breast irradiations[13-17] but no large studies evaluated clinical results.

The purpose of this study is to report the clinical and dosimetrics results for patients treated with HT or VMAT using simultaneous integrated boost (SIB) in the setting of complex adjuvant breast and nodes irradiation.

MATERIALS AND METHODS

A bi-centric retrospective study of breast cancer patients with complex anatomy and treated by HT or VMAT was conducted. Patients included in our study were treated from September 2010 to November 2013 in the HT cohort (n = 31) and from February 2011 to October 2013 (n = 42) in the VMAT cohort.

Patients' selection

Inclusion criteria were: Stage Ⅰ/Ⅲ invasive breast cancers patients, breast conserving surgery, indication of lymph node irradiation (IMC, supraclavicular nodes ± axillary nodes). Patients with unacceptable dosimetry according to International Commission on Radiation Units and Measurements and Units 62 using 3D-CRT were selected

Table 1 Definition of planning target volume

	HT	VMAT
Breast PTV	[Breast CTV + 5 mm - (PTV tumor bed + 2 mm)] - 3 mm cutaneous	[Breast CTV + 7 mm - (PTV tumor bed + 2 mm)] - 5 mm cutaneous
Tumor bed PTV	(CTV tumor bed + 5 mm) - 3 mm cutaneous	(CTV tumor bed + 7 mm) - 5 mm cutaneous
Supra infra clavicular ± axillary PTV	(CTV SN + 5 mm) - 3 mm cutaneous	(CTV SN ± axillary + 7 mm) - 5 mm cutaneous
IMC PTV	(CTV IMC + 5 mm) - PTV breast	CTV IMC + 7 mm

PTV: Planning target volume; CTV: Clinical target volume; IMC: Internal mammary chain; SN: Supra and infra clavicular nodes (Levels II-III-IV); HT: Helical tomotherapy; VMAT: Volumetric modulated arc therapy.

for treatment using HT or VMAT by the treating radiation oncologist. The indication to proceed with HT or VMAT was validated at a quality control meeting comprised of staff radiation oncologists specializing in breast cancer. Patients with distant metastases, indication of bilateral breast irradiation and treated with total mastectomy with immediate breast reconstruction were excluded.

Institutional HT and VMAT indications

HT and VMAT indications were funnel chest (HT series and VMAT series respectively 11% and 5%), large breast size (5% and 17%), tumour in the inner quadrant (38% and 16%), interbreast reduced space (11% and 0%), axillary irradiation (0% and 19%) and suboptimal dosimetry (35% and 43%).

Patient immobilization

Patients were treated in the supine position, both arms above the head in both institutes.

Compared to 3D-CRT, when patients were treated with these two highly conformal techniques, contentions were added to limit set-up errors: A cervical thermoplastic immobilization was used in the HT group and a back Moldcare® was used in the VMAT group.

Target volumes: Definition and delineation

The CT data were transferred to a commercial treatment planning system in the two series (Eclipse 3D version 8.1; Varian Medical Systems Inc., Palo Alto, United States).

Clinical target volumes (CTVs) were the same when using 3D-CRT: The breast CTV was delineated using radiopaque markers defined at the clinical examination before the planning CT, nodal delineation was performed using established guidelines[16,17] and tumour bed boost was delineated using surgical clips, initial mammogram and postoperative scar[18]. There was an expansion of all CTVs, in all directions, of 5 mm (HT) and 7 mm (VMAT), except for the skin (Table 1). The planning target volume provided a margin around the CTV to compensate for the variability of treatment setup and motion of the breast with breathing[19]. Margins from CTV to PTV are different between the two groups, so we decided to present here the results of CTV coverage.

OAR delineation

The heart was delineated from the apex to the roots of the major vessels and included pericardial fat. Lungs, spinal cord, thyroid and oesophagus were delineated entirely. Contralateral breast was defined using radiopaque markers defined at the clinical exam. Unspecified normal tissue corresponded to the volume enclosed by the whole patient skin contours.

Dose prescription

All patients were treated with SIB. With SIB, the planning and delivery of whole breast and boost radiotherapy are integrated into a single plan that is used for the whole treatment course, with patients receiving a differential dose to the whole breast and to the tumor bed for every fraction. The reduction in overall treatment time and the increased dose per fraction to the tumor bed can also theoretically lead to improve local control[20]. In breast cancer treated with SIB, HT avoided unnecessary breast overdosage compared to 3D-CRT[21]. Treatments were in 29 fractions (f) in the both series. The dose to breast PTV was similar in both groups (52.2 Gy). 63.8 Gy (2.2 Gy/f) and 63.2 Gy (2.18 Gy/f) were delivered to the tumor bed respectively for HT and VMAT, 50.4 Gy (1.74 Gy/f) and 49.3 Gy (1.7 Gy/f) to the SN ± axillary nodes and 50,4Gy (1.74 Gy/f) and 52.2 Gy (1.8 Gy/f) to the IMC.

For a tumor α/β of 4[20], HT and VMAT fractionation schedule are respectively radiobiologically equivalent in 2 Gy fractions to 50.5 Gy in the whole breast, 65.9 Gy and 65.3 Gy to the tumor bed, 48.2 Gy and 46.8 Gy to the SN ± axillary nodes and 48.2 Gy and 50.5 Gy in the IMC.

HT and VMAT planning

For HT planning, the CT data and the structure sets were transferred to the TomoTherapy planning station (TomoTherapy HI-ART version 3.1.2.3; TomoTherapy Inc., Madison, United States). All plans used a jaw width of 2.5 cm, a pitch of 0.286 and a modulation factor of 2.5.

VMAT optimization was performed using the treatment planning system Eclipse version 8.9 (Helios, Varian, Palo Alto, CA). The plans were delivered in a Varian 21EX linear accelerator (Varian, Palo Alto, CA).

Toxicity assessment

Acute oesophageal, lung and skin toxicity were assessed retrospectively using Common Terminology Criteria for Adverse Events v.3.0. A clinical exam was weekly performed during radiotherapy and one and three

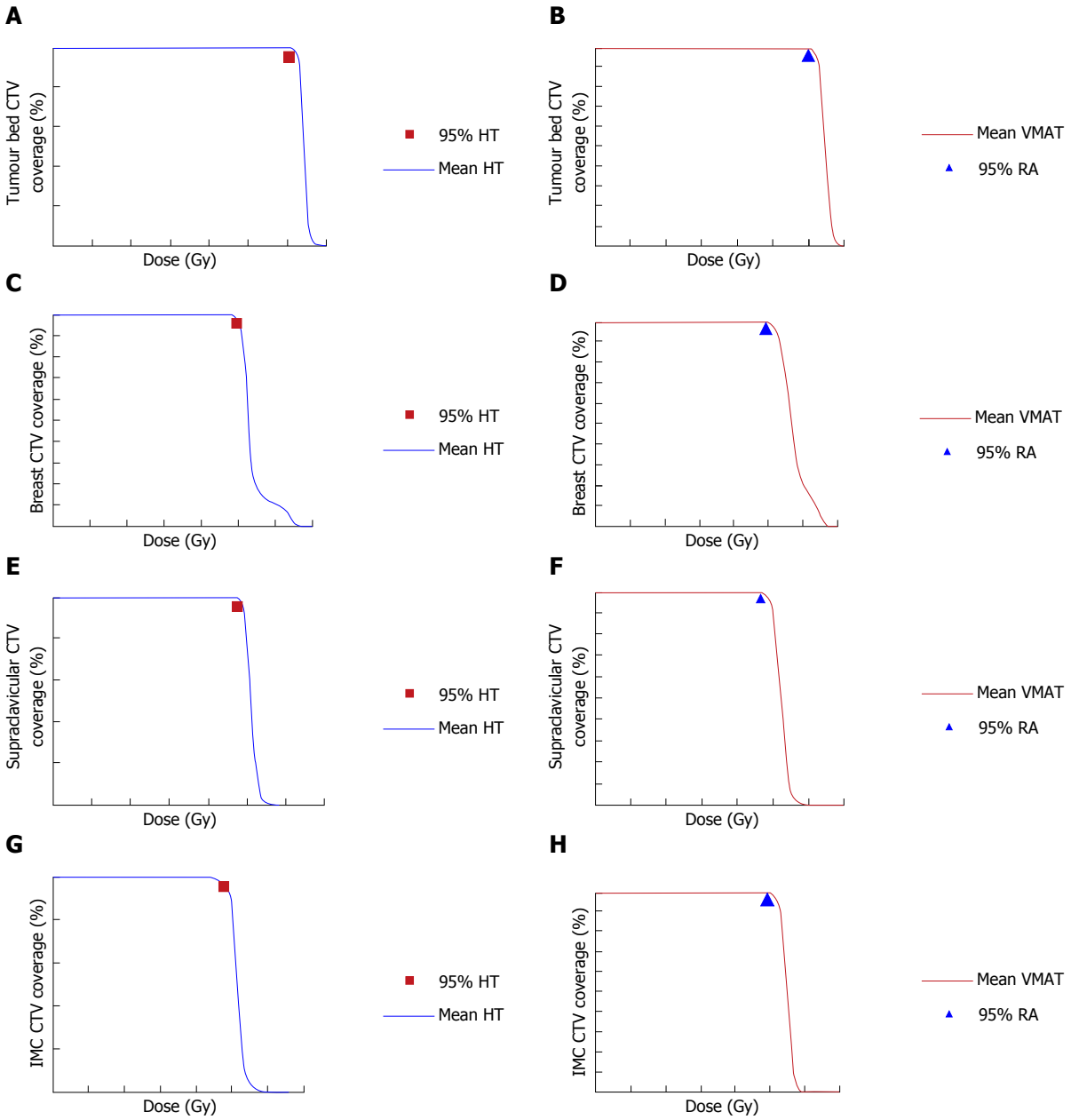

Figure 1 Dose volume histogram of clinical target volume. A, C, E and G: HT; B, D, F and H: VMAT. A and B: Tumour bed CTV; C and D: Breast CTV; E and F: Supra-infra clavicular ± axillary nodes CTV; G and H: IMC CTV. 95% HT: Breast CTV volume covered by 95% of the dose delivered by HT; 95% VMAT: Breast CTV volume covered by 95% of the dose delivered by VMAT; HT: Helical tomotherapy; VMAT: Volumetric modulated arc therapy; CTV: Clinical target volume; IMC: Internal mammary chain; RA: Rapid arc.

months following the completion of radiotherapy.

RESULTS

Patient characteristics

Patient's characteristics are summarized in Table 2. Clinical characteristics, biological and prognostic factors were equally balanced in the two series except for inner quadrants tumours location.

Target volumes coverage

Tumour bed CTV: CTV V95 was 99.7% ± 0.1% with HT and 99.7% ± 0.5% with VMAT (Figure 1A and B).

Breast CTV: The breast CTV V95 was 98.4% ± 4.3% with HT and 99.3% ± 0.7% with VMAT (Figure 1C and D).

Supra and infra clavicular ± axillary nodes CTV: The supraclavicular ± axillary nodes CTV V95 were 99.6% ± 1.2% with HT and 99.3% ± 3% with VMAT (Figure 1E and F).

IMC CTV: The IMC CTV V95 was 96.5% ± 13.9% with HT and 99.6% ± 1.7% with VMAT (Figure 1G and H).

Dose to normal tissues

Doses to normal tissues are summarized in Table 3.

Table 2 Patient's characteristics

	HT (n = 31)	VMAT (n = 42)
Age	50	52
Laterality		
Right	56.8%	50%
Left	43.2%	50%
Quadrant		
IQ	70.2%	40%
Outer quadrants	29.8%	60%
Size (mm)	25.4	25
N stage		
N0	37.8%	21%
N1	48.6%	42%
N2	13.5%	23%
N3	0%	14%
Grade		
1	2.7%	7%
2	45.9%	31%
3	51.4%	62%
LVI		
-	59.5%	77%
+	40.5%	23%
Hormone receptors		
RH+	76%	77%
RH-	24%	29%
Triple negative	18.9%	24%
HER2		
+	16.2%	14%
-	83.8%	86%
Tobacco	16.2%	20.9%
BMI (kg/m^2)	25.8	25.9
Chemotherapy		
Neoadjuvant	30%	29%
Adjuvant	49%	64%
Concurrent	4%	0%
Irradiation N		
SN	100%	98%
IMC	100%	100%
Axillary	16.2%	19%

HT: Helical tomotherapy; VMAT: Volumetric modulated arc therapy; BMI: Body mass index; LVI: Lymphovascular invasion; SN: Supra and infra clavicular nodes (Levels II-III-IV); IMC: Internal mammary chain; RH: Hormonal receptor; HER2: Human epidermal growth factor receptor-2; IQ: Inner quadrant.

Table 3 Doses to normal tissues

	VMAT	HT
Ipsilateral lung		
V5	85.3% ± 9.6%	78.5% ± 12.6%
V20	20.1% ± 3.2%	21.1% ± 5%
V30	8.8% ± 3.2%	10.1 ± 3.3
Mean dose	13.6 ± 1.4 Gy	13.6 ± 1.2 Gy
Controlateral lung		
V5	46% ± 14.1%	35.4 ± 11.3
V20	0.7% ± 0.5%	0.1 ± 0.2
Mean dose	5.4 ± 1 Gy	4.6 ± 0.8 Gy
Heart		
Mean dose	10.3 ± 4.2 Gy	7.5 ± 1.4 Gy
V5	77.6% ± 21%	59.8 % ± 14.6%
V30	2.5% ± 3.9%	1% ± 1%
Controlateral breast		
Mean dose	4.6 ± 0.9 Gy	3.6 ± 0.6 Gy
V5	32% ± 11.9%	14.7% ± 7%
Spinal cord		
V40	0 mm^3	0 mm^3
V5	22.4 ± 8.8 mm^3	25.2 ± 9 mm^3
Oesophagus		
V45	0.4 ± 0.6 mm^3	1 ± 1.2 mm^3
V10	8.8 ± 5.4 mm^3	12.8 ± 5.7 mm^3
Thyroid		
Mean dose	28.3 ± 7 Gy	26.7 ± 7.7 Gy
V30	44% ± 15.3%	39.8% ± 17.6%
V5	97.1% ± 8.3%	96% ± 9.4%
Unspecified tissues		
V40	1977 ± 911 mm^3	1880.9 ± 754
V5	9770.3 ± 2551 mm^3	8566.6 ± 1946.2

VMAT: Volumetric modulated arc therapy; HT: Helical tomotherapy.

There were little exposure of normal tissues to high doses; instead there were high volumes of normal tissues encompassed by small doses irradiation. Lung exposure and dosimetric constraints matched with Société Française Radiothérapie Oncologique (SFRO) recommendations[22] with V30 ipsilateral lung < 20% (8.8% ± 3.2% for VMAT and 10% ± 3% for HT) and V20 < 30% (20.1% ± 3.2% for VMAT and 20.9% ± 4.9% for HT).

Acute toxicity

A maximum of 5% of grade 3 acute skin toxicity was observed regardless VMAT or HT use. Thirty-five percent (HT) and 40% (VMAT) grade ⩽ 2 oesophagus toxicity was noticed. No lung toxicity was observed.

DISCUSSION

HT and VMAT could be an interesting option in case of complex anatomical cases of breast cancer patients by offering adequate and optimal target volumes coverage while lessening OAR exposure. Our results showed that 95% isodose covered at least 95% of PTV regardless IMRT techniques in case of funnel chest anatomy (Figure 2A), unfavourable cardiac anatomy (Figure 2B) or obese patients with superposition of breast and nodal volumes (Figure 2C).

A previous study, which assess the benefit of adjuvant breast hypo fractionated irradiation with HT, reported only 8% of grade ⩾ 3 acute skin toxicity and 10% of grade ⩾ 1 lung toxicity two months after treatment[23]. In this study only 13 patients received supraclavicular, infraclavicular and axillary irradiation and no patients received IMC irradiation. Our study is the largest to report clinical outcomes in the setting of complex adjuvant breast and nodes irradiation, including IMC, treated with VMAT or HT. Our study showed a lower incidence of grade 3-4 acute skin toxicities (5%), rather than tolerance reported after static IMRT (27%)[4], probably because inverse plan IMRT improve dose homogeneity compare to forward plan IMRT[11,24], and improve dose homogeneity translate into lower acute skin toxicity[4]. To reduce severe acute skin toxicity is a real challenge in breast cancer radiotherapy as it is related to a poor cosmetic outcome[25,26]. Static IMRT decreased its incidence when compared to 3D-CRT, but seems to be less effective when compared to HT and VMAT. Moreover, we have not yet observed clinical radiation pneumonitis in

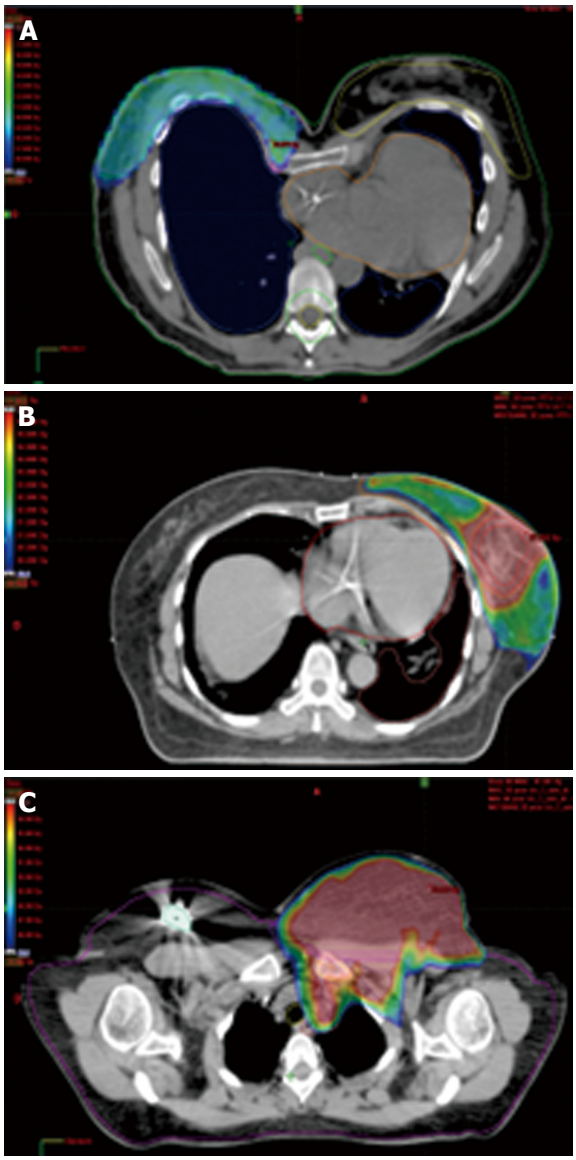

Figure 2 Dose distribution in difficult to irradiate cases. A: Breast irradiation with HT in a patient with funnel chest (isodose 45 Gy); B: Breast irradiation with HT in a patient with unfavourable cardiac anatomy (isodose 45 Gy); C: Breast and nodes irradiation with VMAT in an obese patient with superposition of breast and nodes volumes (isodose 45 Gy). HT: Helical tomotherapy; VMAT: Volumetric modulated arc therapy.

the two series while a meta-analysis mentioned a 14% incidence clinical radiation pneumonitis with 3D-CRT[27]. Given the negative selection bias towards patients with problematic anatomy, the favourable comparison of acute toxicity with historical trial data for a more standard cohort is encouraging.

To decrease the risk of late cardiac toxicity occurrence is one of the main challenges of breast cancer radiotherapy. Long-term breast cancer survivors are at high risk of cardiac events. Darby *et al*[28] showed an increased risk of ischemic heart disease (myocardial infarction, coronary revascularization, or death from ischemic heart disease) after breast cancer irradiation, which was related to the mean dose to the heart. No evident threshold has been observed but patients with pre-existing cardiac risk factors had a higher risk of developing such toxicities. This large cohort of patients was treated with standard 2D or 3D-conformal techniques of radiotherapy. The gain of the use of IMRT is to lessen heart exposure to high doses[6,8,9]. Our study reinforces these findings with a low value of V30Gy regardless HT or VMAT. However these techniques expose the heart to substantial low dose (V5Gy = 77.6% ± 21% in VMAT series and 59.8% ± 14.6% in HT series), which translates in a relative high mean heart dose [10.3 ± 4.2 Gy (VMAT) and 7.5 ± 1.4 Gy (HT)]. A longer follow-up is warranted to follow cardiac events occurrence after breast IMRT.

One limitation of the use of HT or VMAT in breast cancer is the lung exposure to low dose (*i.e.*, lesser than 5 Gy). Our study showed a significant lung volume exposure to dose lower than 5 Gy, which is higher than lung exposure after 2D or 3D-CRT[6,8,9]. Similarly to heart exposure, late consequences of low doses to the lung are unknown. A carefully follow-up should be considered in patients treated with HT or VMAT.

Other unknown factors still remain as the contralateral breast exposure. Contralateral breast is rarely exposed after conventional techniques of radiotherapy or after static IMRT[29]. Here, the use of HT or VMAT exposed contralateral breast volume to low dose (lesser than 5 Gy; 4.6 ± 0.9 Gy in VMAT series and 3.6 ± 0.6 Gy in HT series). The main uncertainty of low dose exposure after HT or VMAT is the risk of radio-induced cancer[30,31]. The risk of radio-induced breast cancer has been widely reported after Hodgkin irradiation and young age and dose were the main risk factors[29,32]. Hence, the use of HT or VMAT should be carefully considered in young patients.

When examining normal tissues as a whole, there was less exposure to high doses using rotational techniques[8,9,33]. However, there were high volumes of normal tissue encompassed by small doses of irradiation (unspecified tissue V5: 9770.3 ± 2551 mm^3 in VMAT cohort and 8566.6 ± 1946.2 mm^3 in HT cohort) suggesting the possibility of a greater risk for secondary cancer, which could be a concern for young patients[12].

In conclusion, HT and VMAT are feasible techniques in cases of complex adjuvant breast and nodal irradiation and provide excellent target volume coverage with an acceptable acute toxicity. As low dose distribution with HT or VMAT is large, a careful follow-up regarding lung, heart, contralateral breast is warranted.

Since uncertainties still remain regarding the role of low dose, this technique should only be considered to a selected population of breast cancer such as funnel chest, high breast volume, tumour in the inner quadrants, unfavourable cardiac anatomy.

COMMENTS

Background

Benefit of lymph node irradiation in patients with axillary lymph nodes involvement has been proven by the MA.20 and European Organisation for Research and Treatment of Cancer 22922/10925 trials. The benefit of lymph

node irradiation has been proven with two-dimensional or three-dimensional conformal radiation therapy techniques. In complex cases, there could be suboptimal target coverage or great dose exposure to the normal structures with standard techniques. Helical tomotherapy (HT) and volumetric modulated arc therapy (VMAT) are two techniques of rotational intensity modulated radiation therapy that provide excellent target volume coverage and reduce high doses to normal tissues. Some dosimetric studies suggested a benefit of HT or VMAT in complex breast irradiations but no large clinical studies evaluated clinical results.

Research frontiers

This study is the first to report the feasibility of HT and VMAT in case of complex adjuvant breast and nodal irradiation.

Innovations and breakthroughs

The rationale of the study is based on the complexity of the irradiation of lymph nodes and breast with standard techniques, which could be responsible of poor target volume coverage, or great dose exposure of the normal structures, especially in complex anatomies. This study is the largest to report clinical outcomes in the setting of complex adjuvant breast and nodes irradiation, including internal mammary chain, treated with VMAT or HT. The data suggest that HT and VMAT are attractive techniques in the setting of complex adjuvant breast and nodes irradiation allowing good target volume coverage with an acceptable acute toxicity.

Applications

This study suggests that HT and VMAT are feasible techniques in complex adjuvant breast and nodes irradiation. It provides readers with the necessary information (patients selection, patient immobilization, dose prescription, target volume and organs at risk delineation, HT and VMAT planning) to carry out HT and VMAT in the setting of complex breast and nodes irradiation.

Terminology

VMAT and HT are techniques of rotational intensity modulated radiation therapy. With VMAT, the beam radiation can be modulated by varying the gantry speed, move of the leafs and dose rate. HT is a 6-MV accelerator mounted on a ring gantry that rotates around the patient while the table advances slowly through the bore.

Peer-review

Very interesting and promising radiation management. This manuscript provides useful information to the medical students, clinicians, and researchers in this field.

REFERENCES

1 **Darby S**, McGale P, Correa C, Taylor C, Arriagada R, Clarke M, Cutter D, Davies C, Ewertz M, Godwin J, Gray R, Pierce L, Whelan T, Wang Y, Peto R. Effect of radiotherapy after breast-conserving surgery on 10-year recurrence and 15-year breast cancer death: meta-analysis of individual patient data for 10,801 women in 17 randomised trials. *Lancet* 2011; **378**: 1707-1716 [PMID: 22019144 DOI: 10.1016/S0140-6736(11)61629-2]

2 **Budach W**, Kammers K, Boelke E, Matuschek C. Adjuvant radiotherapy of regional lymph nodes in breast cancer - a meta-analysis of randomized trials. *Radiat Oncol* 2013; **8**: 267 [PMID: 24225206 DOI: 10.1186/1748-717X-8-267]

3 **Mukesh MB**, Barnett GC, Wilkinson JS, Moody AM, Wilson C, Dorling L, Chan Wah Hak C, Qian W, Twyman N, Burnet NG, Wishart GC, Coles CE. Randomized controlled trial of intensity-modulated radiotherapy for early breast cancer: 5-year results confirm superior overall cosmesis. *J Clin Oncol* 2013; **31**: 4488-4495 [PMID: 24043742 DOI: 10.1200/JCO.2013.49.7842]

4 **Pignol JP**, Olivotto I, Rakovitch E, Gardner S, Sixel K, Beckham W, Vu TT, Truong P, Ackerman I, Paszat L. A multicenter randomized trial of breast intensity-modulated radiation therapy to reduce acute radiation dermatitis. *J Clin Oncol* 2008; **26**: 2085-2092 [PMID: 18285602 DOI: 10.1200/JCO.2007.15.2488]

5 **Donovan E**, Bleakley N, Denholm E, Evans P, Gothard L, Hanson J, Peckitt C, Reise S, Ross G, Sharp G, Symonds-Tayler R, Tait D, Yarnold J. Randomised trial of standard 2D radiotherapy (RT) versus intensity modulated radiotherapy (IMRT) in patients prescribed breast radiotherapy. *Radiother Oncol* 2007; **82**: 254-264 [PMID: 17224195 DOI: 10.1016/j.radonc.2006.12.008]

6 **Popescu CC**, Olivotto IA, Beckham WA, Ansbacher W, Zavgorodni S, Shaffer R, Wai ES, Otto K. Volumetric modulated arc therapy improves dosimetry and reduces treatment time compared to conventional intensity-modulated radiotherapy for locoregional radiotherapy of left-sided breast cancer and internal mammary nodes. *Int J Radiat Oncol Biol Phys* 2010; **76**: 287-295 [PMID: 19775832 DOI: 10.1016/j.ijrobp.2009.05.038]

7 **Osman SO**, Hol S, Poortmans PM, Essers M. Volumetric modulated arc therapy and breath-hold in image-guided locoregional left-sided breast irradiation. *Radiother Oncol* 2014; **112**: 17-22 [PMID: 24825176 DOI: 10.1016/j.radonc.2014.04.004]

8 **Caudrelier JM**, Morgan SC, Montgomery L, Lacelle M, Nyiri B, Macpherson M. Helical tomotherapy for locoregional irradiation including the internal mammary chain in left-sided breast cancer: dosimetric evaluation. *Radiother Oncol* 2009; **90**: 99-105 [PMID: 18977546 DOI: 10.1016/j.radonc.2008.09.028]

9 **Goddu SM**, Chaudhari S, Mamalui-Hunter M, Pechenaya OL, Pratt D, Mutic S, Zoberi I, Jeswani S, Powell SN, Low DA. Helical tomotherapy planning for left-sided breast cancer patients with positive lymph nodes: comparison to conventional multiport breast technique. *Int J Radiat Oncol Biol Phys* 2009; **73**: 1243-1251 [PMID: 19251096 DOI: 10.1016/j.ijrobp.2008.11.004]

10 **Chira C**, Kirova YM, Liem X, Campana F, Peurien D, Amessis M, Fournier-Bidoz N, Pierga JY, Dendale R, Bey P, Fourquet A. Helical tomotherapy for inoperable breast cancer: a new promising tool. *Biomed Res Int* 2013; **2013**: 264306 [PMID: 24078909 DOI: 10.1155/2013/264306]

11 **Lauche O**, Kirova YM. Helical tomotherapy in breast cancer treatment. *Breast Cancer Manag* 2014; **3**: 441-449 [DOI: 10.2217/bmt.14.34]

12 **Abo-Madyan Y**, Aziz MH, Aly MM, Schneider F, Sperk E, Clausen S, Giordano FA, Herskind C, Steil V, Wenz F, Glatting G. Second cancer risk after 3D-CRT, IMRT and VMAT for breast cancer. *Radiother Oncol* 2014; **110**: 471-476 [PMID: 24444525 DOI: 10.1016/j.radonc.2013.12.002]

13 **Coon AB**, Dickler A, Kirk MC, Liao Y, Shah AP, Strauss JB, Chen S, Turian J, Griem KL. Tomotherapy and multifield intensity-modulated radiotherapy planning reduce cardiac doses in left-sided breast cancer patients with unfavorable cardiac anatomy. *Int J Radiat Oncol Biol Phys* 2010; **78**: 104-110 [PMID: 20004529 DOI: 10.1016/j.ijrobp.2009.07.1705]

14 **Lamberth F**, Guilbert P, Gaillot-Petit N, Champagne C, Looten-Vieren L, Nguyen TD. [Potential indications for helical tomotherapy in breast cancers]. *Cancer Radiother* 2014; **18**: 7-14 [PMID: 24314856 DOI: 10.1016/j.canrad.2013.07.148]

15 **Haertl PM**, Pohl F, Weidner K, Groeger C, Koelbl O, Dobler B. Treatment of left sided breast cancer for a patient with funnel chest: volumetric-modulated arc therapy vs. 3D-CRT and intensity-modulated radiotherapy. *Med Dosim* 2013; **38**: 1-4 [PMID: 22727550 DOI: 10.1016/j.meddos.2012.04.003]

16 **Kirova YM**, Castro Pena P, Dendale R, Servois V, Bollet MA, Fournier-Bidoz N, Campana F, Fourquet A. Simplified rules for everyday delineation of lymph node areas for breast cancer radiotherapy. *Br J Radiol* 2010; **83**: 683-686 [PMID: 20019174 DOI: 10.1259/bjr/28834220]

17 **Atean I**, Pointreau Y, Barillot I, Kirova YM. [Organs at risk and target volumes: definition for conformal radiation therapy in breast cancer]. *Cancer Radiother* 2012; **16**: 485-492 [PMID: 22925488 DOI: 10.1016/j.canrad.2012.06.002]

18 **Kirova YM**, Castro Pena P, Hijal T, Fournier-Bidoz N, Laki F, Sigal-Zafrani B, Dendale R, Bollet MA, Campana F, Fourquet A. Improving the definition of tumor bed boost with the use of surgical clips and image registration in breast cancer patients. *Int*

J Radiat Oncol Biol Phys 2010; **78**: 1352-1355 [PMID: 20381975 DOI: 10.1016/j.ijrobp.2009.10.049]
19 **Wiant DB**, Wentworth S, Maurer JM, Vanderstraeten CL, Terrell JA, Sintay BJ. Surface imaging-based analysis of intrafraction motion for breast radiotherapy patients. *J Appl Clin Med Phys* 2014; **15**: 4957 [PMID: 25493520 DOI: 10.1120/jacmp.v15i6.4957]
20 **Qi XS**, White J, Li XA. Is α/β for breast cancer really low? *Radiother Oncol* 2011; **100**: 282-288 [PMID: 21367477 DOI: 10.1016/j.radonc.2011.01.010]
21 **Hijal T**, Fournier-Bidoz N, Castro-Pena P, Kirova YM, Zefkili S, Bollet MA, Dendale R, Campana F, Fourquet A. Simultaneous integrated boost in breast conserving treatment of breast cancer: a dosimetric comparison of helical tomotherapy and three-dimensional conformal radiotherapy. *Radiother Oncol* 2010; **94**: 300-306 [PMID: 20171752 DOI: 10.1016/j.radonc.2009.12.043]
22 **Ortholan C**, Estivalet S, Barillot I, Costa A, Gérard JP. [Guide for external beam radiotherapy. Procedures 2007]. *Cancer Radiother* 2007; **11**: 329-330 [PMID: 17962059 DOI: 10.1016/j.canrad.2007.09.005]
23 **Van Parijs H**, Miedema G, Vinh-Hung V, Verbanck S, Adriaenssens N, Kerkhove D, Reynders T, Schuermans D, Leysen K, Hanon S, Van Camp G, Vincken W, Storme G, Verellen D, De Ridder M. Short course radiotherapy with simultaneous integrated boost for stage I-II breast cancer, early toxicities of a randomized clinical trial. *Radiat Oncol* 2012; **7**: 80 [PMID: 22656865 DOI: 10.1186/1748-717X-7-80]
24 **Yin Y**, Chen J, Sun T, Ma C, Lu J, Liu T, Wang R. Dosimetric research on intensity-modulated arc radiotherapy planning for left breast cancer after breast-preservation surgery. *Med Dosim* 2012; **37**: 287-292 [PMID: 22284640 DOI: 10.1016/j.meddos.2011.11.001]
25 **Ginot A**, Doyen J, Hannoun-Lévi JM, Courdi A. [Normal tissue tolerance to external beam radiation therapy: skin]. *Cancer Radiother* 2010; **14**: 379-385 [PMID: 20594894 DOI: 10.1016/j.canrad.2010.03.015]
26 **Hopewell JW**. The skin: its structure and response to ionizing radiation. *Int J Radiat Biol* 1990; **57**: 751-773 [PMID: 1969905 DOI: 10.1080/09553009014550911]
27 **Gokula K**, Earnest A, Wong LC. Meta-analysis of incidence of early lung toxicity in 3-dimensional conformal irradiation of breast carcinomas. *Radiat Oncol* 2013; **8**: 268 [PMID: 24229418 DOI: 10.1186/1748-717X-8-268]
28 **Darby SC**, Ewertz M, McGale P, Bennet AM, Blom-Goldman U, Brønnum D, Correa C, Cutter D, Gagliardi G, Gigante B, Jensen MB, Nisbet A, Peto R, Rahimi K, Taylor C, Hall P. Risk of ischemic heart disease in women after radiotherapy for breast cancer. *N Engl J Med* 2013; **368**: 987-998 [PMID: 23484825 DOI: 10.1056/NEJMoa1209825]
29 **Boice JD**, Harvey EB, Blettner M, Stovall M, Flannery JT. Cancer in the contralateral breast after radiotherapy for breast cancer. *N Engl J Med* 1992; **326**: 781-785 [PMID: 1538720 DOI: 10.1056/NEJM199203193261201]
30 **Kirova YM**, Gambotti L, De Rycke Y, Vilcoq JR, Asselain B, Fourquet A. Risk of second malignancies after adjuvant radiotherapy for breast cancer: a large-scale, single-institution review. *Int J Radiat Oncol Biol Phys* 2007; **68**: 359-363 [PMID: 17379448 DOI: 10.1016/j.ijrobp.2006.12.011]
31 **Clarke M**, Collins R, Darby S, Davies C, Elphinstone P, Evans V, Godwin J, Gray R, Hicks C, James S, MacKinnon E, McGale P, McHugh T, Peto R, Taylor C, Wang Y. Effects of radiotherapy and of differences in the extent of surgery for early breast cancer on local recurrence and 15-year survival: an overview of the randomised trials. *Lancet* 2005; **366**: 2087-2106 [PMID: 16360786 DOI: 10.1016/S0140-6736(05)67887-7]
32 **Stovall M**, Smith SA, Langholz BM, Boice JD, Shore RE, Andersson M, Buchholz TA, Capanu M, Bernstein L, Lynch CF, Malone KE, Anton-Culver H, Haile RW, Rosenstein BS, Reiner AS, Thomas DC, Bernstein JL. Dose to the contralateral breast from radiotherapy and risk of second primary breast cancer in the WECARE study. *Int J Radiat Oncol Biol Phys* 2008; **72**: 1021-1030 [PMID: 18556141 DOI: 10.1016/j.ijrobp.2008.02.040]
33 **Tsai PF**, Lin SM, Lee SH, Yeh CY, Huang YT, Lee CC, Hong JH. The feasibility study of using multiple partial volumetric-modulated arcs therapy in early stage left-sided breast cancer patients. *J Appl Clin Med Phys* 2012; **13**: 3806 [PMID: 22955645 DOI: 10.1120/jacmp.v13i5.3806]

P- Reviewer: Sonoda K, Tsikouras PPT **S- Editor**: Gong XM
L- Editor: A **E- Editor**: Zhang FF

World Journal of Radiology

Submit a Manuscript: http://www.wjgnet.com/esps/
Help Desk: http://www.wjgnet.com/esps/helpdesk.aspx
DOI: 10.4329/wjr.v8.i8.743

World J Radiol 2016 August 28; 8(8): 743-749
ISSN 1949-8470 (online)

ORIGINAL ARTICLE

Retrospective Study

Tumor characteristics of ductal carcinoma *in situ* of breast visualized on [F-18] fluorodeoxyglucose-positron emission tomography/computed tomography: Results from a retrospective study

Tomoyuki Fujioka, Kazunori Kubota, Akira Toriihara, Youichi Machida, Kaori Okazawa, Tsuyoshi Nakagawa, Yukihisa Saida, Ukihide Tateishi

Tomoyuki Fujioka, Kazunori Kubota, Akira Toriihara, Kaori Okazawa, Yukihisa Saida, Ukihide Tateishi, Department of Diagnostic Radiology, Tokyo Medical and Dental University, Tokyo 113-8519, Japan

Youichi Machida, Department of Radiology, Kameda Kyobashi Clinic, Tokyo 104-0031, Japan

Tsuyoshi Nakagawa, Department of Breast Surgery, Tokyo Medical and Dental University, Tokyo 113-8519, Japan

Author contributions: Fujioka T, Kubota K, Toriihara A, Machida Y, Okazawa K, Nakagawa T, Saida Y and Tateishi U designed the research study.

Institutional review board statement: This study was reviewed and approved by the Ethics Committee of the Tokyo Medical and Dental University Hospital.

Informed consent statement: Patients were not required to give informed consent to the study because the analysis used anonymous clinical data that were obtained after each patient agreed to treatment by written consent.

Conflict-of-interest statement: We have no financial relationships to disclose.

Data sharing statement: No additional data are available.

Manuscript source: Invited manuscript

Correspondence to: Ukihide Tateishi, MD, Department of Diagnostic Radiology, Tokyo Medical and Dental University, 1-5-45 Yushima, Bunkyo-ku, Tokyo 113-8519, Japan. utateish@yokohama-cu.ac.jp
Telephone: +81-3-58035311
Fax: +81-3-58030147

Received: January 25, 2016
Peer-review started: January 25, 2016
First decision: February 29, 2016
Revised: May 2, 2016
Accepted: May 31, 2016
Article in press: June 2, 2016
Published online: August 28, 2016

Abstract

AIM

To clarify clinicopathological features of ductal carcinoma *in situ* (DCIS) visualized on [F-18] fluorodeoxyglucose-positron emission tomography/computed tomography (FDG-PET/CT).

METHODS

This study retrospectively reviewed 52 consecutive tumors in 50 patients with pathologically proven pure DCIS who underwent [F-18] FDG-PET/CT before surgery. [F-18] FDG-PET/CT was performed after biopsy in all patients. The mean interval from biopsy to [F-18] FDG-PET/CT was 29.2 d. [F-18] FDG uptake by visual analysis and maximum standardized uptake value (SUVmax) was compared with clinicopathological characteristics.

RESULTS

[F-18] FDG uptake was visualized in 28 lesions (53.8%) and the mean and standard deviation of SUVmax was 1.63 and 0.90. On univariate analysis, visual analysis and the SUVmax were associated with symptomatic presentation (P = 0.012 and 0.002, respectively), palpability (P = 0.030 and 0.024, respectively), use of core-needle biopsy (CNB) (P = 0.023 and 0.012, respectively), ultrasound-guided biopsy (P = 0.040 and 0.006, respectively), enhancing lesion ⩾ 20 mm on magnetic resonance imaging (MRI) (P = 0.001 and 0.010, respectively), tumor size ⩾ 20 mm on histopathology (P = 0.002 and 0.008, respectively). However, [F-18] FDG uptake parameters were not significantly associated with age, presence of calcification on mammography, mass formation on MRI, presence of comedo necrosis, hormone status (estrogen receptor, progesterone receptor and human epidermal growth factor receptor-2), and nuclear grade. The factors significantly associated with visual analysis and SUVmax were symptomatic presentation (P = 0.019 and 0.001, respectively), use of CNB (P = 0.001 and 0.031, respectively), and enhancing lesion ⩾ 20 mm on MRI (P = 0.001 and 0.049, respectively) on multivariate analysis.

CONCLUSION

Although DCIS of breast is generally non-avid tumor, symptomatic and large tumors (⩾ 20 mm) tend to be visualized on [F-18] FDG-PET/CT.

Key words: Ductal carcinoma *in situ*; Positron emission tomography; Breast cancer; [F-18] fluorodeoxyglucose-positron emission tomography/computed tomography

Core tip: Symptomatic tumor or large ductal carcinoma *in situ* (DCIS) (⩾ 20 mm) is often visualized on [F-18] fluorodeoxyglucose-positron emission tomography/computed tomography (FDG-PET/CT). This evidence suggests that large DCIS (⩾ 20 mm) has possibility to be selected as target lesion on [F-18] FDG-PET/CT prior to neoadjuvant chemotherapy.

Fujioka T, Kubota K, Toriihara A, Machida Y, Okazawa K, Nakagawa T, Saida Y, Tateishi U. Tumor characteristics of ductal carcinoma *in situ* of breast visualized on [F-18] fluorodeoxyglucose-positron emission tomography/computed tomography: Results from a retrospective study. *World J Radiol* 2016; 8(8): 743-749 Available from: URL: http://www.wjgnet.com/1949-8470/full/v8/i8/743.htm DOI: http://dx.doi.org/10.4329/wjr.v8.i8.743

INTRODUCTION

Since widespread of and technical improvements to screening mammography, the frequency of ductal carcinoma *in situ* (DCIS) has increased substantially. mammography is able to detect even small DCIS if they have suspicious microcalcifications[1]. With the increasing use of ultrasound and magnetic resonance imaging (MRI), occult DCIS that cannot be identified by mammography, such as DCIS without microcalcification and in patients with dense breasts, have been occasionally detected[2-5]. Nowadays, maximally 20%-25% of new breast cancer cases consist of DCIS[6-8].

[F-18] fluorodeoxyglucose-positron emission tomography/computed tomography (FDG-PET/CT) has been recognized as an essential modality for detecting hypermetabolic activity in primary breast tumor, diagnosing and staging local and distant sites, and evaluating the response to therapy[9-13]. It has been reported that the 25%-77% sensitivity of DCIS is lower than that of invasive ductal carcinoma (IDC) on [F-18] FDG-PET/CT[10,11]. However, DCIS often can be detected on [F-18] FDG-PET/CT. The purpose of this study was to clarify clinicopathological features of DCIS visualized on [F-18] FDG-PET/CT with special reference to pathologic specimens obtained by surgery.

MATERIALS AND METHODS

Patients

This retrospective study was officially approved by the Ethical Commission of our institution (No. 1987). The inclusion criteria for patients with breast cancer were as follows: (1) those who underwent [F-18] FDG-PET/CT and operation at our hospital between March 2008 and May 2014; and (2) those with a pathologically proven pure DCIS, which means DCIS without microinvasion. The decision to perform [F-18] FDG-PET/CT was left to the discretion of the surgeon. In this study, after searching the database of radiology reports and clinical records at our institute, we identified 52 consecutive lesions in 50 patients with a mean age of 56.3 years (range, 33-85 years). All of the patients were not pregnant or breastfeeding. [F-18] FDG-PET/CT was performed after biopsy in all patients. The mean interval from biopsy to [F-18] FDG-PET/CT was 29.2 d (range, 43-133 d) and from biopsy to operation was 78.8 d (range, 34-224 d). The treatment comprised of total mastectomy in 14 lesions, breast conserving surgery in 27, and skin sparing mastectomy in 11.

Clinical examination

All patients had physical examinations, mammography, ultrasound, and MRI. Mammography examination (craniocaudal and mediolateral oblique views) was performed using Lorad Selenia (Hologic Inc, Bedford, Massachusetts). EUB-7500 scanner with a EUP-L54MA 9.75-MHz linear probe (Hitachi Medical Systems, Tokyo) or Aplio XG scanner with a PLT-805AT 8.0-MHz linear probe (Toshiba Medical Systems, Tochigi) was used for the ultrasound examinations.

MRI examination was performed with 1.5-T system

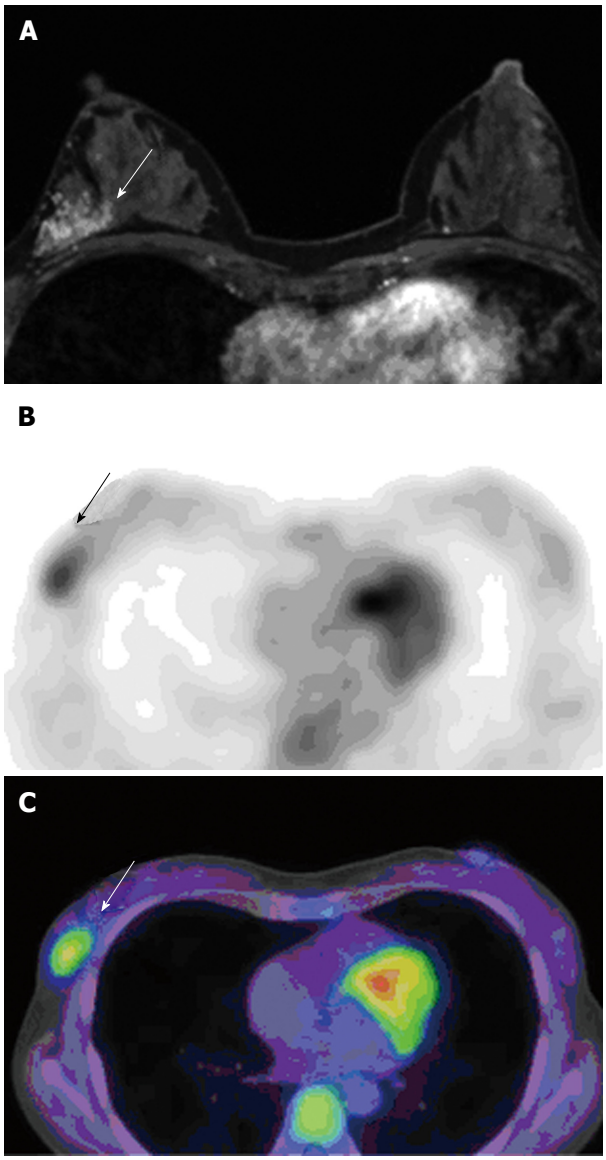

Figure 1 A 41-year-old woman with a palpable mass in right breast was diagnosed with ductal carcinoma *in situ* using ultrasound guided core-needle biopsy. MRI shows a 30-mm enhanced mass in the right breast (A, arrow). [F-18] FDG PET/CT also shows a mass with intense [F-18] FDG uptake (B and C, arrow). On histopathologic examination, a 32-mm DCIS (absence of comedo necrosis, ER positive, PgR positive, HER-2 positive, nuclear grade1) was found. MRI: Magnetic resonance imaging; FDG PET/CT: Fluorodeoxyglucose-positron emission tomography/computed tomography; DCIS: Ductal carcinoma *in situ*; ER: Estrogen receptor; PgR: Progesterone receptor; HER: Human epidermal growth factor receptor.

(Magnetom Vision, Siemens, Erlangen) for 7 patients and 3.0-T system (Signa HDxt, General Electric Medical Systems, Milwaukee, Wisconsin) for 43 patients using a breast coil in the prone position using a breast coil. To evaluate the MRI imaging, the early phase of a contrast enhancement study within 1 and 2 min after intravenous bolus injection of Gd-DTPA (0.2 mL/kg) was acquired. Unilateral coronal T1 weighted sequence [repetition time (TR)/echo time (TE) = 170/4.7, flip angle = 40°, 4 mm thick section, 256 × 256 matrix, 210 mm field of view)] using 1.5-T system and bilateral axial fat suppressed T1 weighted sequence (TR/TE = 6.5/2.4, flip angle = 10°, 2 mm thick section, 512 × 512 matrix, 360 mm field of view) using 3.0-T system were employed.

Percutaneous needle biopsy was done with either ultrasound-guided core-needle biopsy (CNB); 14-gauge Biopsy System (C.R. Bard, Covington, Georgia), ultrasound-guided or stereotactic vacuum-assisted biopsy (VAB); 8- or 11-gauge Mammotome (Ethicon Endo-Surgery, Cincinnati, Ohio) or 11- or 14-gauge Vacora (CR Bard, Murray Hill, New Jersey).

One radiologist had 5 years of experience in breast imaging recorded the reason for presentation (screening-detected or symptomatic lesion), presence of a palpable lesion, use of biopsy device, and image guidance, then evaluated presence of clustered micro calcifications within the tumor on mammography, presence of mass formation, and size (largest diameter) of enhancing lesion on MRI by the American College of Radiology Breast Imaging Reporting and Data System without access to FDG-PET/CT or pathological data[14] (Figure 1A and 2A).

FDG-PET/CT protocol

After at least a 4-h fasting period, the patients received an intravenous injection of 3.7 MBq/kg (0.1 mCi/kg) [F-18] FDG. Images were obtained by whole-body mode with a PET/CT system (Aquiduo; Toshiba Medical Systems, Tokyo). CT images were performed by the following parameters: Pitch 0.938; 0.5 s gantry rotation time; 30 mm/s table time; 120 KVp; auto-exposure control (SD 20); and 2.0-mm slice thickness. Contrast agents were not used during our study. Approximately 60 min after the FDG injection, whole-body emission PET scan was obtained with the following parameters: 7-8 bed positions; 2-min emission time per bed position; 3.375-mm slice thickness; and 128 × 128 matrix.

Data analysis of FDG-PET/CT

[F-18] FDG-PET/CT images were reviewed by two nuclear medicine physicians (with 5 and 17 years of experience) in consensus; although they knew that the patients had DCIS, they were blind to clinical information including menopausal status and phase of the menstrual cycles, and presence of fibrocystic changes in patients. They performed visual analysis without defining a cutoff point. Lesions showing [F-18] FDG uptake higher than the surrounding background of normal breast tissue were defined as FDG positive. Region of interest (ROI) was placed on the PET images for measuring the maximum standardized uptake values (SUVmax) of the tumor. If the tumor was FDG negative, ROI was drawn on the background breast tissue area, and the SUVmax was established (Figures 1B, 1C, 2B and 2C).

Pathological evaluation

Specimens were cut into 5-10 mm contiguous sections and then stained using hematoxylin and eosin staining. Additional immunohistochemistry of markers for estrogen receptor (ER), progesterone receptor (PgR), and human epidermal growth factor receptor (HER)-2 was used to

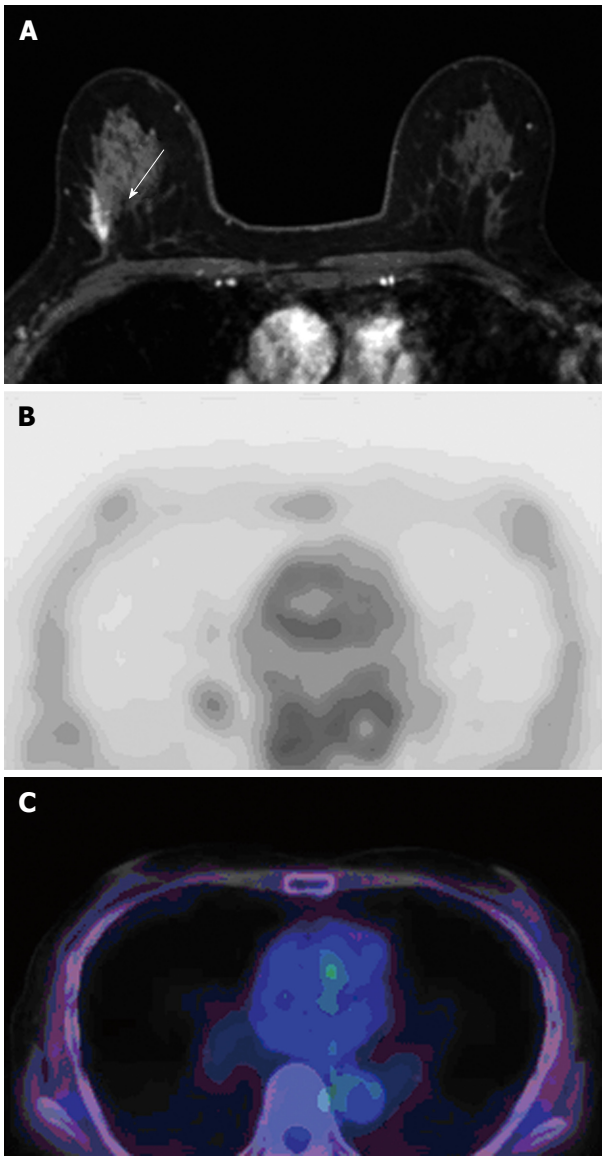

Figure 2 A 64-year-old woman with mammographically detected microcalcifications in right breast was diagnosed with ductal carcinoma *in situ* using stereotactic stereotactic vacuum-assisted biopsy. MRI shows a 12-mm non mass enhancement in the right breast (A, arrow). [F-18] FDG PET/CT did not depict any abnormal uptake (B and C). On histopathologic examination, a 15-mm DCIS (absence of comedo necrosis, ER positive, PgR positive, HER-2 positive, nuclear grade1 DCIS) was found. MRI: Magnetic resonance imaging; FDG PET/CT: Fluorodeoxyglucose-positron emission tomography/computed tomography; DCIS: Ductal carcinoma *in situ*; ER: Estrogen receptor; PgR: Progesterone receptor; HER: Human epidermal growth factor receptor.

evaluate the hormone receptor status. All cases were diagnosed by more than two pathologists, and the following histological features were recorded: Presence of comedo necrosis, nuclear grade (1, 2 or 3), hormone receptor status (ER, PgR and HER-2), and tumor size (largest diameter).

Statistical analysis

The patient population showed normal distribution with the Smirnov-Kolmogorov analysis in this study. The patient characteristics and findings of [F-18] FDG-PET/CT (results of visual analysis and the SUVmax) were compared in each group using univariate analysis of Fisher's exact test and Mann-Whitney *U* test. Further, we also performed multiple logistic regression analyses. Statistical calculations were performed with IBM SPSS statistics 22. *P* values of < 0.05 were regarded as significant.

RESULTS

PET/CT findings

Visual analysis revealed that [F-18] FDG uptake was seen in 28 lesions (53.8%, Figure 1). All values are provided as mean ± SD. The SUVmax of all lesions was 1.63 ± 0.90 (range, 0.62-5.49), of [F-18] FDG-positive lesions were 2.18 ± 1.16 (range, 1.16-5.49), and of [F-18] FDG-negative lesions were 0.99 ± 0.19 (range, 0.62-1.29, Figure 2).

Clinicopathological characteristics

Clinically, 39 lesions (75.0%) were symptomatic, 13 (25.0%) were detected on screening, and 15 (28.8%) were palpable (Table 1). Percutaneous biopsy was performed using ultrasound-guided CNB in 20 lesions (38.5%), ultrasound-guided VAB in 25 (48.1%), and stereotactic VAB in 7 (13.5%). Moreover, calcification on mammography was found in 27 lesions (52.0%). Eight patients (15.4%) had mass formation; 42 lesions (80.8%) did not have mass formation and 2 (3.8%) were undetected at MRI. The mean size of enhancing lesions at MRI was 31.7 ± 30.0 mm (range, 0-80 mm), of [F-18] FDG-negative lesions was 22.8 ± 18.5 mm (range, 0-60 mm), and of [F-18] FDG-positive lesions was 39.3 ± 18.2 mm (range, 7-80 mm). In 34 lesions (65.4%), sizes of enhancing lesions were $\geqslant$ 20 mm.

Microscopic observation revealed that 22 lesions (42.3%) had comedo necrosis, 42 (80.8%) were ER positive, 38 (73.1%) were PgR positive, and 22 (42.3%) were HER-2 positive. Further, 42 lesions (80.8%) were nuclear grade 1, 8 (15.4%) were nuclear grade 2, and 2 (3.8%) were nuclear grade 3. The mean pathological size of tumors was 41.4 ± 32.2 mm (range, 1-150 mm), of [F-18] FDG-negative lesions was 34.5 ± 39.4 mm (range, 1-150 mm), and of [F-18] FDG-positive lesions was 47.3 ± 24.0 mm (range, 2-85 mm); 37 lesions (71.1%) were $\geqslant$ 20 mm in size.

Comparison between clinicopathological characteristics and PET/CT findings

On univariate analysis (Table 2), visual analysis and significant association was found between the SUVmax and symptomatic presentation ($P = 0.012$ and 0.002, respectively), palpability ($P = 0.030$ and 0.024, respectively), use of CNB ($P = 0.023$ and 0.012, respectively), ultrasound-guided biopsy ($P = 0.040$ and 0.006, respectively), large size ($\geqslant$ 20 mm) of enhancing lesion on MRI ($P = 0.001$ and 0.010, respectively), and large tumor size ($\geqslant$ 20 mm) on histopathology ($P = 0.002$

Table 1 Patients' clinicopathological characteristics

Clinical characteristics		*n*	Pathological characteristics		*n*
Symptomatic presentation	Y/N	13/39	Comedo necrosis	Y/N	22/30
Palpability	Y/N	15/37	ER	Y/N	42/10
Biopsy device	CNB/VAB	20/32	PgR	Y/N	38/14
Image guidance	US/ST	45/7	HER2	Y/N	22/30
Calcification at MG	Y/N	27/25	Nuclear grade	1/2/3	42/82
Mass formation at MRI	Mass	8	Tumor size at pathology	Mean ± SD, range	41.4 ± 32.3, 1-150
	Non mass	42		< 20 mm	15
	Undetectable	2		⩾ 20 mm	37
Lesion size at MRI	Mean ± SD, range	31.7 ± 20.0, 0-80.0			
	< 20 mm	18			
	⩾ 20 mm	34			

MG: Mammography; MRI: Magnetic resonance imaging; CNB: Core-needle biopsy; VAB: Vacuum-assisted biopsy; US: Ultrasonographic; ST: Stereotactic; ER: Estrogen receptor; PgR: Progesterone receptor; HER: Human epidermal growth factor receptor.

Table 2 Comparison between patients' clinicopathological characteristics and positron emission tomography/computed tomography findings

		FDG uptake					SUVmax		
		Negative	Positive	Percent	P^1	P^2	mean ± SD	P^3	P^4
Age (yr)	< 55	10	13	56.5%	0.785	0.373	1.88 ± 1.09	0.077	0.210
	⩾ 55	14	15	51.7%			1.44 ± 0.66		
Symptomatic presentation	Y	2	11	84.6%	0.012	0.019	2.36 ± 1.24	0.002	0.001
	N	22	17	43.6%			1.39 ± 0.59		
Palpability	Y	3	12	80.0%	0.030	0.083	1.99 ± 0.87	0.024	0.853
	N	21	16	43.2%			1.49 ± 0.87		
Biopsy device	CNB	5	15	75.0%	0.023	0.001	1.86 ± 0.68	0.012	0.031
	VAB	19	13	40.6%			1.49 ± 0.99		
Image guidance	US	18	27	60.0%	0.040	0.545	1.73 ± 0.92	0.006	0.849
	ST	6	1	14.3%			0.99 ± 0.20		
Calcification at MG	Y	15	12	44.4%	0.177	0.323	1.44 ± 0.66	0.107	0.214
	N	9	16	64.0%			1.84 ± 1.07		
Mass formation at MRI	Y	3	5	62.5%	0.711	0.215	1.76 ± 0.72	0.348	0.253
	N	21	23	52.3%			1.61 ± 0.93		
Lesion size at MRI (mm)	< 20	14	4	22.2%	0.001	0.001	1.24 ± 0.57	0.010	0.049
	⩾ 20	10	24	70.6%			1.84 ± 0.97		
Comedo necrosis	Y	9	13	59.1%	0.581	0.284	1.69 ± 0.85	0.634	0.301
	N	15	15	50.0%			1.59 ± 0.94		
ER	Y	19	23	54.8%	1	0.249	1.67 ± 0.96	0.889	0.628
	N	5	5	50.0%			1.47 ± 056		
PgR	Y	18	20	52.6%	1	0.608	1.64 ± 0.96	0.804	0.731
	N	6	8	57.1%			1.60 ± 0.72		
HER2	Y	10	12	54.5%	1	0.681	1.65 ± 0.78	0.788	0.496
	N	14	16	53.3%			1.62 ± 0.98		
Nuclear grade	1	20	22	52.4%	0.736	0.510	1.64 ± 0.93	0.898	0.718
	2.3	4	6	60.0%			1.61 ± 0.79		
Tumor size at pathology	< 20	12	3	20.0%	0.002	0.708	1.19 ± 0.55	0.008	0.516
	⩾ 20	12	25	67.6%			1.81 ± 0.97		

[1]Fisher's exact test; [2]Logistic regression analysis; [3]Mann-Whitney's *U* test; [4]Multiple regression analysis. FDG: Fluorodeoxyglucose; SUVmax: Maximum standardized uptake value; MG: Mammography; MRI: Magnetic resonance imaging; CNB: Core-needle biopsy; VAB: Vacuum-assisted biopsy; US: Ultrasonographic; ST: Stereotactic; ER: Estrogen receptor; PgR: Progesterone receptor; HER: Human epidermal growth factor receptor.

and 0.008, respectively). However, visual analysis and SUVmax failed to show association with age, presence of calcification on mammography, mass formation on MRI, presence of comedo necrosis, hormone receptor status (ER, PgR), HER-2 expression, and nuclear grade.

On multivariate analysis (Table 2), the factors significantly associated with visual analysis and SUVmax were symptomatic presentation (P = 0.019 and 0.001, respectively), use of CNB (P = 0.001 and 0.031, respectively), and large size (⩾ 20 mm) of enhancing lesion on MRI (P = 0.001 and 0.049, respectively).

DISCUSSION

This study demonstrated that symptomatic and large DCIS (⩾ 20 mm) often can be visualized on [F-18] FDG-PET/CT. The results mirrored those of the previous study showing sensitivity of 25%-77%[10,11]. Although [F-18]

FDG uptake depends on cell density in patients with predominant and pure DCIS, the association between [F-18] FDG and clinicopathological features of DCIS has not been fully elucidated. To the best of our knowledge, our study has the largest sample number among studies examining clinicopathological features of DCIS visualized on [F-18] FDG-PET/CT. Our hypothesis is that large DCIS (≥ 20 mm) has possibility to be selected as target lesion on [F-18] FDG-PET/CT prior to neoadjuvant chemotherapy.

In our study, FDG uptake was highly seen in enhancing lesions of ≥ 20 mm in size on MRI (24/34, 70.6%) and in tumors histopathologically measuring ≥ 20 mm on (25/37, 67.6%). These results show that large tumors tend to have [F-18] FDG uptake in DCIS, similar to a previous study that reported that sensitivity of [F-18] FDG-PET and PET/CT is associated to a large tumor size in IDC[10,11].

In this study, FDG uptake was highly detected in symptomatic (11/13, 84.6%) and palpable lesions (12/15, 80.0%); [F-18] FDG-PET/CT findings were markedly associated with symptomatic presentation and palpability. It has been reported that a large tumor tend to be symptomatic and palpable and that most tumors do not become palpable until a size > 10 mm in diameter is reached[10]. These factors may reflect the association between symptomatic presentation, palpability, and [F-18] FDG-PET/CT findings. In contrast, [F-18] FDG uptake was not highly visualized in screening-detected lesions (17/39, 43.6%) and non-palpable lesions (16/37, 43.2%). These results indicate that FDG-PET/CT was not appropriate for the screening of DCIS.

[F-18] FDG-PET/CT findings markedly associated with the use of CNB and ultrasound-guided biopsy in our study. Stereotactic VAB were performed in 7 lesions undetected by ultrasound, and [F-18] FDG uptake was visualized only in 1/7 (14.3%) lesions. It is possible that larger and palpable lesions are more easily detected and effectively performed using ultrasound CNB than stereotactic VAB. These factors may reflect the association between biopsy device, image guidance, and [F-18] FDG-PET/CT findings.

A previous meta-analysis has demonstrated that pooled random-effect risk values of significant predictors for ipsilateral breast tumor recurrence were the presence of symptoms 1.35 (95%CI: 1.12-1.62), presence of comedo necrosis 1.71 (95%CI: 1.36-2.16), high tumor nuclear grade 1.81 (95%CI: 1.53-2.13), and large tumor size 1.63 (95%CI: 1.30-2.06)[15]. Of these factors, [F-18] FDG-PET/CT findings associated with macro factors (presence of symptoms and large tumor size) but not with micro factors (presence of comedo necrosis and high tumor nuclear grade) in this study. Although the detection of [F-18] FDG-PET/CT depends not only on the tumor volume but also on the degree of FDG activity, tumor-to- normal tissue ratio, and respiratory effects, a lesion < 10 mm lesion may not be detected as the resolution of PET/CT imaging is limited[15,16]. These micro factors will not reflect [F-18] FDG uptake for the limitation of resolution of PET/CT imaging. If a more precise examination can be conducted using high-resolution PET/CT system or positron emission mammography with the addition of more cases and longer follow-up, [F-18] FDG uptake can be predictors for ipsilateral breast tumor recurrence in DCIS patients.

Another previous meta-analysis has reported that a random-effects pooled estimate for underestimation in patients with DCIS at needle biopsy was 25.9% (95%CI: 22.5%, 29.5%)[17] and one study has also shown that high SUVmax is a significant predictive factor for underestimation of IDC in patients with DCIS on needle biopsy[18]. Thus, we need to consider that DCIS proven by core-needle biopsy and with SUVmax will have invasive lesions.

We presented clinicopathological features of DCIS visualized on [F-18] FDG-PET/CT with the largest sample number and hypothesized that large DCIS (≥ 20 mm) might be selected as target lesion on [F-18] FDG-PET/CT prior to neoadjuvant chemotherapy. However, this study had several limitations. First, our study was conducted retrospectively. Second, our study could not correlate the findings with menopausal status and phase of the menstrual cycles, and presence of fibrocystic changes in patients, which can influence normal breast parenchymal enhancement at MRI and [F-18] FDG uptake on PET/CT[19,20]. Third, invasive intervention might affect [F-18] FDG uptake of the lesion in our study, because all patients had biopsy prior to [F-18] FDG-PET/CT study and the mean interval from biopsy to [F-18] FDG-PET/CT was 29.2 d (range, 43-133 d). And finally, PET/CT has limitation in DCIS less than 20 mm; however, MRI might be more sensitive in lesion less than 20 mm.

In conclusion, although most DCIS are non-avid on [F-18] FDG-PET/CT, [F-18] FDG uptake of symptomatic tumors or tumors greater than or equal to 20 mm often can be visualized.

COMMENTS

Background

Nowadays, the incidence of ductal carcinoma *in situ* (DCIS) has increased by prevailing mammography, ultrasound, and magnetic resonance imaging and over 20% of newly identified breast cancer consists of DCIS. However, the sensitivity of [F-18] fluorodeoxyglucose-positron emission tomography/computed tomography (FDG PET/CT) for DCIS remains obscure.

Research frontiers

[F-18] FDG PET/CT has been an essential modality for detecting metabolic activity in primary breast tumor, diagnosing and staging local and distant sites, and evaluating the response to therapy. Wide range of the sensitivity to detect primary tumor in patients with DCIS exists.

Innovations and breakthroughs

DCIS often can be detected on [F-18] FDG-PET/CT in daily practice. The authors assessed clinicopathological features of tumor visualized on [F-18] FDG-PET/CT using pathologic specimens obtained by surgery.

Applications

This study revealed that symptomatic tumor and large DCIS (≥ 20 mm) is often visualized on [F-18] FDG-PET/CT. The results suggest that large DCIS (≥ 20 mm) has possibility to be selected as target lesion on [F-18] FDG-PET/CT prior to neoadjuvant chemotherapy. Devulking after neoadjuvant chemotherapy may affect surgical approach.

Terminology

DCIS is a group of non-invasive malignant epithelial tumors characterized by non-invasion of adjacent tissues and mostly adenocarcinoma derived from the mammary parenchymal epithelium. [F-18] FDG-PET/CT is one of the hybrid type imaging modality which provides activity of glucose metabolism.

Peer-review

This article mentioned that DCIS of breast with diameter > 20 mm can be visualized on [F-18] FDG-PET/ CT. This result is very useful in clinical diagnosis.

REFERENCES

1 **Barreau B**, de Mascarel I, Feuga C, MacGrogan G, Dilhuydy MH, Picot V, Dilhuydy JM, de Lara CT, Bussières E, Schreer I. Mammography of ductal carcinoma in situ of the breast: review of 909 cases with radiographic-pathologic correlations. *Eur J Radiol* 2005; **54**: 55-61 [PMID: 15797293 DOI: 10.1016/j.ejrad.2004.11.019]

2 **Berg WA**, Gutierrez L, NessAiver MS, Carter WB, Bhargavan M, Lewis RS, Ioffe OB. Diagnostic accuracy of mammography, clinical examination, US, and MR imaging in preoperative assessment of breast cancer. *Radiology* 2004; **233**: 830-849 [PMID: 15486214 DOI: 10.1148/radiol.2333031484]

3 **Schouten van der Velden AP**, Schlooz-Vries MS, Boetes C, Wobbes T. Magnetic resonance imaging of ductal carcinoma in situ: what is its clinical application? A review. *Am J Surg* 2009; **198**: 262-269 [PMID: 19375068 DOI: 10.1016/j.amjsurg.2009.01.010]

4 **Baur A**, Bahrs SD, Speck S, Wietek BM, Krämer B, Vogel U, Claussen CD, Siegmann-Luz KC. Breast MRI of pure ductal carcinoma in situ: sensitivity of diagnosis and influence of lesion characteristics. *Eur J Radiol* 2013; **82**: 1731-1737 [PMID: 23743052 DOI: 10.1016/j.ejrad.2013.05.002]

5 **Jin ZQ**, Lin MY, Hao WQ, Jiang HT, Zhang L, Hu WH, Zhang M. Diagnostic evaluation of ductal carcinoma in situ of the breast: ultrasonographic, mammographic and histopathologic correlations. *Ultrasound Med Biol* 2015; **41**: 47-55 [PMID: 25479813 DOI: 10.1016/j.ultrasmedbio.2014.09.023]

6 **Jemal A**, Siegel R, Ward E, Murray T, Xu J, Thun MJ. Cancer statistics, 2007. *CA Cancer J Clin* 2007; **57**: 43-66 [PMID: 17237035 DOI: 10.3322/canjclin.57.1.43]

7 **Li CI**, Daling JR, Malone KE. Age-specific incidence rates of in situ breast carcinomas by histologic type, 1980 to 2001. *Cancer Epidemiol Biomarkers Prev* 2005; **14**: 1008-1011 [PMID: 15824180 DOI: 10.1158/1055-9965.EPI-04-0849]

8 **Rosen EL**, Eubank WB, Mankoff DA. FDG PET, PET/CT, and breast cancer imaging. *Radiographics* 2007; **27** Suppl 1: S215-S229 [PMID: 18180228 DOI: 10.1148/rg.27si075517]

9 **Rostom AY**, Powe J, Kandil A, Ezzat A, Bakheet S, el-Khwsky F, el-Hussainy G, Sorbris R, Sjoklint O. Positron emission tomography in breast cancer: a clinicopathological correlation of results. *Br J Radiol* 1999; **72**: 1064-1068 [PMID: 10700822 DOI: 10.1259/bjr.72.863.10700822]

10 **Avril N**, Rosé CA, Schelling M, Dose J, Kuhn W, Bense S, Weber W, Ziegler S, Graeff H, Schwaiger M. Breast imaging with positron emission tomography and fluorine-18 fluorodeoxyglucose: use and limitations. *J Clin Oncol* 2000; **18**: 3495-3502 [PMID: 11032590]

11 **Mavi A**, Urhan M, Yu JQ, Zhuang H, Houseni M, Cermik TF, Thiruvenkatasamy D, Czerniecki B, Schnall M, Alavi A. Dual time point 18F-FDG PET imaging detects breast cancer with high sensitivity and correlates well with histologic subtypes. *J Nucl Med* 2006; **47**: 1440-1446 [PMID: 16954551]

12 **Groheux D**, Giacchetti S, Delord M, Hindié E, Vercellino L, Cuvier C, Toubert ME, Merlet P, Hennequin C, Espié M. 18F-FDG PET/CT in staging patients with locally advanced or inflammatory breast cancer: comparison to conventional staging. *J Nucl Med* 2013; **54**: 5-11 [PMID: 23213197 DOI: 10.2967/jnumed.112.106864]

13 **Wang Y**, Zhang C, Liu J, Huang G. Is 18F-FDG PET accurate to predict neoadjuvant therapy response in breast cancer? A meta-analysis. *Breast Cancer Res Treat* 2012; **131**: 357-369 [PMID: 21960111 DOI: 10.1007/s10549-011-1780-z]

14 **D'Orsi CJ**, Sickles EA, Mendelson EB, Morris EA. Breast Imaging Reporting and Data System: BI-RADS Atlas. 5th ed. American College of Radiology, Reston, 2013

15 **Wang SY**, Shamliyan T, Virnig BA, Kane R. Tumor characteristics as predictors of local recurrence after treatment of ductal carcinoma in situ: a meta-analysis. *Breast Cancer Res Treat* 2011; **127**: 1-14 [PMID: 21327465 DOI: 10.1007/s10549-011-1387-4]

16 **Groheux D**, Espié M, Giacchetti S, Hindié E. Performance of FDG PET/CT in the clinical management of breast cancer. *Radiology* 2013; **266**: 388-405 [PMID: 23220901 DOI: 10.1148/radiol.12110853]

17 **Brennan ME**, Turner RM, Ciatto S, Marinovich ML, French JR, Macaskill P, Houssami N. Ductal carcinoma in situ at core-needle biopsy: meta-analysis of underestimation and predictors of invasive breast cancer. *Radiology* 2011; **260**: 119-128 [PMID: 21493791 DOI: 10.1148/radiol.11102368]

18 **Shigematsu H**, Kadoya T, Masumoto N, Matsuura K, Emi A, Kajitani K, Amioka A, Okada M. Role of FDG-PET/CT in prediction of underestimation of invasive breast cancer in cases of ductal carcinoma in situ diagnosed at needle biopsy. *Clin Breast Cancer* 2014; **14**: 358-364 [PMID: 24962555 DOI: 10.1016/j.clbc.2014.04.006]

19 **Kang SS**, Ko EY, Han BK, Shin JH, Hahn SY, Ko ES. Background parenchymal enhancement on breast MRI: influence of menstrual cycle and breast composition. *J Magn Reson Imaging* 2014; **39**: 526-534 [PMID: 23633296 DOI: 10.1002/jmri.24185]

20 **Vranjesevic D**, Schiepers C, Silverman DH, Quon A, Villalpando J, Dahlbom M, Phelps ME, Czernin J. Relationship between 18F-FDG uptake and breast density in women with normal breast tissue. *J Nucl Med* 2003; **44**: 1238-1242 [PMID: 12902413]

P- Reviewer: Chu JP, Tsikouras PPT, Zafrakas M
S- Editor: Gong XM **L- Editor**: A **E- Editor**: Zhang FF

World Journal of Radiology

Submit a Manuscript: http://www.wjgnet.com/esps/
Help Desk: http://www.wjgnet.com/esps/helpdesk.aspx
DOI: 10.4329/wjr.v8.i8.750

World J Radiol 2016 August 28; 8(8): 750-756
ISSN 1949-8470 (online)

ORIGINAL ARTICLE

Observational Study

Relative volume measured with magnetic resonance imaging is an articular collapse predictor in hematological pediatric patients with femoral head osteonecrosis

Davide Ippolito, Alessandro Masetto, Cammillo Talei Franzesi, Pietro A Bonaffini, Alessandra Casiraghi, Sandro Sironi

Davide Ippolito, Alessandro Masetto, Cammillo Talei Franzesi, Pietro A Bonaffini, Alessandra Casiraghi, Sandro Sironi, Department of Diagnostic Radiology, School of Medicine, San Gerardo Hospital, University of Milano-Bicocca, 20900 Monza, Italy

Author contributions: Ippolito D is the guarantor of integrity of entire study; Ippolito D contributed to manuscript final version approval; Ippolito D and Masetto A contributed to study concepts; Ippolito D, Masetto A, Talei Franzesi C contributed to study design; Ippolito D, Masetto A, Talei Franzesi C contributed to data acquisition; Ippolito D, Masetto A, Talei Franzesi C and Bonaffini PA contributed to manuscript preparation; Ippolito D, Masetto A and Bonaffini PA contributed to clinical studies; Ippolito D and Bonaffini PA contributed to manuscript editing; Ippolito D and Sironi S contributed to manuscript definition of intellectual content; Masetto A and Casiraghi A contributed to data analysis and interpretation; Talei Franzesi C and Bonaffini PA contributed to literature research; Casiraghi A made statistical analysis; all authors contributed to manuscript revision and review.

Institutional review board statement: The study was reviewed and approved by the H. San Gerardo Institutional Review Board.

Informed consent statement: Every patient gave his informed consent, as required by our Institution.

Conflict-of-interest statement: All the authors are aware of the content of the manuscript and have no conflict of interest.

Data sharing statement: No additional data are available.

Manuscript source: Invited manuscript

Correspondence to: Davide Ippolito, MD, Department of Diagnostic Radiology, School of Medicine, San Gerardo Hospital, University of Milano-Bicocca, Via Pergolesi 33, 20900 Monza, Italy. davide.atena@tiscalinet.it
Telephone: +39-02-64488265
Fax: +39-02-64488299

Received: January 26, 2016
Peer-review started: January 27, 2016
First decision: March 23, 2016
Revised: April 10, 2016
Accepted: May 31, 2016
Article in press: June 2, 2016
Published online: August 28, 2016

Abstract

AIM

To assess the potential value of femoral head (FH) volume measurements to predict joint collapse, as compared to articular surface involvement, in post-treatment osteonecrosis (ON) in pediatric patients affected by lymphoproliferative diseases.

METHODS

Considering 114 young patients with lymphoproliferative diseases undergone a lower-limbs magnetic resonance imaging (MRI) examination between November 2006 and August 2012 for a suspected post-treatment ON, we finally considered a total of 13 cases (7 males, mean age 15.2 ± 4.8 years), which developed a FH ON lesions (n = 23). The MRI protocol included coronal short tau inversion recovery and T1-weighted sequences, from the hips to the ankles. During the follow-up (elapsed time: 9.2 ± 2 mo), 13/23 FH articular surface (FHS)

developed articular deformity. The first MRI studies with diagnosis of ON were retrospectively analyzed, measuring FH volume (FHV), FHS, ON volume (ONV) and the articular surface involved by ON (ONS). The relative involvement of FHS, in terms of volume [relative volume (RV): ONV/FHV] and articular surface [relative surface (RS): ONS/FHS], was then calculated.

RESULTS

By using receiver operating characteristic curve analysis (threshold of 23% of volume involvement), RV predicted articular deformity in 13/13 FHS [sensitivity 100%, specificity 90%, accuracy 95%, positive predictive value (PPV) 93%, negative predictive value (NPV) 100%]. Considering a threshold of 50% of articular involvement, RS predicted articular deformity in 10/13 femoral heads (sensitivity 77%, specificity 100%, accuracy 87%, PPV 100%, NPV 77%).

CONCLUSION

RV might be a more reliable parameter than RS in predicting FH deformity and could represent a potential complementary diagnostic tool in the follow-up of femoral heads ON lesions.

Key words: Osteonecrosis; Volume; Articular surface; Lymphoproliferative diseases; Femoral head; Magnetic resonance imaging

Core tip: Osteonecrosis can affect different bone segments but the most common sites are the weight-bearing joints of the lower limbs (hips and knees), with potential evolution to disability. To date magnetic resonance imaging represents the standard imaging method in the assessment of bone necrotic lesions [osteonecrosis (ON)], replacing other techniques in diagnostic work-up of initial ON, allowing also the detection of early bone marrow changes. Our preliminary data show that the volume of the necrotic portion of the femoral head might be a parameter highly predictive of future collapse of femoral head affected by osteonecrosis also in young patients treated for haematological malignancies.

Ippolito D, Masetto A, Talei Franzesi C, Bonaffini PA, Casiraghi A, Sironi S. Relative volume measured with magnetic resonance imaging is an articular collapse predictor in hematological pediatric patients with femoral head osteonecrosis. *World J Radiol* 2016; 8(8): 750-756 Available from: URL: http://www.wjgnet.com/1949-8470/full/v8/i8/750.htm DOI: http://dx.doi.org/10.4329/wjr.v8.i8.750

INTRODUCTION

The optimization of treatment strategies for haematological pediatric malignancies has led to a significant improvement of overall survival[1]; however, therapy has also turned out to determine several complications, particularly osteonecrosis (ON)[2]. Several risk factors might play a role in the development of bone tissue necrosis, both individual and related to treatment itself (glucocorticoids, chemotherapics, total body irradiation)[3-6]. ON can affect different bone segments but the most common sites are the weight-bearing joints of the lower limbs (hips and knees), with potential evolution to disability[7]. Therapeutic solutions and clinical management of post-treatment osteonecrosis depends on the joint affected, the stage of both osteonecrosis and primary disease and on symptoms. Core decompression is the most frequently therapeutic procedure in early femoral head ON, while joint replacement is performed in cases of collapse[8]. However, even minimally invasive surgery may be life threatening and septic complications may be severe[9].

Imaging may play a crucial role for prompt diagnosis and proper staging, above all in patients with no specific symptoms[10]. Magnetic resonance imaging (MRI) is the technique that demonstrated the highest sensitivity and specificity in the early diagnosis of ON: It allows detecting initial typical signal intensity alterations of the bone marrow, when other examinations show nonspecific findings or even no alterations at all[11]. Some studies reported that MRI is accurate also for the assessment of the size of femoral head osteonecrotic lesion[12]. This parameter seems to be one of the main determinants of collapse in adults[13,14] but to our knowledge there are only a few studies in young patients.

On these bases, the purpose of our study was to evaluate if the volumetric measurement of post-treatment osteonecrotic lesions on MRI could be a predictor of femoral head collapse also in paediatric patients with haematological malignancies. We also compared volume with articular surfaces of affected femoral heads as an alternative parameter for prediction of collapse.

MATERIALS AND METHODS

Study population

We retrospectively evaluated as a start 114 peadiatric and young patients (64 males, 50 females, mean age 14.8 years, range 3-23 years), affected by proven lymphoproliferative diseases and treated with chemotherapy and steroids and/or bone marrow transplantation. All these patients underwent at least one lower limb MRI study between November 2006 and March 2012 (80/114 because of symptoms suspicious for ON, 34/114 for screening purposes), while follow-up examinations were performed in 72/114 cases.

Among these patients, we selected only those who showed at follow-up osteonecrosis of one or both femoral heads, regardless symptoms and with the following exclusion criteria: (1) patients with suspected osteonecrosis but affected by non-lymphoproliferative

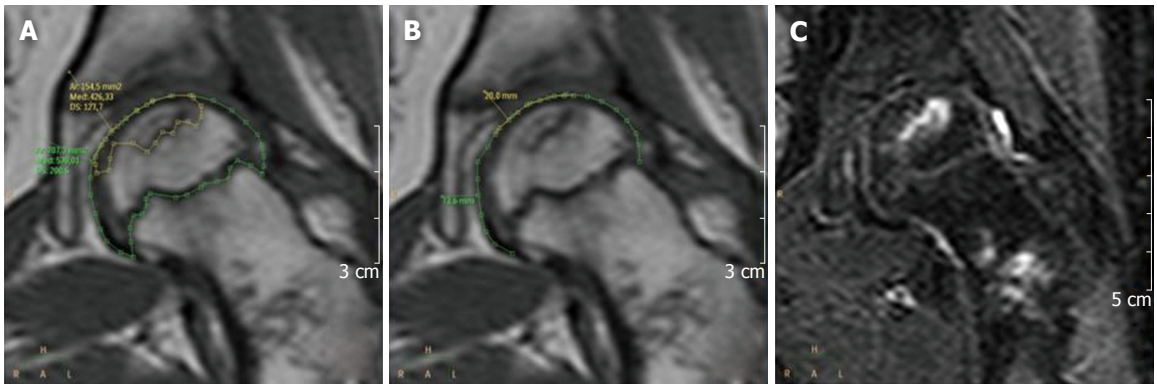

Figure 1 Assessment of relative volume and relative surface. The measurements were performed on a dedicated workstation on the T1-weighted images, both for RV (A) and RS (B) for each slice of the series. The corresponding STIR images (C) were reviewed in order to better evaluate the extent of the necrotic process. RV: Relative volume; RS: Relative surface; STIR: Short time inversion recovery.

diseases (*e.g.*, thrombotic thrombocytopenic purpura) or those who underwent MRI study for different purposes (lymphoproliferative disease localization, inflammatory complications such as fasciitis, osteomyelitis or soft tissues abscess); (2) patients who did not perform follow-up studies in our Institution; (3) patients with osteonecrosis of the femoral head and evidence of joint deformity or collapse at the first MRI examination.

As a result, a total of 13 patients (7 males, 6 females; mean age 15.2 years, range 9-23 years), met the above-mentioned inclusion and exclusion criteria.

MRI study protocol

The MRI studies were performed either on a 1.5 T magnet (Achieva, Philips) using a built-in body coil (Q-Body) and the stepping table technique or a 1 T scanner (Panorama, Philips), with a three-channel surface body coil (extra large body coil). The acquisition protocol included: long echo time (TE) short time inversion recovery (STIR) (TE = 80 ms; repetition time (TR)/TE = 4935/150 ms; slice thickness = 5 mm; acquisition matrix MxP = 352 × 351; acquisition voxel measurement, phase and slice encoding (MPS) = 1.51/1.51/5.00 mm; reconstruction voxel MPS = 1.04/1.04/5.00; min. slice gap = 1 mm) and T1-weighted sequences (TE = 15 ms; TR = 225 ms; acquisition matrix MxP = 400 × 259; acquisition voxel MPS = 1.33/1.33/5.00 mm; reconstruction voxel MPS = 1.04/1.04/5.00; min. slice gap = 5 mm; act. slice gap 0.5 mm). Images were acquired coronal, from the hips to the ankle, with an average acquisition time of about 15-20 min (depending on patient's height).

Image analysis: Femoral head volume and surface

The diagnosis of osteonecrotic involvement of femoral heads was established when typical morphological alterations were present[15]: Sharply defined areas with geographical appearance affecting subchondral bone marrow, characterized by peripheral rim of low signal intensity on T1-weighted sequences and high signal intensity on STIR images.

Considering the first MRI study that showed the presence of osteonecrosis, a radiologist measured on dedicated software (Brilliance Workspace Portal, V 2.6.1.5, Philips): The volume [femoral head volume (FHV)] and the articular surface area of the affected epiphysis [femoral head surface (FHS)], the osteonecrotic lesion volume (ONV) and the articular surface area affected by osteonecrosis (ONS). As shown in Figure 1, to determine the FHV in each slide of the T1 weighted images the corresponding epiphysis was contoured along its edge, using the cartilaginous physeal line as the caudal limit of the epiphysis itself. The procedure was performed for each slice and the values obtained (expressed in square millimeter) were added up together and then multiplied by section thickness (5 mm), obtaining the corresponding epiphyseal volumes (expressed in cubic millimeter). The same steps were followed for the assessment of the ONV, by contouring on T1 images the edge of the bone involved by necrosis. STIR sequence was contextually taken into account as reference to better assess lesion's boundaries. Similarly, to determine the FHS (Figure 1), the convex articular edge was contoured in each slice of the T1 weighted sequence, obtaining linear values (expressed in millimeter) that were added up together; the resulting number was multiplied by the slice thickness (5 mm), obtaining surface values (expressed in square millimeter). The same procedure was performed for the ONS, considering only the surface of the femoral head with subchondral bone necrosis.

Assessment of relative volume and relative surface

Following these measurements, the necrotic portions of the femoral heads involved were then calculated as ratio. First of all, the involvement of the femoral heads in terms of volume was defined as relative volume (RV) and calculated with the following formula: ONV/FHV. The articular surface involvement was defined as relative surface (RS) and assessed with the following formula: ONS/FHS (Table 1).

Statistical analysis

We employed the receiver-operator characteristic (ROC)

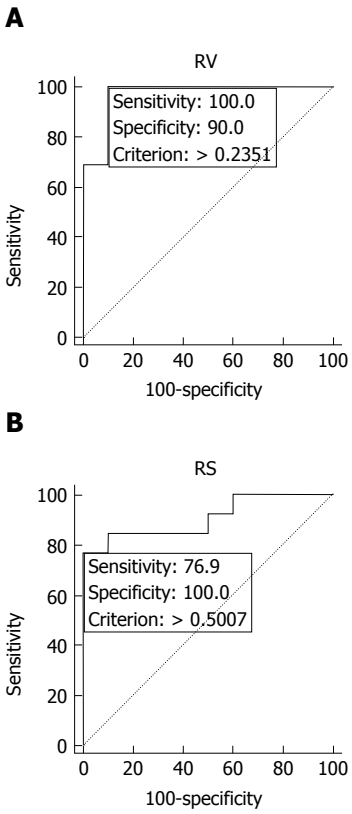

Figure 2 Receiver-operator characteristic curves analysis of relative volume and relative surface. RV (A) performed best with a threshold of 0.23 (sensitivity 100%, specificity 90%), while RS (B) with a threshold of 0.50 (sensitivity 77%, specificity 90%). RV: Relative volume; RS: Relative surface.

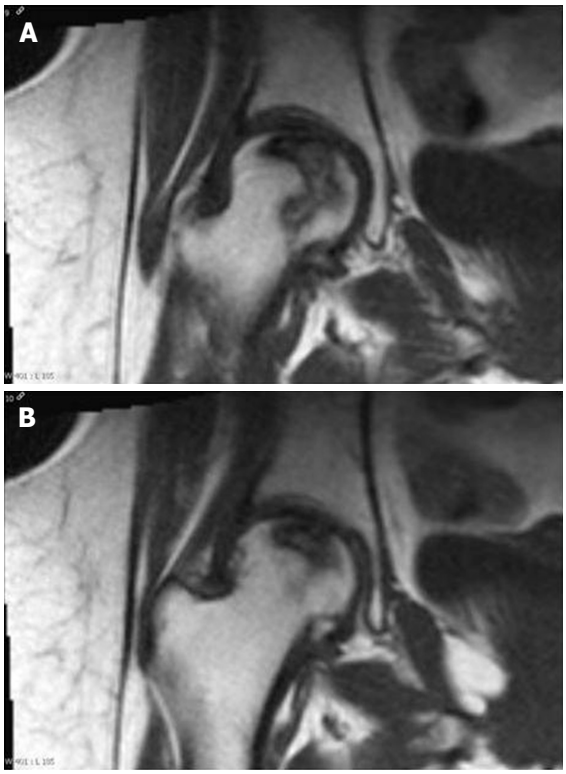

Figure 3 Two adjacent coronal T1-weighted images show the discrepancy between the two parameters (volume, A *vs* surface area, B) considered for the prediction of future joint deformity. Even if the overall necrotic lesion is rather big (A), there is only a minor involvement of the femoral head surface (B): In these cases RV performed better than RS in predicting femoral head deformity. RV: Relative volume; RS: Relative surface.

Table 1 Results of relative volume and relative surface for prediction of femoral head collapse

	RV (ONV/FHV)	RS (ONS/FHS)
Threshold	0.23	0.5
Sensitivity	100%	77%
Specificity	90%	100%
Accuracy	95%	87%
PPV	93%	100%
NPV	100%	77%

RV: Relative volume; RS: Relative surface; ONV: Osteonecrosis volume; FHV: Femoral head volume; ONS: Osteonecrosis surface; FHS: Femoral head surface; PPV: Positive predictive value; NPV: Negative predictive value.

curve analysis in order to determine the best thresholds of both RV and RS to predict joint deformity. Statistical analysis was performed with MedCalc software (version 12.4.0.0).

RESULTS

Twenty-three femoral heads were affected, since 10/13 patients had bilateral involvement. In the follow-up studies (elapsed time: 9.2 ± 2 mo), 13/23 (56%) femoral heads developed articular deformity or complete collapse, within a mean time of 10.2 mo (range 2-32 mo). The average follow-up period of the femoral heads that did not collapse was 12.5 mo (range 4-32 mo). The required time for postprocessing, volumes and surfaces measurements was about 10 min per lesion.

Applying the thresholds suggested by the ROC analysis (0.23), RV predicted correctly articular deformity in 13/13 (100%) of femoral heads affected by ON and erroneously in 1/10 that did not collapse (Figure 2), with sensitivity of 100%, specificity of 90%, accuracy of 95%, positive predictive value (PPV) of 93% and negative predictive value (NPV) of 100% (Table 1).

On the other hand, using a threshold of 0.50 (Figure 2), RS correctly predicted joint collapse in 10/13 (77%) femoral heads, without false positives; however, it missed 3/13 (23%) of them that developed deformity during follow-up, with corresponding sensitivity of 77%, specificity of 100%, accuracy of 87%, PPV of 100% and NPV of 77% (Table 1). In the 3 cases in which RS did not predict joint collapse and was not in agreement with RV, there was discrepancy between the overall size of the osteonecrotic lesion and its involvement of the corresponding articular surface of the femoral head affected (Figure 3).

DISCUSSION

Therapy for hematologic malignancies is a well-recognized cause of osteonecrosis in paediatric patients[16]. Femoral

heads are the most critical sites affected, because of their high rate of progression towards collapse leading to surgical intervention[17]. To determine which patients with femoral head osteonecrosis will more likely develop collapse may be important in order to guide follow-up studies and to better address treatment strategies[10].

The main purpose of our study was to evaluate if the size of both the lesion and the joint surface involved by necrosis could be useful predictors of deformity in young patients affected by post-treatment femoral head ON. To this reason, we retrospectively selected in our database patients who underwent several lower-limbs MRI studies to reveal either stability of the osteonecrotic lesions or development of joint deformity. We measured the volume of the necrotic lesion related to the volume of the proximal epiphyseal region and we also assessed the extension of the lesion itself to the joint surface in relation to the whole articular surface of the femoral head. The two parameters were called RV and RS respectively and were compared each other in terms of prediction of joint collapse. In order to obtain a more reliable quantification of the necrotic lesion, without employing complex mathematical formulas, we measured epiphyseal volume only, considering the physeal line as the caudal limit of the epiphysis itself. In all our patients the physeal line was clearly evident or at least appreciable, particularly evaluating T1 and STIR images side by side, because of incomplete consolidation of the cartilaginous growth plate.

Several authors evaluated potential reliable parameters to predict collapse or outcome of core decompression in adult patients with femoral head osteonecrosis[18-20]. Most of these studies focused on the measurements of the necrotic portion of the femoral head or of the joint surface involved by necrosis. Morphologic evaluations were performed with radiographs in older works and more recently with MRI, employing several different techniques or formulas. Almost all the Authors reported the size of the necrotic lesion as the main predictor of progression towards deformity and collapse of the femoral head[21]. To our knowledge, only one study performed by Karimova *et al*[22] evaluated factors that could potentially forecast the outcome of post-treatment femoral head osteonecrosis in paediatric patients affected by haematological malignancies. Among several parameters (*i.e.*, sex, age, stage disease), the necrotic portion of femoral head was considered. Radiological evaluation of involvement by ON was conducted with two approaches. The first one consisted of a quantitative assessment, according to the measurement technique described by Hernigou[12] and to the classification system of Steinberg *et al*[23] (mild: < 15% of femoral head affected; moderate: 15%-30%; severe: > 30%). The second approach relied on the method described by Sugano *et al*[24], where ON lesions are classified semi-quantitatively (A: Involvement of the medial 1/3 of femoral head or less; B: Medial 2/3 or less; C: More than 2/3). Similarly to the results reported for adults' femoral head osteonecrosis, also in Karimova's work the size of the necrotic lesion turned out to be the best predictor of future collapse. In particular, femoral heads with an involvement of more than 30% by osteonecrosis or type C lesions had higher rates of collapse. The involvement of the articular surface was also included among the potential factors for progression to deformity but it was considered only as a qualitative parameter, without measurements of the joint affected surface.

Even according to our results, RV performed better than RS, with an overall accuracy of 95% *vs* 87% and with a cut-off value of 23%, as reported by the cited papers also in adult patients. Particularly, RS did not properly forecast the progression to collapse in 3/13 cases, where the necrotic process had a minor involvement of the joint surface as compared to the underlying deeper portions of the epiphysis affected. Karimova's results may seem quite similar to our in terms of cut-off value of necrotic lesion volume (30% *vs* 23%, respectively) but the differences between the two approaches should be take into account. We considered only the proximal femoral epiphysis involvement, while in Karimova's study the reported percentage was related to the entire femoral head, including also the physeal and metaphyseal regions. Moreover, also measurements methods are different (semiquantitative evaluation of femoral head involvement *vs* quantitative assessment of proximal epiphysis). Basing on these observations, we presume that in our population collapse occurred with smaller lesions or with minor femoral head involvement than in Karimova's patients.

The main limitations of our study were the small number of patients considered and the short non-standardized follow-up time; however it has to be considered that, according to the literature, our population study was quite in line with those reported in other studies. Inter- and intra-observer agreement analysis might have strengthened the reported results but it was out of the aims of this study. Furthermore, referring to physeal line as caudal limit of femoral epiphysis might be considered a less reproducible method for volume measurements in the clinical practice. Therefore, our data and the proposed technique for volume analysis have to be confirmed and validated by a wider study population. Another remark is that the majority of our patients were still being administered corticosteroids between the different MRI studies, that were either performed during the different phases of the therapy or after treatment for a graft *vs* host disease. As known, therapy itself along with the size of the lesion may determine the progression towards deformity. However, the main purpose of our study was to assess the potential value of volume and surface measurements in the prediction of joint collapse, regardless patients' symptoms and related risk factors (*i.e.*, therapy).

In conclusion, our preliminary data show that the volume of the necrotic portion of the femoral head might be a parameter highly predictive of future collapse of femoral head affected by osteonecrosis also in young patients treated for haematological malignancies. Since the management of osteonecrosis is often challenging,

the quick and reproducible measurements of this parameter could properly guide follow-up studies and, therefore, help better address diagnostic resources, avoiding unnecessary examinations in small lesions or in those less prone to collapse. However, further prospective studies with a larger population study are fundamental to confirm these results.

COMMENTS

Background

The treatment strategies for haematological pediatric malignancies has improved the overall survival, but has also determined several complications, in particular osteonecrosis (ON), related to several risk factors, individual and related to treatment (glucocorticoids, chemotherapics, total body irradiation). The most common sites involved in ON are the weight-bearing joints of the lower limbs (hips and knees), with potential evolution to disability. Imaging may play a crucial role for prompt diagnosis and proper staging, and magnetic resonance imaging (MRI) is the technique that demonstrated the highest sensitivity and specificity in the early diagnosis of ON and in an accurate assessment of the size of osteonecrotic lesion. This parameter seems to be one of the main determinants of collapse in adults, but there are only a few studies in young patients.

Research frontiers

MRI, with the advantages of no ionizing radiation, permits to safely evaluated young patients. Therefore the MRI study may be useful in the evaluation and follow-up of post-treatment femoral head osteonecrosis, in paediatric patients affected by haematological malignancies.

Innovations and breakthroughs

Almost all the authors reported the size of the necrotic lesion as the main predictor of progression towards deformity and collapse of the femoral head in adult patients. The measurement of the volume of the necrotic portion of the femoral head, with MRI, could potentially forecast the outcome of post-treatment femoral head osteonecrosis in paediatric patients affected by haematological malignancies.

Applications

The relevance of this work relies on the possibility, by measuring the volume of the necrotic portion of the femoral head, to obtain a new diagnostic parameter that might be highly predictive of future collapse of femoral head affected by osteonecrosis also in young patients treated for haematological malignancies. Furthermore the quick and reproducible measurements of this parameter could properly guide follow-up studies, improving the better address diagnostic resources and avoiding unnecessary examinations in small lesions or in those less prone to collapse.

Terminology

MRI: MRI is the technique that demonstrated the highest sensitivity and specificity in the early diagnosis of ON; ON: ON is a bone disease, that affect the joints, caused by reduced blood flow. The typical aspect is a "geographic pattern" area, surrounded by low signal intensity serpentine rim and a high signal intensity line on T2 weighted images inside the rim; FHV: Femoral head volume, calculated by contouring in each slide of the T1 weighted images the corresponding epiphysis. The values obtained (expressed in square millimeter) were added up together and then multiplied by section thickness (5 mm), obtaining the corresponding epiphyseal volumes (expressed in cubic millimeter); ONV: Osteonecrotic volume, by contouring for each slide on T1 images, the edge of the bone involved by necrosis. The values obtained (expressed in square millimeter) were added up together and then multiplied by section thickness (5 mm), obtaining the corresponding epiphyseal volumes (expressed in cubic millimeter); FHS: Femoral head surface, assessed by contouring the convex articular edge in each slice of the T1 weighted sequence, obtaining linear values (expressed in millimeter) that were added up together; the resulting number was multiplied by the slice thickness (5 mm), obtaining surface values (expressed in square millimeter); ONS: Osteonecrotic surface, measured with the same procedure of FHS, considering only the surface of the femoral head with subchondral bone necrosis; RV: Relative volume, defines the articular volume involved on ON, calculated with the following formula: ONV/FHV; RS: Relative surface, defines the articular surface involved on ON, assessed with the following formula: ONS/FHS.

Peer-review

This is a technical and interdisciplinary study conducted in the assessment of receiver-operator characteristic. This preliminary data show that the volume of the necrotic portion of the femoral head might be a parameter highly predictive of future collapse of femoral head affected by osteonecrosis also in young patients treated for haematological malignancies.

REFERENCES

1 **Hunger SP**, Lu X, Devidas M, Camitta BM, Gaynon PS, Winick NJ, Reaman GH, Carroll WL. Improved survival for children and adolescents with acute lymphoblastic leukemia between 1990 and 2005: a report from the children's oncology group. *J Clin Oncol* 2012; **30**: 1663-1669 [PMID: 22412151 DOI: 10.1200/JCO.2011.37.8018]

2 **Barr RD**, Sala A. Osteonecrosis in children and adolescents with cancer. *Pediatr Blood Cancer* 2008; **50**: 483-485; discussion 486 [PMID: 18064641 DOI: 10.1002/pbc.21405]

3 **Harper PG**, Trask C, Souhami RL. Avascular necrosis of bone caused by combination chemotherapy without corticosteroids. *Br Med J* (Clin Res Ed) 1984; **288**: 267-268 [PMID: 6198019 DOI: 10.1136/bmj.288.6413.267]

4 **Jagasia S**, Misfeldt A, Griffith M, Jagasia M. Age and total-body irradiation in addition to corticosteroid dose are important risk factors for avascular necrosis of the bone. *Biol Blood Marrow Transplant* 2010; **16**: 1750-1751 [PMID: 20849970 DOI: 10.1016/j.bbmt.2010.09.004]

5 **Kawedia JD**, Kaste SC, Pei D, Panetta JC, Cai X, Cheng C, Neale G, Howard SC, Evans WE, Pui CH, Relling MV. Pharmacokinetic, pharmacodynamic, and pharmacogenetic determinants of osteonecrosis in children with acute lymphoblastic leukemia. *Blood* 2011; **117**: 2340-2347; quiz 2556 [PMID: 21148812 DOI: 10.1182/blood-2010-10-311969]

6 **Niinimäki RA**, Harila-Saari AH, Jartti AE, Seuri RM, Riikonen PV, Pääkkö EL, Möttönen MI, Lanning M. High body mass index increases the risk for osteonecrosis in children with acute lymphoblastic leukemia. *J Clin Oncol* 2007; **25**: 1498-1504 [PMID: 17442991 DOI: 10.1200/JCO.2006.06.2539]

7 **Min BW**, Song KS, Cho CH, Lee SM, Lee KJ. Untreated asymptomatic hips in patients with osteonecrosis of the femoral head. *Clin Orthop Relat Res* 2008; **466**: 1087-1092 [PMID: 18327630 DOI: 10.1007/s11999-008-0191]

8 **Vora A**. Management of osteonecrosis in children and young adults with acute lymphoblastic leukaemia. *Br J Haematol* 2011; **155**: 549-560 [PMID: 22077340 DOI: 10.1111/j.1365-2141.2011.08871.x]

9 **Singer K**, Subbaiah P, Hutchinson R, Odetola F, Shanley TP. Clinical course of sepsis in children with acute leukemia admitted to the pediatric intensive care unit. *Pediatr Crit Care Med* 2011; **12**: 649-654 [PMID: 21478790 DOI: 10.1097/PCC.0b013e31821927f1]

10 **Marchese VG**, Connolly BH, Able C, Booten AR, Bowen P, Porter BM, Rai SN, Hancock ML, Pui CH, Howard S, Neel MD, Kaste SC. Relationships among severity of osteonecrosis, pain, range of motion, and functional mobility in children, adolescents, and young adults with acute lymphoblastic leukemia. *Phys Ther* 2008; **88**: 341-350 [PMID: 18202079 DOI: 10.2522/ptj.20070108]

11 **Mitchell MD**, Kundel HL, Steinberg ME, Kressel HY, Alavi A, Axel L. Avascular necrosis of the hip: comparison of MR, CT, and scintigraphy. *AJR Am J Roentgenol* 1986; **147**: 67-71 [PMID: 3487233 DOI: 10.2214/ajr.147.1.67]

12 **Hernigou P**, Lambotte JC. Volumetric analysis of osteonecrosis of the femur. Anatomical correlation using MRI. *J Bone Joint Surg Br*

2001; **83**: 672-675 [PMID: 11476303 DOI: 10.1302/0301-620X.83B5.11447]
13 **Hernigou P**, Lambotte JC. Bilateral hip osteonecrosis: influence of hip size on outcome. *Ann Rheum Dis* 2000; **59**: 817-821 [PMID: 11005784 DOI: 10.1136/ard.59.10.817]
14 **Koo KH**, Kim R. Quantifying the extent of osteonecrosis of the femoral head. A new method using MRI. *J Bone Joint Surg Br* 1995; **77**: 875-880 [PMID: 7593098]
15 **Kaplan P**, Helms CA, Dussault R, Anderson MW, Major NM. Musculoskeletal MRI. W.B. Saunders, Philadelphia, 2001: 46-48
16 **Mattano LA**, Sather HN, Trigg ME, Nachman JB. Osteonecrosis as a complication of treating acute lymphoblastic leukemia in children: a report from the Children's Cancer Group. *J Clin Oncol* 2000; **18**: 3262-3272 [PMID: 10986059]
17 **Ribeiro RC**, Fletcher BD, Kennedy W, Harrison PL, Neel MD, Kaste SC, Sandlund JT, Rubnitz JE, Razzouk BI, Relling MV, Pui CH. Magnetic resonance imaging detection of avascular necrosis of the bone in children receiving intensive prednisone therapy for acute lymphoblastic leukemia or non-Hodgkin lymphoma. *Leukemia* 2001; **15**: 891-897 [PMID: 11417473 DOI: 10.1038/sj.leu.2402139]
18 **Kerboul M**, Thomine J, Postel M, Merle d'Aubigné R. The conservative surgical treatment of idiopathic aseptic necrosis of the femoral head. *J Bone Joint Surg Br* 1974; **56**: 291-296 [PMID: 4854691]
19 **Ohzono K**, Saito M, Sugano N, Takaoka K, Ono K. The fate of nontraumatic avascular necrosis of the femoral head. A radiologic classification to formulate prognosis. *Clin Orthop Relat Res* 1992; (**227**): 73-78 [PMID: 1555359]
20 **Mont MA**, Jones LC, Pacheco I, Hungerford DS. Radiographic predictors of outcome of core decompression for hips with osteonecrosis stage III. *Clin Orthop Relat Res* 1998; (**354**): 159-168 [PMID: 9755775 DOI: 10.1097/00003086-199809000-00019]
21 **Lee GC**, Steinberg ME. Are we evaluating osteonecrosis adequately? *Int Orthop* 2012; **36**: 2433-2439 [PMID: 23011722 DOI: 10.1007/s00264-012-1658-7]
22 **Karimova EJ**, Rai SN, Howard SC, Neel M, Britton L, Pui CH, Kaste SC. Femoral head osteonecrosis in pediatric and young adult patients with leukemia or lymphoma. *J Clin Oncol* 2007; **25**: 1525-1531 [PMID: 17442995 DOI: 10.1200/JCO.2006.07.9947]
23 **Steinberg ME**, Bands RE, Parry S, Hoffman E, Chan T, Hartman KM. Does lesion size affect the outcome in avascular necrosis? *Clin Orthop Relat Res* 1999; (**367**): 262-271 [PMID: 10546624 DOI: 10.1097/00003086-199910000-00033]
24 **Sugano N**, Ohzono K, Masuhara K, Takaoka K, Ono K. Prognostication of osteonecrosis of the femoral head in patients with systemic lupus erythematosus by magnetic resonance imaging. *Clin Orthop Relat Res* 1994; (**305**): 190-199 [PMID: 8050228 DOI: 10.1097/00003086-199408000-00023]

P- Reviewer: Casciaro S, Gao BL, Li YZ, Shen J
S- Editor: Gong XM **L- Editor**: A **E- Editor**: Zhang FF

World Journal of Radiology

Submit a Manuscript: http://www.wjgnet.com/esps/
Help Desk: http://www.wjgnet.com/esps/helpdesk.aspx
DOI: 10.4329/wjr.v8.i8.757

World J Radiol 2016 August 28; 8(8): 757-763
ISSN 1949-8470 (online)

CASE REPORT

Unusual presentation of Erdheim-Chester disease in a child with acute lymphoblastic leukemia

Archana George Vallonthaiel, Asit Ranjan Mridha, Shivanand Gamanagatti, Manisha Jana, Mehar Chand Sharma, Shah Alam Khan, Sameer Bakhshi

Archana George Vallonthaiel, Asit Ranjan Mridha, Mehar Chand Sharma, Department of Pathology, All India Institute of Medical Sciences, New Delhi 110029, India

Shivanand Gamanagatti, Manisha Jana, Department of Radiodiagnosis, All India Institute of Medical Sciences, New Delhi 110029, India

Shah Alam Khan, Department of Orthopaedics, All India Institute of Medical Sciences, New Delhi 110029, India

Sameer Bakhshi, Medical Oncology, All India Institute of Medical Sciences, New Delhi 110029, India

Author contributions: Vallonthaiel AG, Mridha AR and Sharma MC designed the report; Vallonthaiel AG and Mridha AR analyzed the data and wrote the paper; Gamanagatti S, Jana M, Khan SA and Bakhshi S provided the patient's clinical data.

Institutional review board statement: This case report was exempt from the Institutional Ethics Board standards at All India Institute of Medical Sciences, New Delhi, India.

Informed consent statement: The patient involved in this case report gave her written informed consent authorizing use and disclosure of her protected health information.

Conflict-of-interest statement: None of the authors have any conflicts of interest.

Manuscript source: Unsolicited manuscript

Correspondence to: Asit Ranjan Mridha, MD, Assistant Professor, Department of Pathology, All India Institute of Medical Sciences, Ansari Nagar, New Delhi 110029, India. asit_aiims@yahoo.co.in
Telephone: +91-11-26593227
Fax: +91-11-26588641

Received: December 15, 2015
Peer-review started: December 18, 2015
First decision: February 29, 2016
Revised: May 14, 2016
Accepted: June 14, 2016
Article in press: June 16, 2016
Published online: August 28, 2016

Abstract

Erdheim-Chester disease (ECD) is an uncommon, non-familial, non-Langerhans cell histiocytosis, which involves skeletal system and soft tissue usually in middle aged and elderly patients. The characteristic radiologic features include bilateral, symmetric cortical osteosclerosis of the diaphyseal and metaphyseal parts of the long bones, or bilateral symmetrically abnormal intense ^{99m}Technetium labelling of the metaphyseal-diaphyseal region of the long bones, and computed tomography scan findings of "coated aorta" or "hairy kidneys". ECD in childhood with osteolytic lesion is extremely rare. We describe an unusual case with an expansile lytic bone lesion at presentation in a case of acute lymphoblastic leukemia.

Key words: Erdheim-Chester disease; Osteolytic lesion; Bone; Acute lymphoblastic leukemia

Core tip: Erdheim-Chester disease (ECD) is characterised by bilateral, symmetric cortical osteosclerosis of the diaphyseal and metaphyseal parts of the long bones. Occurrence of osteolytic lesions and presentation in childhood are extremely rare. We describe an unusual

case of ECD with an expansile lytic bone lesion in a case of acute lymphoblastic leukemia.

Vallonthaiel AG, Mridha AR, Gamanagatti S, Jana M, Sharma MC, Khan SA, Bakhshi S. Unusual presentation of Erdheim-Chester disease in a child with acute lymphoblastic leukemia. *World J Radiol* 2016; 8(8): 757-763 Available from: URL: http://www.wjgnet.com/1949-8470/full/v8/i8/757.htm DOI: http://dx.doi.org/10.4329/wjr.v8.i8.757

INTRODUCTION

Erdheim-Chester disease (ECD) results from excessive proliferation of CD68-positive and CD1a-negative foamy histiocytes and "lipid-laden" macrophages in different organs and tissues. It was first described in 1930 as "lipid granulomatosis" by Erdheim and Chester[1]. More than 550 cases have been described[2] and most are in middle aged and elderly patients. Bone is most commonly affected. The pathognomonic radiologic features are bilateral, symmetric cortical osteosclerosis of the diaphyseal and metaphyseal regions of the long bones, symmetric bilateral abnormally intense ^{99m}Technetium (Tc) labelling of the distal ends of the long bones, and, "coated aorta" and "hairy kidneys" which are seen on computed tomography (CT) scan due to soft-tissue sheathing of aorta and infiltration of the perirenal fat by the histiocytic infiltrate respectively[3,4]. Occurrence in childhood and presence of osteolytic lesions are uncommon[5,6]. Only a single case with multiple osteolytic lesions in a child with acute lymphoblastic lymphoma (ALL) has been reported[5]. But an expansile osteolytic lesion as the presenting clinical feature is unique to our case and has not been reported in the literature.

CASE REPORT

A 6-year-old female was diagnosed with B-cell ALL and treated as per International Network for Cancer Treatment and Research programs protocol. Complete clinical and haematological remission was achieved after induction therapy. Two years later, during maintenance therapy, she complained of pain in the right arm. Physical examination revealed a tender swelling in the right upper arm; while other systems were unremarkable. An X-ray of right arm revealed a multiseptated, expansile, lytic lesion with narrow zone of transition in the metaphysis of upper end of the right humerus with cortical discontinuity on medial aspect (arrow). No specific matrix mineralization or periosteal reaction was noted (Figure 1). Magnetic resonance imaging (MRI) of the right shoulder showed a solid expansile intramedullary mass replacing the normal marrow fat. It was hypointense on T1-weighted images, and hyperintense on T2-weighted images. There was a cortical break in medial upper humeral diaphysis with extension into soft tissue. A skip lesion in the humeral shaft with similar signal characteristics was also noted (white arrows) (Figure 2). A biopsy from the lesion showed fragmented bony trabeculae with widening of intertrabecular spaces by an infiltrate comprised of foamy histiocytic cells, lipid laden histiocytes, a few multinucleated giant cells, lymphocytes and fibroblastic cells (Figure 3A). No emperipolesis, mitosis or necrosis was seen. Histiocytic cells and giant cells were immunopositive with CD68 (1:50) (Novocastra, United Kingdom) (Figure 3B) and negative for CD1a (1:100) (Thermo Scientific, United States), Langerin (1:200) (Novocastra, United Kingdom), S100 (1:800) (Dako, United States), and CD23 (1:100) (Spring Bioscience, United States). Microscopic features were those of ECD. Subsequent skeletal survey revealed symmetric bilateral osteosclerosis of the metaphysis and diaphysis of both the long bones of the forearms and legs (arrows) (Figure 4) as well as patchy osteosclerosis involving pelvic bones and proximal femoral shafts (arrows) (Figure 5). Whole body MRI was performed in a 1.5 T MRI scanner (Acheiva 1.5 T, Philips, The Netherlands) and coronal whole body soft tissue inversion recovery sequence was acquired, followed by detailed evaluation of the foci of abnormality, using axial and coronal T2-weighted and T2-weighted turbo spin echo fat-suppressed sequences. Coronal whole body diffusion weighted imaging with background suppression imaging were performed using *b*-value of 0 and 400. The whole body MRI showed presence of bilateral ethmoid and maxillary sinusitis along with replacement of normal marrow by focal lesions involving maxilla (Figure 6), mandible, right humerus (involving epi-meta and proximal diaphysis), left scapula, head of left humerus, dorsal vertebra, sacrum, bilateral femoral and tibial diaphyses (Figure 7). Positron emission tomography-computed tomography (PET-CT) acquisition was done 45 to 60 min after injection of 10 mCi ^{18}fludeoxyglucose (^{18}FDG) by intravenous route from level of orbits to mid-thigh. PET-CT revealed increased tracer uptake in bilateral maxilla, head of the right humerus, and bilateral pubic and iliac bones (Figure 8) along with ground glass appearance in bilateral lungs. MR and PET-CT scans of the brain were normal. Besides mild pain and swelling in the right shoulder, the patient is otherwise doing well. She has been given conservative treatment with anti-inflammatory drug and kept under close follow up.

DISCUSSION

ECD is a primary histiocytic disorder with unknown aetiology and usually occurs during fifth to seventh decades of life with a slight male predominance[7]. It can involve multiple organ systems or any tissue of the body; however, bone is most frequently (96%) affected with a predilection for the femur, tibia and fibula[8]. Involvement of the humerus and axial skeleton is uncommon[9]. Soft tissue lesions are generally seen in the heart with endocardial, myocardial and pericardial involvement, coronaries, large vessels, lung parenchyma, pleura, retroperitoneum with or without ureteral obstruction and hydronephrosis, adrenal glands, retro-orbital region,

Table 1 Summary of Erdheim-Chester disease

Age	**Middle aged and elderly patients predominantly affected**
Site	Any tissue or organ can be affected and clinical manifestations depend upon the organ of involvement. Bone is most frequently affected (> 90%), however, at least one soft tissue component is seen in more than 50% of patients
Pathophysiology	Shows polyclonal proliferation of histiocytes associated with abnormal Th1 immune response. The recent studies however have suggested a clonal origin by demonstrating BRAFV600E mutations in more than 50% cases
Diagnostic criteria (Radiologic)	Bilateral, symmetric cortical osteosclerosis of the diaphyseal and metaphyseal regions of the long bones Symmetric bilateral abnormally intense Tc labelling of the distal ends of the long bones
(Histopathologic)	Characteristic "coated aorta" or "hairy kidneys" on CT scan; Xanthogranulomatosis or polymorphic granuloma with foamy/lipid laden histiocytes with immunoreactivity to CD68, but negative for CD1a and Langerin
Treatment	IFN-α and pegylated IFN-α are preferred for the treatment Anakinra (recombinant IL1R antagonist) and infliximab (anti-TNF-α antibody) may be used for second-line treatment Vemurafenib (an inhibitor of BRAF) especially for the patients with severe and refractory BRAFV600E histiocytoses
Follow-up (with PET-CT)	Useful for assessing extent of involvement both skeletal and extraskeletal components, activity and progression of disease, and monitoring of therapy

PET-CT: Positron emission tomography-computed tomography; Tc: ^{99m}Technetium; CT: Computed tomography; FDG: Fludeoxyglucose; IL: Interleukin; BRAFV600E: V-raf murine sarcoma viral oncogene homolog B1V600E; IFN: Interferon; TNF: Tumor necrosis factor; BRAF: V-raf murine sarcoma viral oncogene homolog B1.

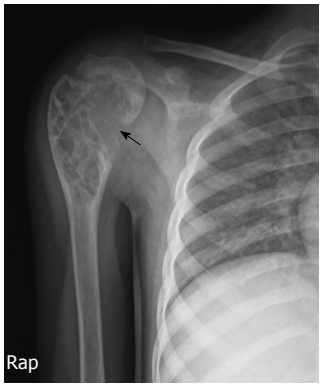

Figure 1 Anteroposterior radiograph of right shoulder showing multi-septated expansile lytic lesion with narrow zone of transition involving metaphysis of upper end of right humerus with cortical discontinuity on medial aspect (arrow). No specific matrix mineralization or periosteal reaction noted.

maxillary sinus, central nervous system including intra- and extra-axial compartments, skin, *etc.*[2]. At least one soft tissue involvement is present in more than 50% of patients[8,10]. The clinical presentation depends upon the organ of involvement and the common manifestations are bone pain (in 50% of cases)[3] diabetes insipidus, proptosis, renal, cardiovascular, central nervous system and retroperitoneal involvement[7,10]. The classic triad of ECD includes bone pain, diabetes insipidus and painless bilateral exophthalmos. The commonest cutaneous manifestation is xanthelasma. Some authors have categorized ECD as central nervous system, cardiac, vascular, endocrine, retroperitoneal, pulmonary dominant and multisystem type depending on the organ/tissue involvement[2]. ECD is rare in children and only seven cases have been reported[3]. Though clinical features are like that of adult patients; no cardiovascular involvement has been reported in children[5,6]. Localized pain and swelling in the right shoulder were the clinical presentation in our case.

Bone is most frequently (96% of cases) affected in ECD and the typical radiographic features include bilateral symmetric osteosclerosis of the metadiaphyseal region of long bones. Lytic lesions are infrequent and occur in < 10% of cases[5,7]. An expansive lytic lesion involving the epi-, meta- and proximal diaphysis of humerus, which was the presenting clinical feature in our case, has not been described earlier. Even though the exact pathogenesis needs to be elucidated, the lytic lesions may be due to localised increase in osteoclastic activity or reduced host bone response to the lesion. However, subsequent skeletal survey revealed typical features of ECD in the bilateral long bones of upper and lower extremities as well as osteosclerotic lesions in the pelvic bones and the femur. Epiphyseal and subperiosteal lesions are rare[9] and better visualized by MRI than plain radiograph or CT[3,8]. The classical CT scan findings of ECD are "coated aorta" and "hairy kidneys" which are seen in 23% and 68% cases respectively[3]. In the present case besides right humerus lesions, MRI also revealed focal lesions in the maxilla, mandible, left scapula, head of the left humerus, dorsal vertebrae, sacrum, bilateral femoral and tibial diaphysis, and right maxilla.

^{99m}Tc bone scintigraphy demonstrates bilateral, symmetric, abnormal labelling in the metaphyseal-diaphyseal parts of long bones especially in the lower limbs[8]. FDG PET-CT scan can assess extent of involvement including extraskeletal components, activity and progression of disease, and help monitoring of therapy[11] (Table 1). In addition to above bone and soft tissue lesions, the PET-CT scan in our case also showed mild bilateral lung parenchymal involvement which was also described by Wittenberg *et al*[12]. Lung lesions mainly affect the interlobular septae and are not associated with a significant prognostic factor for ECD[3].

Radiologic differential diagnoses of ECD are renal osteodystrophy, Pagets disease, myelofibrosis, osteoblastic metastases, chronic osteomyelitis, metabolic bone disorders[8,13] and in children with lytic lesion differentials include Langerhans cell histiocytosis (LCH), infection and metastatic neuroblastoma[5]. Imaging findings are

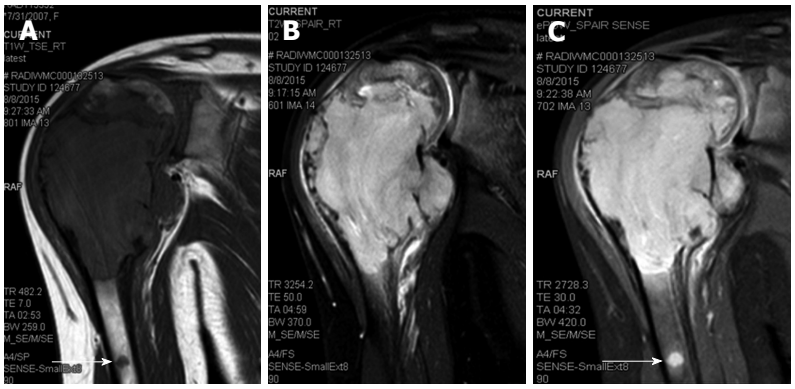

Figure 2 Oblique coronal turbo spin-echo T1-weighted (A), turbo spin-echo T2-weighted fat-suppressed (B) and proton-density-weighted fat-suppressed (C) magnetic resonance imaging images of the right shoulder showing a solid expansile intramedullary mass replacing the normal marrow fat; hypointense on T1-weighted images, hyperintense on T2-weighted images. A cortical break in medial upper humeral diaphysis with extension into soft tissue noted. Note another skip lesion in the humeral shaft with similar signal characteristics (white arrow).

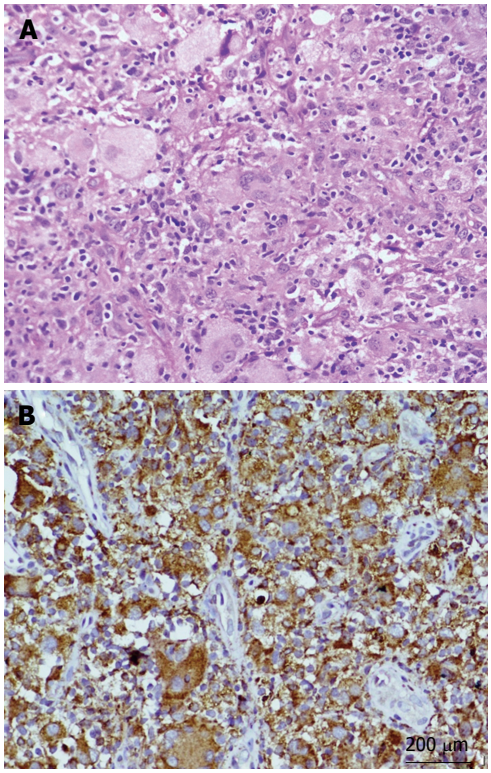

Figure 3 A biopsy from the lesion. A: Hematoxylin and eosin stained section showing an infiltrate comprised of foamy and lipid laden histiocytes, multinucleated giant cells, lymphocytes and fibroblastic cells (200 ×); B: Immunohistochemistry with CD68 showing positivity in histiocytic cells and giant cells (200 ×).

typical and pathognomonic for ECD in most of the cases. However, histopathologic examination is required to confirm the diagnosis and exclude the other possibilities and coexisting diseases such as LCH and Rosai-Dorfman disease (RDD).

Microscopic features of ECD include foamy histiocytic infiltrate with lipid laden macrophages/histiocytes, fibroblastic proliferation, lymphocytic infiltrate, granuloma formation with or without Touton giant cells and fibrosis[8]. LCH and RDD can rarely coexist either alone

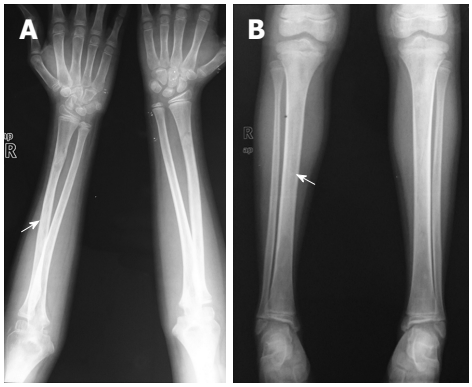

Figure 4 Anteroposterior radiographs of both forearms (A) and both legs (B) showing symmetric bilateral osteosclerosis of the metaphysis and diaphysis of the long bones (arrows).

or in combination with ECD. Histiocytes of ECD are immunoreactive to CD68, CD163 and Factor XIIIa; while, negative for CD1a and langerin, which are positive in LCH. In our case, histiocytes were negative for S100, CD1a and langerin. Absence of emperipolesis in our case also ruled out the possibility of RDD (Table 2). The association of ALL and ECD, similar to our case, has been reported only in a single child; but she had osteolytic lesions in multiple long bones and skull bones without any osteosclerosis[5].

ECD was considered as non-clonal condition associated with abnormal Th1 immune response producing several proinflammatory cytokines like interferon-α, interleukin (IL)-1/IL1-RA, IL-6, IL-12 and monocyte chemotactic protein-1[2,8,14]. The recent studies, however, have demonstrated v-raf murine sarcoma viral oncogene homolog B1V600E (BRAFV600E) mutations in more than 50% cases, suggesting the clonal origin[2,3]. The origin of ECD is thought to be from CD34(+) myeloid stem cells, which also give rise to various haematolymphoid malignancies[8]. The association between ECD with other histiocytic disorders like Langerhans cell histiocytosis, Rosai-Dorfman disease and rare cases of haematologic malignancies like Hodgkin lymphoma[15] and ALL could

Table 2 Differential diagnoses of Erdheim-Chester disease

Radiologic differential diagnoses	
With osteosclerotic lesions	Renal osteodystrophy, Pagets disease, myelofibrosis, osteoblastic metastases, chronic osteomyelitis, metabolic bone disorders
With osteolytic lesions in children	Langerhans cell histiocytosis, infection, metastatic neuroblastoma
Histologic	
Langerhans cell histiocytosis	Positive for S100, CD1a, and Langerin
Rosai-Dorfman disease	Histiocytes show emperipolesis; positive for S100 and CD68; negative for CD1a, and Langerin
Juvenile xanthogranuloma	Lack characteristic radiologic features of ECD; positive for factor XIIIa, CD68, CD163, fascin, and CD14, negative for CD1a, S100, and Langerin
Solitary/multicentric reticulohistiocytoma	Lack characteristic radiologic features of ECD; positive for factor XIIIa, CD68, CD163, fascin, and CD14; negative for CD1a, S100, and Langerin

ECD: Erdheim-Chester disease.

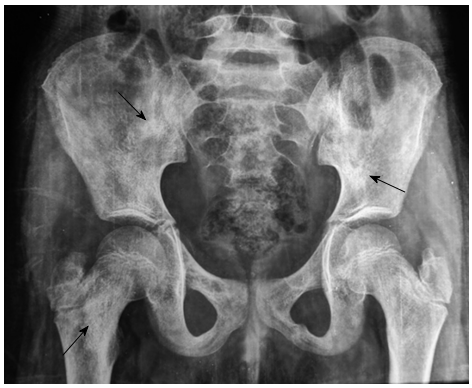

Figure 5 Anteroposterior radiograph of pelvis showing patchy osteosclerosis involving pelvic bones and proximal shafts of the femur (arrows).

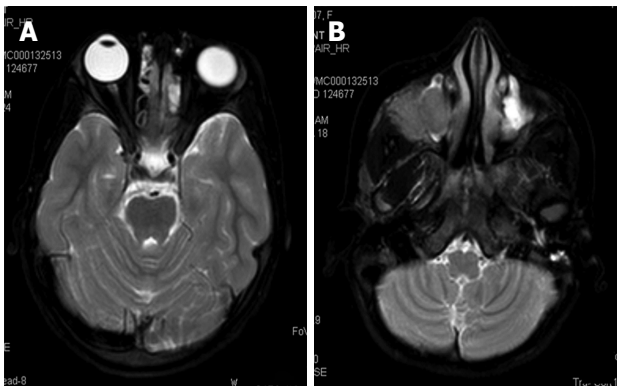

Figure 6 The whole body magnetic resonance imaging showing presence of bilateral ethmoid and maxillary sinusitis along with replacement of normal marrow by focal lesions involving maxilla. A: Axial TSE T2-weighted fat suppressed image of normal orbits; B: T2WFS axial image of the face showing isointense soft tissue filling the right maxillary sinus with extension into the infratemporal fossa. TSE: Turbo spin-echo; T2WFS: T2-weighted fat-suppressed.

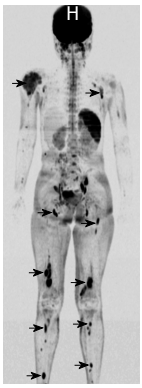

Figure 7 Whole body diffusion weighted imaging with background suppression imaging showing multiple skeletal lesions in right humerus, left scapula, bilateral femur and tibia (arrows).

be due to the origin from common precursor cells.

Current recommendations for evaluation of ECD are imaging studies including skeletal survey, CT scan of chest, abdomen, and pelvis, fluorine-18-fluorodeoxy-glucose- positron emission tomography (FDG-PET) of the entire body including brain and distal extremities, MRI of the brain and the heart with gadolinium, histo-pathological examination and v-raf murine sarcoma viral oncogene homolog B1 (BRAF) mutation analysis[2]. Immunohistochemistry using the BRAFV600E mutant specific antibody (anti-BRAF V600E) has high sensitivity and specificity[16]. However, it was negative in our case.

Corticosteroids, cytotoxic chemotherapies, radiotherapy and surgery were the treatment modalities prior to the discovery of interferon (IFN)-α[2]. Currently, IFN-α and pegylated IFN-α are preferred for the treatment and are associated with improved survival[17]. Treatment should be continued indefinitely if tolerated. An attempt at treatment cessation may be done for individual cases with minimal disease burden[2]. Anakinra (recombinant IL1R antagonist) and infliximab [anti-tumor necrosis factor (TNF)-α antibody] reduce the inflammatory mediators and may be used for second-line treatment. A pilot study using vemurafenib, an inhibitor of BRAF harbouring the V600E mutation, has shown dramatic clinical improvement in a few patients[18]. Treatment with LCH-protocol therapies in children with ECD has proved to be unsuccessful. FDG-PET scan is recommended for monitoring and assessing treatment response, every 3 to 6 mo for all patients following the initiation of treatment, and the frequency can be reduced once the disease has stabilized[2,19]. No specific therapy has been given to our patient and she has been kept under close follow-up.

Prognosis of patients with ECD has been reported to be dismal[14] and is generally worse with cardiovascular

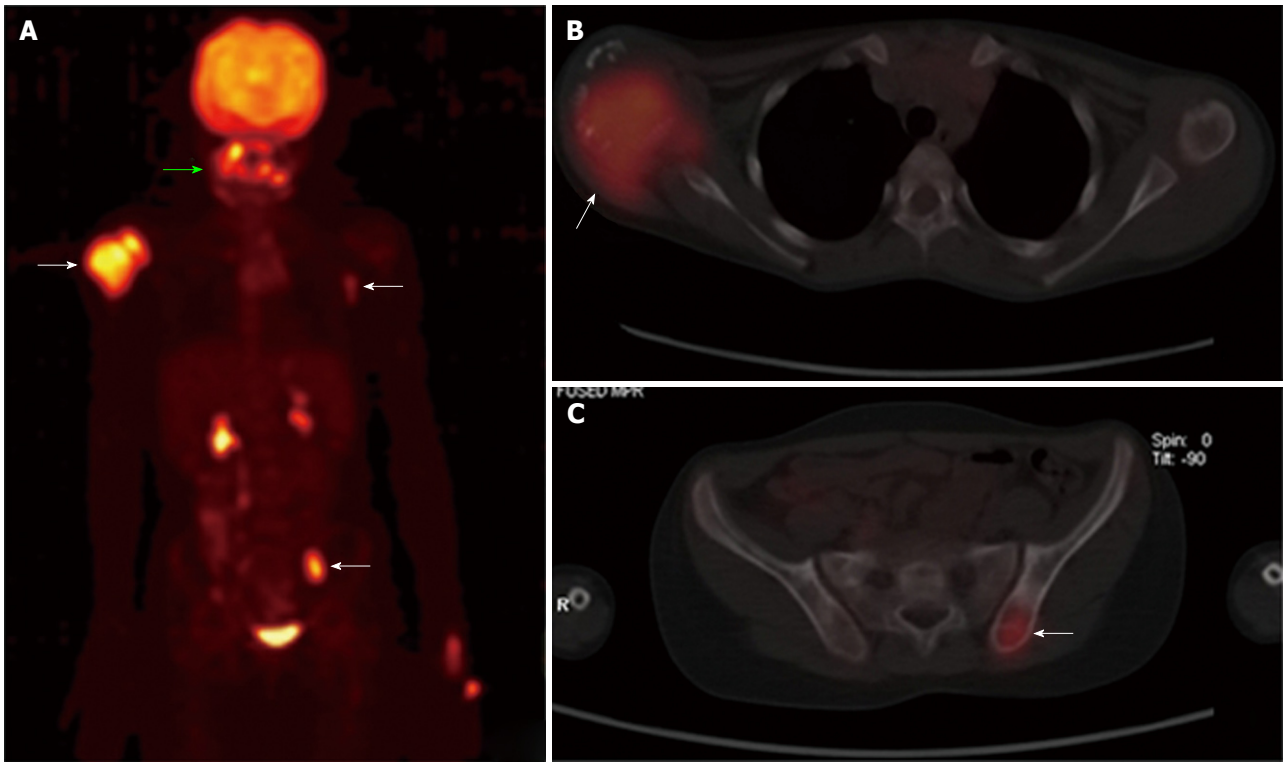

Figure 8 Positron emission tomography-computed tomography whole body maximum intensity projection image (A), axial fused images of chest (B) and pelvis (C) reveal areas of increased fluorodeoxyglucose uptake in right humeral head (arrow), the paranasal sinuses (green arrow), left thoracic wall (arrow) and left iliac bone (arrow). Note the physiological uptake and excretion in the kidneys and urinary bladder.

and central nervous system involvement. Overall mean survival is 32 mo and majority of patients die within 3 years from renal, cardiovascular, pulmonary or central neurological complications[7]. Arnaud *et al*[17] have reported 1-year and 5-year survival rates to be 96% and 68% respectively. ECD is a rare disease and may occur in association with other neoplastic and non-neoplastic diseases with atypical clinical presentation. High degree of suspicion and proper evaluation are required for the diagnosis of the disease, proper management and prediction of prognosis.

COMMENTS

Case characteristics

A 6-year-old female who had achieved remission after treatment for B-cell acute lymphoblastic lymphoma (ALL), presented with pain in the right upper arm.

Clinical diagnosis

Physical examination revealed a tender swelling in the right upper arm, suspicious of primary bone neoplasm.

Differential diagnosis

Langerhans cell histiocytosis.

Laboratory diagnosis

All labs were within normal limits including bone marrow aspirate for blasts.

Imaging diagnosis

An X-ray of right arm revealed a multiseptated, expansile, lytic lesion with narrow zone of transition in the metaphysis of upper end of the right humerus with cortical discontinuity without specific matrix mineralization or periosteal reaction while magnetic resonance images of the right shoulder showed a solid expansile intramedullary mass replacing the normal marrow fat, suggestive of Langerhan cell histiocytosis (LCH).

Pathological diagnosis

Polymorphic population with foamy and lipid laden histiocytes, which are immunopositive with CD68, but negative for CD1a and Langerin, compatible with Erdheim-Chester disease (ECD).

Treatment

Patient is kept on symptomatic treatment and a close follow-up.

Related reports

ECD presenting in childhood, especially after ALL and with osteolytic lesions is extremely rare. Only one case with multiple pure osteolytic lesions after ALL has been reported in the literature.

Term explanation

ECD is a non-LCH characterised by bilateral symmetrical osteosclerosis of diaphyseal and metaphyseal region of long bones.

Experiences and lessons

ECD may be mistaken for LCH which is the most common differential diagnosis of osteolytic lesions in childhood. High degree of suspicion and proper evaluation are required for an accurate diagnosis.

Peer-review

It is an excellent, well-written and documented work.

REFERENCES

1 **Chester W**. Uber lipoidgranulomatose. *Virchows Arch A Pathol*

Anat Histol 1930; **279**: 561-602 [DOI: 10.1007/BF01942684]
2 **Diamond EL**, Dagna L, Hyman DM, Cavalli G, Janku F, Estrada-Veras J, Ferrarini M, Abdel-Wahab O, Heaney ML, Scheel PJ, Feeley NK, Ferrero E, McClain KL, Vaglio A, Colby T, Arnaud L, Haroche J. Consensus guidelines for the diagnosis and clinical management of Erdheim-Chester disease. *Blood* 2014; **124**: 483-492 [PMID: 24850756 DOI: 10.1182/blood-2014-03-561381]
3 **Haroche J**, Arnaud L, Amoura Z. Erdheim-Chester disease. *Curr Opin Rheumatol* 2012; **24**: 53-59 [PMID: 22089098 DOI: 10.1097/BOR.0b013e32834d861d]
4 **Serratrice J**, Granel B, De Roux C, Pellissier JF, Swiader L, Bartoli JM, Disdier P, Weiller PJ. "Coated aorta": a new sign of Erdheim-Chester disease. *J Rheumatol* 2000; **27**: 1550-1553 [PMID: 10852289]
5 **Krishna VV**, James TE, Chang KT, Yen SS. Erdheim-Chester disease with rare radiological features in a 14-year old girl with pre-B Acute Lymphocytic Leukemia and Diabetes Mellitus. *J Radiol Case Rep* 2014; **8**: 7-15 [PMID: 25426240 DOI: 10.3941/jrcr.v8i8.1899]
6 **Song SY**, Lee SW, Ryu KH, Sung SH. Erdheim-Chester disease with multisystem involvement in a 4-year-old. *Pediatr Radiol* 2012; **42**: 632-635 [PMID: 21879308 DOI: 10.1007/s00247-011-2235-8]
7 **Veyssier-Belot C**, Cacoub P, Caparros-Lefebvre D, Wechsler J, Brun B, Remy M, Wallaert B, Petit H, Grimaldi A, Wechsler B, Godeau P. Erdheim-Chester disease. Clinical and radiologic characteristics of 59 cases. *Medicine* (Baltimore) 1996; **75**: 157-169 [PMID: 8965684]
8 **Mazor RD**, Manevich-Mazor M, Shoenfeld Y. Erdheim-Chester Disease: a comprehensive review of the literature. *Orphanet J Rare Dis* 2013; **8**: 137 [PMID: 24011030 DOI: 10.1186/1750-1172-8-137]
9 **Dion E**, Graef C, Miquel A, Haroche J, Wechsler B, Amoura Z, Zeitoun D, Grenier PA, Piette JC, Laredo JD. Bone involvement in Erdheim-Chester disease: imaging findings including periostitis and partial epiphyseal involvement. *Radiology* 2006; **238**: 632-639 [PMID: 16371583 DOI: 10.1148/radiol.2382041525]
10 **Antunes C**, Graça B, Donato P. Thoracic, abdominal and musculoskeletal involvement in Erdheim-Chester disease: CT, MR and PET imaging findings. *Insights Imaging* 2014; **5**: 473-482 [PMID: 25017251 DOI: 10.1007/s13244-014-0331-7]
11 **Arnaud L**, Malek Z, Archambaud F, Kas A, Toledano D, Drier A, Zeitoun D, Cluzel P, Grenier PA, Chiras J, Piette JC, Amoura Z, Haroche J. 18F-fluorodeoxyglucose-positron emission tomography scanning is more useful in followup than in the initial assessment of patients with Erdheim-Chester disease. *Arthritis Rheum* 2009; **60**: 3128-3138 [PMID: 19790052 DOI: 10.1002/art.24848]
12 **Wittenberg KH**, Swensen SJ, Myers JL. Pulmonary involvement with Erdheim-Chester disease: radiographic and CT findings. *AJR Am J Roentgenol* 2000; **174**: 1327-1331 [PMID: 10789787 DOI: 10.2214/ajr.174.5.1741327]
13 **Ihde LL**, Forrester DM, Gottsegen CJ, Masih S, Patel DB, Vachon LA, White EA, Matcuk GR. Sclerosing bone dysplasias: review and differentiation from other causes of osteosclerosis. *Radiographics* 2011; **31**: 1865-1882 [PMID: 22084176 DOI: 10.1148/rg.317115093]
14 **Al-Quran S**, Reith J, Bradley J, Rimsza L. Erdheim-Chester disease: case report, PCR-based analysis of clonality, and review of literature. *Mod Pathol* 2002; **15**: 666-672 [PMID: 12065781 DOI: 10.1038/modpathol.3880583]
15 **Bulycheva EN**, Baykov VV, Zaraĭskiĭ MI, Salogub GN. Rare form of erdheim-chester disease presenting with isolated central skeletal lesions treated with a combination of alfa-interferon and zoledronic Acid. *Case Rep Hematol* 2015; **2015**: 876752 [PMID: 25949835 DOI: 10.1155/2015/876752]
16 **Long GV**, Wilmott JS, Capper D, Preusser M, Zhang YE, Thompson JF, Kefford RF, von Deimling A, Scolyer RA. Immunohistochemistry is highly sensitive and specific for the detection of V600E BRAF mutation in melanoma. *Am J Surg Pathol* 2013; **37**: 61-65 [PMID: 23026937 DOI: 10.1097/PAS.0b013e31826485c0]
17 **Arnaud L**, Pierre I, Beigelman-Aubry C, Capron F, Brun AL, Rigolet A, Girerd X, Weber N, Piette JC, Grenier PA, Amoura Z, Haroche J. Pulmonary involvement in Erdheim-Chester disease: a single-center study of thirty-four patients and a review of the literature. *Arthritis Rheum* 2010; **62**: 3504-3512 [PMID: 20662053 DOI: 10.1002/art.27672]
18 **Haroche J**, Cohen-Aubart F, Emile JF, Arnaud L, Maksud P, Charlotte F, Cluzel P, Drier A, Hervier B, Benameur N, Besnard S, Donadieu J, Amoura Z. Dramatic efficacy of vemurafenib in both multisystemic and refractory Erdheim-Chester disease and Langerhans cell histiocytosis harboring the BRAF V600E mutation. *Blood* 2013; **121**: 1495-1500 [PMID: 23258922 DOI: 10.1182/blood-2012-07-446286]
19 **García-Gómez FJ**, Acevedo-Báñez I, Martínez-Castillo R, Tirado-Hospital JL, Cuenca-Cuenca JI, Pachón-Garrudo VM, Álvarez-Pérez RM, García-Jiménez R, Rivas-Infante E, García-Morillo JS, Borrego-Dorado I. The role of 18FDG, 18FDOPA PET/CT and 99mTc bone scintigraphy imaging in Erdheim-Chester disease. *Eur J Radiol* 2015; **84**: 1586-1592 [PMID: 25975897 DOI: 10.1016/j.ejrad.2015.04.022]

P- Reviewer: Garcia-Gomez FJ, Matsushita K, Monti L
S- Editor: Kong JX **L- Editor**: A **E- Editor**: Zhang FF

Published by **Baishideng Publishing Group Inc**
8226 Regency Drive, Pleasanton, CA 94588, USA
Telephone: +1-925-223-8242
Fax: +1-925-223-8243
E-mail: bpgoffice@wjgnet.com
Help Desk: http://www.wjgnet.com/esps/helpdesk.aspx
http://www.wjgnet.com